Advances in non-equilibrium CO₂ plasma kinetics : a theoretical and experimental review

Advances in non-equilibrium CO_2 plasma kinetics: a theoretical and experimental review

Lucia Daniela Pietanza[1], Olivier Guaitella[2], Vincenzo Aquilanti[3,4], Iole Armenise[1], Annemie Bogaerts[5], Mario Capitelli[1], Gianpiero Colonna[1], Vasco Guerra[6], Richard Engeln[7], Elena Kustova[8], Andrea Lombardi[3], Federico Palazzetti[3], and Tiago Silva[6]

[1] Consiglio Nazionale delle Ricerce, Istituto per la Scienza e Tecnologia dei Plasmi, Sede di Bari, via Amendola 122/D, 70126 Bari, Italy
[2] LPP, CNRS, École Polytechnique, Sorbonne Université, Université Paris-Saclay, IP-Paris, 91128 Palaiseau, France
[3] Dipartimento di Chimica, Biologia e Biotecnologie, Università di Perugia,Via Elce di Sotto 8, 06123 Perugia, Italy
[4] Istituto di Struttura della Materia, Consiglio Nazionale delle Ricerche, 00133 Rome, Italy
[5] Research group PLASMANT, University of Antwerp, Department of Chemistry, Universiteitsplein 1, BE-2610 Antwerp, Belgium
[6] Instituto de Plasmas e Fusão Nuclear, Instituto Superior Técnico,Universidade de Lisboa, Av. Rovisco Pais 1, Lisbon, 1049-001, Portugal
[7] PMP, Department of Applied Physics, Eindhoven University of Technology, 5600 MB Eindhoven, The Netherlands
[8] Saint Petersburg State University, 7/9 Universitetskaya nab., St. Petersburg, 199034, Russia

Abstract. Numerous applications have required the study of CO_2 plasmas since the 1960s, from CO_2 lasers to spacecraft heat shields. However, in recent years, intense research activities on the subject have restarted because of environmental problems associated with CO_2 emissions. The present review provides a synthesis of the current state of knowledge on the physical chemistry of cold CO_2 plasmas. In particular, the different modeling approaches implemented to address specific aspects of CO_2 plasmas are presented. Throughout the paper, the importance of conducting joint experimental, theoretical and modeling studies to elucidate the complex couplings at play in CO_2 plasmas is emphasized. Therefore the experimental data that are likely to bring relevant constraints to the different modeling approaches are first reviewed. Second, the calculation of some key elementary processes obtained with semi-empirical, classical and quantum methods is presented. In order to describe the electron kinetics, the latest coherent sets of cross section satisfying the constraints of "electron swarm" analyses are introduced, and the need for self-consistent calculations for determining accurate Electron Energy Distribution Function (EEDF) is evidenced. The main findings of the latest zero-dimensional (0D) global models about the complex chemistry of CO_2 and its dissociation products in different plasma discharges are then given, and full State-to-State (STS) models of only the vibrational-dissociation kinetics developed for studies of spacecraft shields are described. Finally, two important points for all applications using CO_2 containing plasma are discussed: the role of surfaces in contact with the plasma, and the need for 2D/3D models to capture the main features of complex reactor geometries including effects induced by fluid dynamics on the plasma properties. In addition to bringing together the latest advances in the description of CO_2 non equilibrium plasmas, the results presented here also highlight the fundamental data that are still missing and the possible routes that still need to be investigated.

PACS. XX.XX.XX No PACS code given

1 Introduction

The present review deals with the chemical-physics of cold CO_2 plasmas with the aim to collect a part of the efforts dedicated to this topic carried out by several European re-search groups (Belgium, France, Italy, Netherlands, Portugal and Russia) in the last years. Advanced simulation modeling and accurate experimental investigations have been recently developed to better understand the activation (dissociation) of CO_2 in non-equilibrium plasmas, with the aim to efficiently convert CO_2 in specific value-added chemicals. For this purpose, several types of non equilibrium plasma discharges have been investigated to

Correspondence to:
luciadaniela.pietanza@cnr.it,
olivier.guaitella@lpp.polytechnique.fr

efficiently convert CO_2 into molecules with higher added value over a large range of pressures and frequencies: from tens of mTorr to few Torr with direct-current (DC) glow or radio frequency (RF) discharges [1–4], from few Torr to tens of Torr with RF and microwave discharges (MW) [5–8], at atmospheric pressure with gliding arc [9–11], dielectric barrier discharges (DBD) [12–14] or micro-hollow cathode discharges [15] and even above atmospheric pressure with nanosecond discharges [16,17].

The interest on CO_2 plasma, however, has a long history starting from the 1960s with a wide variety of applications, ranging from CO_2 lasers [18], to astrophysical observations [19,20], surface treatment processes on carbon-containing substrates [21–26] and polymer deposition [27–29], or the design of spacecraft shields for planetary atmosphere entry [30,30–36]. Recently, also the possibility of *in situ* oxygen production from the CO_2 present locally in the atmosphere is being developed for futuristic human mission to Mars [2,37–39].

The recent revival of interest in CO_2 conversion by plasma has also its origins in works from the 1970s. The idea to use non-equilibrium plasmas for the CO_2 dissociation started indeed with the works of Fridman [40] and Capezzuto et al. [41], at the beginning of plasma-chemistry activity. In these first studies, it was already clear that non-equilibrium plasma discharges have a great potential in dissociating CO_2 due to the presence of energetic electrons, which activate the CO_2 gas by electron impact excitation (vibrational and electronic), leading to ionization and dissociation, without the need to heat the entire gas. In particular, they suggested the idea to increase CO_2 dissociation by selectively pumping energy into the lowest vibrational levels of the molecule through electron-molecule collisions, followed by vibrational-vibrational (VV) energy exchange processes, which populate the upper vibrational levels, promoting dissociation from these levels. In this way, the energy efficiency of the process is increased since the necessary input power is only that one needed to excite the first vibrational levels, instead of the much higher one requested for thermal or electron impact dissociation. For this reason, big efforts in the scientific community were dedicated in the understanding of the role of vibrational excitation in CO_2 dissociation in non equilibrium plasmas, both by modeling and experimental investigations. Different plasma configurations and operating conditions have been investigated to understand the dominant reaction mechanisms inducing dissociation. As an example, in DBD plasmas, which operate at high electric fields, CO_2 dissociation is mostly driven by direct electron impact processes, thus explaining the low energy efficiencies found in both experimental and modeling studies. On the other hand, MW plasmas seem to provide the best conditions to promote vibrational non-equilibrium that activates the vibrational ladder climbing mechanism. Their features, however, depend on pressure and gas temperature. By increasing the pressure up to atmospheric pressure, three-body recombination processes of the kind $CO + O + M \rightarrow CO_2 + M$ become very important and start limiting the effective CO_2 conversion.

Also, an increase of gas temperature is not beneficial for energy efficiency, since vibrational-translational (VT) energy relaxation processes start dominating reducing the CO_2 vibrational excitation. Moreover, with the increase of gas temperature, the plasma evolves to conditions in which the thermal dissociation is dominating instead of the plasma assisted one. This is not only true for MW plasmas, but also for gliding arc (GA) plasmas, operating at atmospheric pressure.

From an experimental point of view, the majority of the works dedicated to conversion efficiency of CO_2 by plasma uses complex reactor configurations for which only the conversion rate α, defined as $n_{CO}/(n_{CO}+n_{CO_2})$, and the conversion energy efficiency η are measured. Several review papers [42–45] already compare the different plasma sources from [1–14,16,17] and others in terms of α and η. However, these two parameters are insufficient to gain a deep understanding of CO_2 plasma kinetics and a similar dissociation rate α can be calculated with very different kinetic schemes because of the complexity of the energy transfers taking place between excited states of CO_2 and its by-products. Therefore, in this review, particular attention is paid to *in situ* experimental measurements of excited species densities and physical parameters (electric field, temperatures), as well as measurements dedicated to the study of individual collisional processes, which may provide essential information for developing and refining models.

From the modelling point of view, a challenging task is to provide an accurate description not only of the plasma chemistry of the CO_2 mixture, but also of the physical parameters characterizing the plasma discharges for the different plasma reactor geometries. To this purpose, a joint investigation between modeling and experimental works is beneficial for a mutual validating procedure of the results obtained. At the moment, the CO_2 research community has provided a very sophisticated description of the plasma chemistry in CO_2 plasma discharges by implementing 0D kinetic models, also called global models. These models have provided a deep understanding of the reaction mechanisms dominating the CO_2 mixture in different conditions, i.e. MW, DBD, pulsed discharge, nozzle expansion, and, despite the limitation of the 0D approach, have shown results in good agreement with experimental investigations. Special attention was also dedicated to the development of accurate vibrational kinetic models for CO_2 in a State-to-State (STS) approach, for the calculation of the corresponding vibrational distribution functions (VDF), which in non-equilibrium plasmas can deviate from the equilibrium Boltzmann distribution. The CO_2 asymmetric mode levels are generally taken into account, but a big effort is being made by different groups to extend the model also to symmetric and bending mode levels, as already done in full STS models describing the non-equilibrium vibrational kinetics in the hypersonic boundary layer of re-entering bodies in Mars atmosphere [46,47].

Non-equilibrium plasmas are characterized also by non-Maxwell electron energy distribution functions (EEDF). The EEDF can be calculated by solving the corresponding

electron Boltzmann equation in a self-consistent way with the STS plasma kinetic equations, describing the heavy particle kinetics. The electron kinetics is strongly coupled to the vibrational and electronic excited state kinetics of atoms and molecules. Actually, during the discharge, plasma electrons pump vibrational and electronic excited states by means of electron impact excitation collisions, while, in turn, especially in the post-discharge, vibrational and electronic excited states give energy back to the electrons through superelastic collisions, affecting the EEDF shape.

The difficulty of the global models with the STS approach is the need of an enormous number of electron impact cross sections and heavy-particle collision rate coefficients involving all the considered excited states of the involved species, i.e. CO$_2$ and its dissociation products. Semi-empirical, classical and quantum methods are being used for calculating them, but, despite the efforts made in the last years, data are still missing. As an example, the electron impact dissociation cross section and the dissociation rate coefficients by bimolecular heavy particle collisions, which are of fundamental importance for the description of CO$_2$ dissociation in plasmas, are still on debate. Similar considerations apply also to VV and VT rate coefficients characterizing the CO$_2$ vibrational kinetics, which in general are calculated by using scaling laws derived from first-order perturbation theories such as the Schwartz-Slawsky-Herzfeld one (SSH) [48]. Actually, more refined rate coefficient calculations can be provided by using the Forced Harmonic Oscillator (FHO) theory [49–53] or by using an appropriate Potential Energy Surface (PES) and a quasi-classical trajectory (QCT) dynamic method. The latter approach has been already used for the derivation of some VV and VT transition rates but could be extended also to other transitions [54–56], while the FHO theory was used to calculate an extensive matrix of VV and VT transitions for CO$_2$ very recently [52].

Another key challenge is to create an appropriate and complete electron impact cross section database for CO$_2$ plasma mixture species, which should be also compatible with the one involving heavy particle collisions, i.e by considering the same vibrational and electronic excited states. In this direction, a significant effort has been made for the calculation of detailed state-to-state electron impact cross sections and the derivation of complete and consistent cross sections sets by using swarm analysis, with the creation of open-access databases of great relevance for the low-temperature plasma community, such as, respectively, the Phys4Entry [57] and the IST-Lisbon [58] database reported in the LXCat database [59]. Despite considerable progress in the calculation of cross-sections and rate coefficients of elementary processes, as well as in the development of consistent sets of cross-sections for EEDF calculations, there are still too many unknown or poorly documented processes that make it difficult to predict CO$_2$ plasma properties. It therefore appeared necessary to initiate a step-by-step model validation by comparing the results of calculations with measurements made in simplified plasma configurations. By selecting particu-

lar operating regimes of low-pressure glow discharges, it is possible to test one by one the accuracy of the EEDF calculations, the VV and VT coefficients, and the main chemical reactions under conditions of weak CO$_2$ excitation [60–64].

Another challenge in getting the description of the models to converge with the quantities measured in experiments is the need to take into account the effect of surfaces in contact with the plasma. Interaction with complex surfaces is at the centre of most CO$_2$ plasma applications (polymer deposition, spacecraft heat shielding, etc.). In the case of CO$_2$ plasma recycling, the combination of plasma with catalytic materials is one of the best options to improve the energy conversion efficiency. Many processes occur on surfaces, such as vibrational de-excitation or recombination of oxygen atoms. New chemical reactions, or reactions with a different rates can also happen on surfaces with species produced in the plasma. All these effects are strongly dependent on the physico-chemical nature of the surface and their study is therefore complicated by the material specificity of the experimental results obtained. In addition, the breakdown of the plasma itself can be affected by the properties of the surface, which is particularly true in the case of streamers initiating on catalysts. All these complex phenomena are the subject of many studies, often performed in distinct communities, and are briefly discussed in this review.

The CO$_2$ research community has also tried to better describe the geometry of the plasma reactors, to investigate which reactor designs can increase the CO$_2$ conversion. From a modeling point of view, this has been done by implementing higher dimensional fluid dynamics models (2D and 3D) with the compromise of reducing the kinetic scheme modules and/or of applying them to simpler gas mixtures, i.e. helium or argon, or air. All previous aspects are analyzed in detail throughout the paper, by reviewing part of the results obtained by the present community in the description of CO$_2$ non equilibrium plasmas.

The paper is organized as follows. Section 2 focuses on the experimental data available for CO$_2$ plasma, providing information about elementary processes, in situ measurements of short-lived species and plasma parameter measurements such as electric field, electron density and gas and vibrational temperatures. Section 3 reports the state of the art about theoretical calculations of elementary collisions processes, involving heavy-particle (section 3.1) and electron impact collisions (section 3.2). In particular, for heavy-particle collisions, QCT calculation methods are discussed and a focus on the quantum mechanical derivation of the activation energy of the Boudouard process important for the CO$_2$/CO kinetics is provided. A detailed overview of the most recent available database for electron impact cross section sets is also performed. Section 4 gives a general discussion of the state of the art of 0D kinetic modeling for CO$_2$ plasma mixtures in different conditions, with an important focus on the insights that can be obtained by these models for the characterization of the CO$_2$ plasma discharges. Section 5 focuses on the electron kinetics and on the importance of a self-consistent approach de-

scription of the electron and the heavy-particle kinetics. Section 6 provides a discussion about the results obtained by a successful modeling and experimental joint investigation, applied to the description of a pulsed DC CO_2 glow discharge, which have provided a step-by-step validation procedure of different aspects characterizing the complex CO_2 plasma kinetics. Section 7 shows the results obtained by a full STS vibrational kinetic model applied to the description of the hypersonic entry of vehicles in Mars atmosphere. Section 8 addresses three key aspects of plasma-surface interaction for CO_2 plasmas by discussing vibrational de-excitation at the walls, oxygen atom recombination probabilities, and plasma-catalyst interactions. Section 9 provides a brief overview on 2D/3D fluid models, implemented for a spatial distribution description of plasma reactors, not possible with lower dimensional kinetics models. Finally, the conclusions with important perspectives is presented.

2 Experimental data available for CO_2 plasma understanding

The various applications of CO_2 plasmas that have been investigated (CO_2 lasers, surface treatment processes, design of spacecraft shields, CO_2 recycling etc...) have resulted in experimental studies conducted under a wide range of pressure conditions, gas mixtures and discharge types. All these works can provide valuable information for the understanding of CO_2 plasma kinetics. However, the information they provide is not always straight-forward to be used as input data or even as comparison for models. As already mentioned, many articles dedicated to CO_2 conversion are reporting CO_2 conversion rate (α) and energy efficiency (η). While these parameters are certainly important for application purposes, they are not sufficient to understand the elementary processes taking place in the plasma. Our aim, in this section, is not to repeat the comparison of plasma sources in terms of α and η, already well documented in review articles [42–45]. Here we focus on experimental works providing either basic data about elementary processes taking place in CO_2 plasmas, or *in situ* measurements of short-lived species and physical parameters such as field, temperatures, etc. These data are necessary to disentangle the effects of the coupled energy transfer mechanisms between the numerous excited electronic and vibrational states of CO_2 and its dissociation by-products illustrated in the energy diagram on Fig. 1. The coupling between the electron kinetics and the numerous radicals, vibrational and electronic excited levels produced in CO_2 plasmas shown on this energy diagram makes the complexity of CO_2 containing plasmas. Unfortunately, a lot of energy exchange processes between these different species are still poorly known. In fact, sometimes even the excitation cross section of these states by direct electron impact suffers from large uncertainties.

Experimental data concerning elementary processes involving excited states, or discharge parameters such as the electric field, electronic density or gas temperature, are
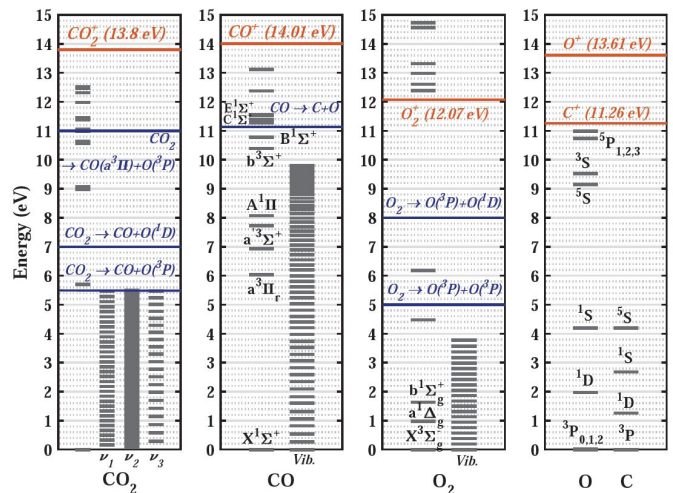

Fig. 1. Energy diagram of electronic and vibrational excited states of the most relevant species in CO_2 plasma

therefore challenging but essential to gain understanding of CO_2 plasmas. The remainder of this section lists some of the works that have reported either *in situ* experimental data in CO_2 plasma, or experimental data on some key elementary processes concerning: i. electronic impact collision processes (Sec. 2.1), ii. vibrational kinetics (Sec. 2.2), iii. the role of excited electronic states and radicals (Sec. 2.3), and iv. the influence of surfaces (Sec. 2.4).

2.1 Electron impact collision processes

A correct description of electronic impact processes is essential for any plasma model. This requires, on the one hand, sets of cross sections for electron impact processes and, on the other hand, direct information on electron properties in various plasma discharges (namely electron density n_e and temperature T_e).

Concerning the first point, section 3.2 gives a state of the art of cross sections databases available for electron impact processes on CO_2 but also for its dissociation products CO, O_2 and O. Here we recall only the experimental difficulties associated with the measurement of these cross sections. As detailed in section 3.2, the problem of total energy losses of electrons must be well distinguished from that of the individual cross sections of each ionisation, electron excitation, ro-vibration or dissociation processes. One of the reasons for this is the accuracy with which it is possible to measure the overall electron scattering parameters in comparison to the accuracy usually obtained for individual processes cross sections.

Total scattering cross sections (TSCS, which include elastic scattering) are usually obtained by transmission methods: the intensity decay of an electron beam passing through a gas cell is measured, and the TSCS is deduced from Beer-Lambert formula. This is a direct absolute measurement for which achievable precision is typically better than 5%. The main inaccuracies often come from the precision of gas pressure measurement (this can make TSCS

prior to 1970 less reliable) and the angular resolution error resulting from the lack of discrimination between electrons scattered within the angular acceptance of the detector. In the case of molecules serious issues arise, especially at low energy for which inelastic scattering due to rotational and vibrational level can be challenging to distinguish from elastic scattering [65–68].

Another approach to deduce integral cross section as a function of energy consists in measuring macroscopic transport coefficients in the so called 'swarm experiments'(SE). In fact, SE comprise different types of experimental configurations, all having relatively simple principles but requiring quite complex analysis to obtain transport coefficients [67–70]. For instance drift velocity v_{dr} and longitudinal diffusion can be obtained from 'Time-of-flight'technique (TOF) monitoring the time an ensemble of swarm electrons (generated by photo-emission at the cathode or with a filament for instance) needs to go across a drift tube with a uniform field between two shutters. Transversal diffusion D_T is obtained in a similar manner by injecting the electron through a small orifice and with a segmented anode [70, 71]. In the technique called 'Pulsed Townsend discharge'(PT), the time variation of electron density is measured either electronically or by integrating the photon flux to deduce the ionization coefficient and v_{dr}. Like TOF and PT, other variation of SE such as 'voltage transient' [72] or 'spatial variation of current' [73] are all based on the analysis of electron avalanches induced in uniform electric field. The main source of experimental errors in SE comes from gas purity, accuracy of gas density or uniformity of the electric field. Recent works, such as [74] for PT technique, are still improving the measurement accuracy using the CO$_2$ case as benchmark. The main difficulty is the complexity of the analysis needed to relate measured transport coefficients to an integral cross section. This requires either a Monte-Carlo simulation describing the kinetics of the electron swarm, or a Boltzman solver to compute an EEDF with a self-consistent set of cross sections allowing to reproduce the transport parameters. The main issue is then the non-uniqueness of the effective cross-section sets capable of reproducing the transport coefficients, in particular for electronegative gases. Other data on elementary processes must therefore be considered to provide constraints on the relative importance of each process. Nevertheless the great merit of the data from these experiments is to provide an excellent benchmark for the overall consistency of a complete set of effective sections used to calculate EEDFs as described in section 3.2. Data from SE for CO$_2$ can be found in [75–79], for instance.

Various techniques have been used to obtain cross sections of individual inelastic collision processes. Electron impact ionization can be measured accurately (between 5 to 10%) with an electron beam ionising the gas contained between two plates imposing a perpendicular electric field. This gives the total ionization cross section [80], but the different ions formed can also be analysed by using time of flight mass spectrometry [81–83]. Cross beam experiments can provide information on specific excitation

processes such as the excitation of the first vibrational levels of CO$_2$ [84, 85]. Recent experimental developments (for instance with modulated electron beams) can overcome the limitations on detection of scattered electrons at angle close to the incident beam axis as shown for electron impact excitation of CO(a$^3\Pi$) [86]. Optically allowed transitions can also be determined from the measurement of the number of photons emitted as a function of the energy of incident electron beam. However, in addition to the difficulty to normalize the results to an absolute scale, cascade effects can lead to large errors. More details about experimental methods for individual cross section measurements can be found in [65, 66, 87]. Although CO$_2$, CO and O$_2$ are among the molecules that have been the most studied, large uncertainties remain about individual processes cross-sections that are often difficult to deconvolve when several excitation channels are open at the same energy. Therefore theoretical works remain crucial to complete the data for missing processes. A striking example of the still substantial lack of basic data is the one of CO$_2$ dissociation by electronic impact for which cross sections reported in literature can largely vary both in shape and magnitude as shown in [88]. It is shown in section 6.3 that recent measurements of dissociation rate coefficient in glow discharge [89] have allowed to constraint the correct cross section.

Beyond the knowledge of cross sections themselves, the modelling of electronic kinetics in various CO$_2$ plasma discharges would greatly benefit from direct experimental measurements of electric field (E$_{field}$), electron density (n$_e$) and temperature (T$_e$) but these data are scarce. Langmuir probes have been used at low pressure (typically 0.1 mbar) in RF-ICP discharges [90–92] providing n$_e$ and T$_e$ together with the dissociation fraction of CO$_2$. In glow discharges at few mbar n$_e$ can be deduced from the imposed current and the electron mobility after measuring the E$_{field}$ with two floating potential pins inserted in the positive column [62, 89, 93, 94]. It can also be measured with MW interferometry as shown in glow discharge for CO$_2$ laser studies [95] as well as low pressure (few mbar) CO$_2$ nanosecond discharge [96]. At higher pressure however the diagnostic methods available to characterize electron properties are limited. In [97] the broadening of H$_\beta$ line is used to measure n$_e$ in CO$_2$/H$_2$ MW discharge. In [98] n$_e$ and T$_e$ were obtained in CH$_4$ and N$_2$ MW discharge with Thomson scattering but the strong rotational Raman signal overwhelmed the Thomson signal for CO$_2$. In nanosecond discharge at atmospheric pressure, only electrical current of individual pulses can be monitored but the relation with n$_e$ is not straight-forward [99, 100]. It is worth noting also that almost no experimental data exist concerning ions in CO$_2$ plasmas. Recently positive ions have been measured with MS in He/CO$_2$ RF jet [101].

There is a clear need for more experimental data concerning electron properties, also in order to describe correctly the vibrational kinetics. Indeed, electron and vibrational kinetics are not only linked by the excitation of vibrations via electron impact (e-V) but also by the heating of the electrons by super-elastic collisions (as discussed in
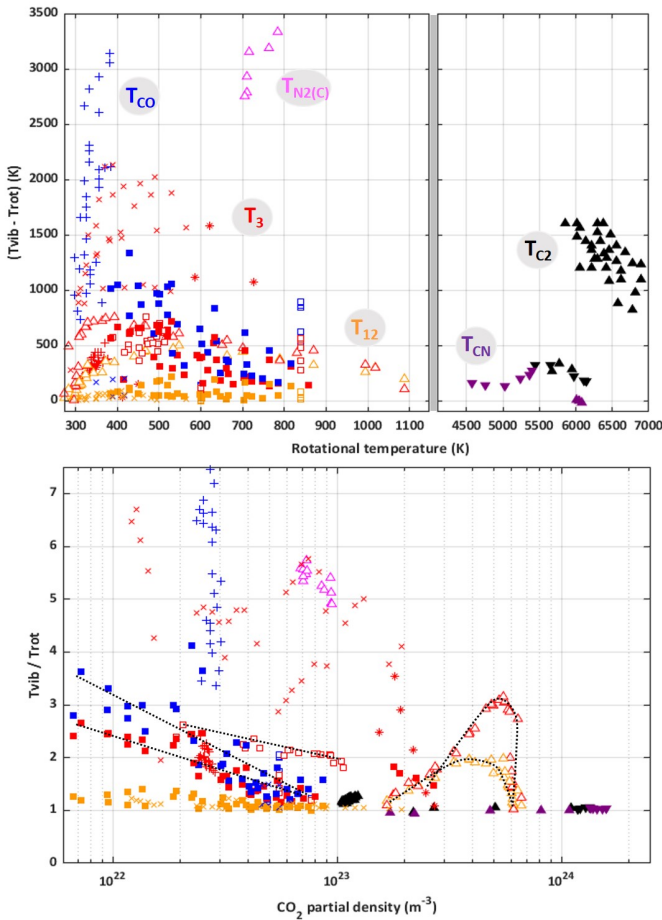
Fig. 2. (a) Difference between vibrational temperatures and rotational temperature (T_{vib}-T_{rot}) of various molecules measured in CO_2 containing plasmas as a function T_{rot}. **(b)** Same data plotted as degree of non equilibrium (T_{vib}/T_{rot}) as a function of the partial density of CO_2. Colors corresponds to the vibrational temperature considered with (red) for T_3 the temperature of the asymmetric mode of CO_2, (orange) for T_{12}, (blue) for T_{vib} of CO (T_{CO}), (magenta) for the electronic state N_2(C) ($T_{N_2(C)}$), (black) for C_2 (T_{C_2}) and (purple) for CN (T_{CN}). Symbols corresponds to different type of plasma discharges with ▲ for MW [43, 98, 103–105] and ▼ for MW torch [106], ■ for Glow discharges [60, 107, 108], + for RF [109], × for capillary discharge in laser gas mixture (CO_2/N_2/He) [110–112], and ∗ for non-self sustained discharges [113]. Open symbols □ and △ are for transient measurements in pulsed discharges.

section 5), or even by ionization induced in collisions of vibrationally excited molecules as shown for CO in pump probe experiments [102].

2.2 Vibrational kinetics in CO_2 containing plasmas

Measurements of vibrational temperatures (and/or individual vibrational level population densities) are essential data to describe CO_2 plasma. Unfortunately data available are scarce compared to the literature dedicated to conversion rates and energy efficiency. Fig. 2 shows a col-

lection of experimental data for vibrational (T_{vib}) and rotational (T_{rot}) temperatures measured in CO_2 containing plasmas for different purposes such as CO_2 recycling, CO_2 lasers, or planetary entry [43, 60, 98, 103–113]. On Fig. 2 (a) most of the data measured in different plasma discharges correspond to values of T_{rot} below 1000 K. Only the MW discharges at pressure equal or close to atmospheric pressure studied for CO_2 recycling [103, 104] or radiation for spacecraft shield design [106] are inducing very high T_{rot} from 4500 to 7000 K. The direct measurement of CO_2 vibrational temperature in the asymmetric mode (T_3) or the symmetric/bending mode (T_{12}) is often very challenging (note that only one temperature T_{12} is used to describe the temperature of the bending and the symetric stretching mode because of the Fermi resonance between these two modes which will be described in section 6). Many studies of CO_2 containing plasma are therefore only reporting T_{vib} from the emission of electronically excited states from other molecules in the gas mixture such as N_2(C), CN or C_2. Nevertheless T_3, T_{12} and the vibrational temperature of CO (T_{CO}) have been measured by infrared absorption spectroscopy using either FTIR or tuneable laser diodes in glow discharges [60, 107–113], and by Raman scattering in MW discharges [98, 105]. Rotational Raman scattering has also been used in glow discharges [64, 114] but only the degree of non equilibrium characterized by the even and odd vibrationally averaged nuclear degeneracies could be obtained in addition to T_{rot}. The difference T_{vib}-T_{rot} for T_{rot}<1100 K on Fig. 2 (a) shows that in all the conditions measured a rough general ordering of vibrational temperature could be done with $T_{N_2} > T_{CO} > T_3 > T_{12}$. T_{12} remains always very close to T_{rot} which is expected from the small energy difference between levels of symmetric and bending mode favouring the de-excitation into gas heating (see Fig. 1). The large energy difference between levels of CO_2 asymmetric stretch mode ν_3 is beneficial to reach non equilibrium conditions but part of the energy stored in ν_3 is lost through (V-V') transfer into ν_{12}, and the V-T transfers are still quite efficient. These two effects combined explain that T_3 is systematically lower than T_{CO} in all the conditions reported. The high efficiency of V-T transfers to de-excite ν_3 levels can be inferred from Fig. 2 (b), which represents the degree of non-equilibrium in a slightly different way than Fig. 2 (a), using the parameter T_{vib}/T_{rot} plotted as function of n_{CO_2}, the partial density of CO_2 in the gas mixtures studied (calculated as $n_{CO_2} = f_{CO_2} \cdot P/(k_B \cdot T)$ with f_{CO_2} the fraction of CO_2 in the gas mixture entering the plasma, P the pressure, k_B the Boltzmann constant and T the temperature taken equal to T_{rot}). The data shown with +, × and ∗ symbols corresponds to measurements performed in CO_2 largely diluted in noble gases (10% CO_2 in Ar and He with a RF jet in [109]), in typical CO_2 laser gas mixtures of CO_2/N_2/He [110–112] and for non-self sustained discharges [113], respectively. The limited collision with other molecules and favourable EEDF in these gas mixtures explain the much higher T_{vib} than any of the data obtained with larger proportions of CO_2. All the solid points are measured either in continuous glow discharge (■) or con-

tinuous MW (▲). These data show a thermalization of all molecules measured ($T_{vib} = T_{rot}$ for CO_2, CN, C_2) for densities higher than $\sim 10^{23} m^{-3}$. For lower densities T_{12} is still nearly thermalized, but T_{CO}/T_{rot} is always higher than T_3/T_{rot} with an almost linear decay respectively from 4 to 1 and from 3 to 1 between $n_{CO_2} = 6.10^{21} m^{-3}$ and $10^{23} m^{-3}$. This correspond to the quenching by V-T transfers increasing with the collision frequency. However the fact that data obtained with diluted CO_2 remains at higher non equilibrium reveals the key role of CO_2 dissociation products in these quenching processes. In particular O atoms are very efficient quenchers of the vibrations as already claimed in CO_2 lasers literature [111, 115] and evidenced more recently in [108]. As already seen on Fig. 2 (a), the gas temperature also increases the efficiency of vibrational quenching. Therefore it is possible to maintain non-equilibrium at relatively high CO_2 density when using pulsed discharges as shown with the open symbols on Fig. 2 (b) for glow discharges (□) [60, 107] and MW (△) [98, 105] (dotted lines are plotted to help seeing the trends). This is made possible by the fact that vibrational excitation via electronic impact is achieved faster than gas heating, and because CO_2 dissociation products accumulate less in pulsed discharge. As a result, at the beginning of plasma pulses, the gas temperature is still low enough for the V-Ts to not yet effectively lower the vibrational temperatures, allowing the T_3/T_{rot} ratio to reach values ~ 3.

A few other papers report densities of individual vibrational levels measured by IR absorption in H_2 with few percent of CO_2/CH_4 [116], or by CARS on N_2 in $CO_2/N_2/He$ [117]. Nevertheless there is certainly a lack of experimental data on the vibrational excitation of CO_2 especially since vibrationally excited molecules can play a key role in plasma chemistry. For instance it is often claimed that effective CO_2 recycling requires promoting the reaction 1 [40, 118]

$$CO_2(v) + O \rightarrow CO + O_2 \qquad (1)$$
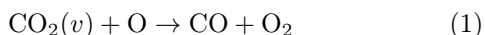
but this process has not yet been directly evidenced experimentally.

The Boudouard or disproportionation reaction 2 is an example of an important chemical reaction involving vibrationally excited molecules which has been studied in 'pump/probe 'experiment by exciting vibrational state of CO by laser and detecting resulting CO and CO_2 by FTIR [119].

$$CO(v) + CO(w) \rightarrow CO_2 + C \qquad (2)$$

where v and w are the quantum numbers describing two possible vibrational excited levels. Different estimations of the corresponding activation energy are available in literature. A focus on this aspect is reported in section 3.1.4, while the effect of this important reaction on the CO vibrational kinetics is analysed in section 5. The Boudouard reaction occurs only if the combined vibrational energy of reactants exceed the activation energy of the process, showing how the role of vibrations in chemical reactions can therefore be of prime importance, but unfortunately it remains insufficiently studied experimentally until now.

2.3 Role of radicals and electronic states

In addition to vibrational states, electronic excited states and radicals also play an important role in the kinetics of CO_2 plasmas. In particular, it is worth mentioning the key role of oxygen atoms (both in fundamental and excited state $O(^3P)$ and $O(^1D)$), as well as the metastable states of CO and O_2 molecules (especially $CO(a^3\Pi)$ and $O_2(^1\Delta_g)$).

As already mentioned in section 2.2, O atoms are very efficient quenchers of CO_2 (and CO) vibrational states [108]. So called 'Flow Tube Experiments'(FTE) are providing useful data about reactions occurring in collisions with short-lived species in general, and about quenching of vibrations by O atoms in particular. In FTE, a flow of CO_2 or CO excited in a specific state (by laser for $CO_2(\nu_3=1)$ [115, 120] or heat jump for $CO_2(\nu_2=1)$ [121–123] and CO(v=1) [124]) is injected into a flow of O atoms obtained either downstream of a MW discharge [115, 120], or by photolysis of O_3 [121, 123, 124]. The population density of the vibrational state detected by its fluorescence or with IR absorption is then measured as a function of the O atoms density in the flow. These data are very valuable but their precision rely on two absolute measurements (of the vibrational state density and of the O atoms density) both bringing their sources of inaccuracies. The quenching rate of CO_2 bending mode by $O(^3P)$ has also been deduced from LIDAR observation at different altitudes in the atmosphere [125] but results were not consistent with lab experiments showing deficiency in modelling of atmospheric $15\mu m$ radiation.

Beyond being 'quenchers'of vibrations, oxygen atoms are also highly reactive chemical species. They can contribute to the 'back reaction mechanisms'giving back CO_2 from CO in a three body reaction.

$$CO + O + M \rightarrow CO_2 \qquad (3)$$

The reaction 3 can produce a broadband chemiluminescence emission often studied in flame combustion [126–128] and recently in MW discharge [129]. However this reaction occurs mostly at high temperature, or at the walls with the surface acting as third body [130]. At low pressure and temperature, back reaction mechanisms are probably dominated by other reactions involving for instance $CO(a^3\Pi)$ state [131]. In any case, the avoidance of recombination of O atoms whether in O_2 or CO_2 is a key process to achieve an energy efficient conversion of CO_2, and the use of membrane to extract O atoms from the plasma could enhance the conversion efficiency [37]. At high pressure, O atoms are also forming O_3 as measured in CO_2 corona discharge [132] which is of importance for planetary atmosphere chemistry. Despite their key role in CO_2 plasma chemistry, very few values of O atoms densities have been measured in plasmas for which CO and CO_2 densities were simultaneously determined [21, 93]. In fact, most of the O atoms density measurements were focussing only on their surface reactivity for spacecraft shield design [32, 33, 133–135].

A variant of the FTE has also been used to study the quenching of $O(^1D)$ electronic state by CO_2 and CO

as done for the study of the Earth's upper atmosphere chemistry. A flow of $O(^1D)$ is produced by photolysis of O_3, N_2O or NO_2 and collides with a flow of CO_2 or CO. The resulting state of the molecules is measured by IR absorption with FTIR or tuneable laser diode [136–139]. The quenching of $O(^1D)$ by CO is a test case of efficient electronic energy transfer to vibrations (about 25% of the energy) happening via a long-lived complex intermediate [136]. In [137,138] the quenching with CO_2 is shown to lead mostly to kinetic energy and weak dissociation into CO and O. However more recent work [139] shows the possibility of vibrational excitation through CO_3 intermediate. It is particularly important to understand the exact reactivity of $O(^1D)$ as it is one of the states produced by the dissociation of CO_2 via electronic impact at $\sim$7eV. Another excited electronic state that can result from CO_2 dissociation is the $CO(a^3\Pi)$ state.

$CO(a^3\Pi)$ is a metastable state storing $\sim$6 eV (see fig. 1) with a radiative lifetime of $\sim$2.6 ms measured in molecular beam experiment [140,141]. The emission of the forbidden transition from $CO(a^3\Pi)$ to the ground state, called the 'Cameron band 'has been measured for instance in Mars airglow [142]. $CO(a^3\Pi)$ can be excited: i. by electron impact (cross section measured in molecular beam experiment together with other electronic states [143–146]), ii. by radiative cascade (decay from e.g. $CO(b^3\Sigma^+)$ called '3rd positive band '), iii. by dissociative excitation of CO_2 by electron impact ($>$11.5 eV), and iv. by dissociative recombination of the CO_2^+ ion as measured in the downstream of a MW plasma in FTE [147]. The large amount of energy carried by this metastable state can influence significantly both vibrational kinetics and chemistry [131, 148]. The transfer from electronic to vibrational energy in collisions between $(CO(a^3\Pi) + CO)$ is found to happen with 89% efficiency in [149] leading to fast redistribution of energy on high vibrational levels and radiation. $CO(a^3\Pi)$ can be simply quenched to the ground state in collisions with CO and O_2 as measured in [150–152] but it can also react with another CO to dissociate into $C+CO_2$ [119,150,153,154] or with O_2 to produce $CO_2 + O$ [150] (see also equation 12 in section 5 and the related discussion). Depending on pressure and temperature conditions, this last reaction can even be the main 'back reaction mechanisms 'as shown in [131]. Even though $CO(a^3\Pi)$ appears to be a key specie in CO_2 plasma dynamics, its direct measurement is very challenging and has been done only in very diluted gas mixture for CO_2 laser study [155].

Other electronic states of dissociation products of CO_2 could play an important role in CO_2 plasma such as $O_2(a^1\Delta_g)$ and $O_2(b^1\Sigma_g^+)$ but almost no data exist concerning their interaction with CO_2 except for their quenching [156,157].

carbon-containing substrates such as polymers [21], glassy carbon [22], carbon nano-structures [23,24], graphene [25, 26] or polymers [27–29] are exposed to a plasma in which CO_2 can either be a byproduct released in the plasma, or the feed gas used for the treatment. However the primary field in which the interaction of CO_2 plasmas with surfaces has been studied experimentally is probably the design of atmospheric re-entry shields. While many works in this field focuses on the radiation emitted at high temperature by CO_2 plasmas using LIF [158] or emission spectroscopy in the downstream intense plasma sources (ICP torch, arc shock tube, MW torch etc...) [159–164] (see the importance of these experiment in section 6), a few studies report on the 'catalycity 'of materials exposed to the plasma. In particular the recombination of oxygen atoms at walls is an important heating source of materials because of the large energy dissipated. O atom recombination probability (γ_O) in the downstream of various CO_2 plasma discharges have therefore been measured on metal (silver, molybdenum, etc.) and ceramic surfaces (quartz, SiC, Al_2O_3, etc.) to simulate Martian atmosphere entry [32,33,134,135]. In these experiments, O atoms density and γ_O were measured by actinometry [134], TALIF [135] or calorimetry and simulation of the heat flux [32,33]. Actinometry has also been used in the field of surface treatment to measure γ_O in a RF discharge used for coating with HMDSO [21]. Recently both actinometry and TALIF have been compared in a pure CO_2 glow discharge studied for CO_2 recycling [93]. It is worth mentioning that O atoms can contribute to 'back reaction mechanisms 'by recombining with CO into CO_2 at the walls [130,150].

Surfaces can also be responsible for vibrational de-excitation which is an additional source of heat for spacecraft shield, and a detrimental contribution for CO_2 lasers. Several works have therefore measured surface vibrational de-excitation with the aim of minimizing it. The measurement is usually performed with 'pump-probe'experiment in which CO_2 is excited by a laser in the first ν_3 level and the decay of spontaneous fluorescence at $4.3\mu m$ is measured over quartz [165], Pyrex, Brass, Mylar Teflon [166] or metal surfaces [167]. Similar experiments have also been done for CO vibrational surface deactivation [168,169]. All these experiments provide valuable information but they also highlight on the one hand the need for theoretical work on elementary processes as discussed in section 3, and on the other hand the need to return to relatively simple plasma configurations to validate kinetic schemes due to the intrinsic complexity of CO_2 plasmas (see section 7).

2.4 Influence of surfaces

The interaction of CO_2 plasmas with surfaces is central to many applications. For instance the coupling of CO_2 plasma with catalyst is one of the main paths studied to achieve efficient CO_2 recycling as detailed in section 8. Surface treatment processes are another example in which

The surface mechanisms undoubtedly add an additional level of complexity to the understanding of CO_2 plasmas. Before they can be properly taken into account, a solid basis on the elementary collision processes is required.

3 State of the art about theoretical calculations of elementary collision processes

In the present section, we focus on elementary collision processes occurring in CO_2 plasmas, involving heavy-particle collisions (see section 3.1) and electron impact ones (see section 3.2). As already pointed out in section 2.2, the CO_2 kinetics is strongly dependent on VV and VT and vibrational activated CO_2 dissociation. Unfortunately, no complete sets of vibrational state specific rate coefficients for heavy particle collisions in CO_2 plasma is available. This kind of information can be explicitly calculated by using molecular dynamics calculations based on quasi-classical methods, using appropriate potential energy surfaces as shown in section 3.1.2. A focus on the Boudouard process important for the CO kinetics is also provided due to recent quantum mechanical calculations of its activation energy. A lot of uncertainty is still present on electron impact cross sections and the need of a complete electron impact cross section database is crucial for the development of kinetic models on CO_2 plasmas. The available and recent electron impact database sets are overviewed in section 3.2.

3.1 Heavy particle collisions

The collisions between heavy particles in plasmas promotes the energy exchange between translations, rotations and vibrations. These processes, conveniently treated as quantum transitions between molecular states, are best described by the evaluation of the related State-to-State (STS) detailed dynamical quantities, from which, by statistical combination and averaging, *ab initio* kinetic observables can be generated. Approximate, reduced-dimension methods, such as the Schwartz-Slawsky-Herzfeld (SSH) theory [48], are routinely used to devise large sets of kinetics data. These are based on scaling of known parameters over quantum numbers and temperatures and have the merit of a straight application. A more accurate approach can be based on the Forced Harmonic Oscillator (FHO) theory [49, 50, 170], which is the extension to higher-order terms of the same kinetic theory the SSH first-order approximation is based on. However, these theories are not expected to be generally accurate, since many degrees of freedom are not included in the original formulation. The simulation of molecular collision dynamics is instead the way to obtain comprehensive data bases of cross sections and rate coefficients for the Vibration-Vibration (VV) and Vibration-Translation (VT) energy exchange processes in gas phase.

In the case of collisions involving CO_2 molecules,overall highly demanding calculations are required, due to the complexity of the interactions and to the relatively high number of internal degrees of freedom. Consequently, full dimensional quantum treatments are a rather impractical approach for systematic calculations. A fairly feasible approach resorts to so called "Quasiclassical" Trajectory (QCT) calculations, performed by specific dynamics programs (see e.g. [171]). The method is illustrated in next section.

3.1.1 The quasiclassical trajectory method

In QCT calculations the collision dynamics is described in a classical mechanics framework, where the cross section of an energy exchange event upon collision involving initial and final states denoted as i and f, depends on the impact parameter b as follows:

$$\sigma_{ij}(E) = \int_0^{b_{max}} 2\pi b P_{ij}(E, b) db \qquad (4)$$

where b_{max} is a truncation limit for the integration, corresponding to the maximum distance range in which the intermolecular potential is effective, P_{ij} is the STS probability associated to the energy exchange event and E is the relative energy of collision. By running a large number of collision trajectories, with the appropriate initial conditions, the probability P_{ij} is obtained as simply the ratio between the number of trajectories corresponding to i–j transitions and the total number of trajectories, N_{ij}/N_t. The cross section σ_{ij} can be estimated as

$$\sigma_{ij}(E) = P_{ij}(E)\pi b_{max}^2 \qquad (5)$$

according to the classical interpretation of this observable as a target area. The selection of the initial conditions, from which the collision trajectories are started, is a key point in the QCT method. In the usual procedure, the collision energy E is given a fixed value for an entire batch of trajectories, while the values of the initial rotational angular momenta of the colliding molecules are selected by sampling the Boltzmann distribution corresponding to a given rotational temperature T_{rot} and the corresponding vectors are randomly oriented; the initial vibrational states of the molecules are explicitly selected according to specified vibrational quantum numbers. Initial coordinates and momenta for the relative motion are chosen assigning to the impact parameter b a value chosen in the range $[0, b_{max}]$. Finally, the molecules are randomly oriented, with the initial intermolecular distance set large enough to make the interaction between them negligible. The vibrational state of the linear CO_2 molecule requires four quantum numbers, however the one corresponding to the vibrational angular momentum can be disregarded, since bending states with significant rotational energy are unlikely (i. e. the rotational energy with respect the molecular axis is in general very low [54]).

The above scheme is suited for VV and VT exchange processes, since cross sections and probabilities obtained from the trajectories are specific for vibrational states, but thermally averaged over rotations (at the given rotational temperature). Thermal averaging over translations can be also achieved, for a given temperature T, assigning different E values to any trajectory, as generated from a sampling of the Boltzmann distributions of the relative velocities. In most cases the rotational temperature T_{rot} can be assumed to be equal to the translational temperature T,

due to the different typical time scales for relaxation of rotations and translations.

The output of QCT calculations is a set of classical final states (in the form of phase-space vectors) of the CO_2 molecules, that are to be matched with the given initial states. The final vibrational energy of each mode of vibration can be calculated by projecting the final phase-space vectors into the CO_2 normal mode basis vectors. This means assuming harmonic motion for the molecular vibrations and separable normal modes, a pretty reasonable approximation for the first lower vibrational states. To deliver the state-to-state vibrational transition probabilities, cross sections and rate coefficients, the classical normal mode energies have to be quantized. Therefore the final step, after running each given bunch of trajectories, is a data-binning procedure, yielding final vibrational quantum numbers. After this proper selection of the averaged initial conditions the thermal state-to-state rate coefficient for an $i - j$ transition (e.g. vibrational) can be expressed as follows:

$$k_{ij}(T) = \left(\frac{8kT}{\mu\pi}\right)^{\frac{1}{2}} \sigma_{ij}(T) \qquad (6)$$

where μ is the reduced mass of the system. To ensure statistical accuracy of the results, large batches of classical trajectories have to be run, for each given initial vibrational state, over the desired range of temperatures, with massive computational efforts. In this respect, we mention that the use of QCT techniques on parallel and distributed computing infrastructures can be easily implemented because of the perfect decoupling of individual trajectories (or of small batches of them). However, the quality of the results also depends on the accuracy of the Potential Energy Surface (PES) in modeling long- and short-range intermolecular forces (see below).

An alternative and in principle more accurate method, balancing accuracy and computational costs, combines a more accurate quantum mechanical treatment (for selected vibrational degrees of freedom) with classical mechanics ones (for the remainder), the so-called quantum-classical method [172], so far adopted for atom-diatom and diatom-diatom collision [173], but in principle amenable of extensions to three-atom molecules.

3.1.2 Potential energy surfaces

The outcomes of the molecular collision events depend on the intermolecular interactions, which affect the energy disposal among the different degrees of freedom (translation, rotations and vibrations). An accurate Potential Energy Surface (PES) is therefore necessary for realistic simulations of the energy transfer processes. The intermolecular potentials can be in principle characterized in detail by molecular beam scattering experiments [174] and, for some aspects, by spectroscopic studies of van der Waals complexes. However, information about the potential has to be inferred from the experimental results by complex inversion procedures; case by case, a parametric

model potential has to be adopted and the sets of parameters have to be varied to obtain best agreement with experiments from the integration of the dynamics equations. The reproduction of glory oscillations and the second virial coefficients is an optimal quality test for the interaction model, see e.g. [175]. Intermolecular forces are expected to be varying when excited vibrational and rotational states distort the molecular geometry, since the physical properties they are directly connected with, such as polarizability and charge distribution, are affected by molecular deformations. Accordingly, a suitable PES should explicitly account for the variation of the intermolecular interaction parameters with the internal coordinates of the molecules and the more the energy is high, the more this dependence is crucial.

An appropriate functional representation of the PES for a system of colliding molecules can be designed as the sum two terms accounting for energy contributions coming from intra- (that is bond lengths and angles) and inter-molecular (distance of the two molecules and angles defining their mutual orientation) degrees of freedom, as follows:
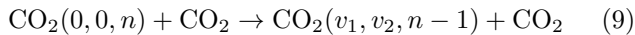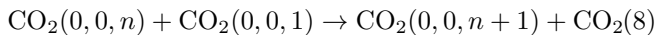
$$V(R, \Omega, \mathbf{q}) = V_{intra}(\mathbf{q}) + V_{inter}(R, \Omega) \qquad (7)$$

where V_{intra} represents the internal potential energy (intramolecular) of the isolated molecules, depending on the internal coordinates denoted as $\mathbf{q}$, V_{inter} is the intermolecular potential energy, R is the distance between the centers of mass and Ω collectively denotes the angles defining the mutual orientation of the molecules. The internal interaction energy is usually replaced by an *ab initio* ground state potential energy surface. The intermolecular interaction energy V_{inter} of Eq. 7 mainly includes two effective contributions, say V_{vdW}, representing the van der Waals interactions (size repulsion and dispersion attraction effects), and V_{elect} representing the purely electrostatic interactions. Both terms depend on the intermolecular distance R, while they are weakly dependent on Ω (anisotropy of the interaction). V_{elect} depends on the anisotropy of the charge distribution of the interacting molecules. In some collisions, the molecules approach each other closely, so that a model for V_{vdW} based on pairwise contributions between specific interaction centers located on atoms or atom groups is more suited. The so called Improved Lennard Jones (ILJ) potential [55], where the interactions between centers is modelled by using a general potential function for each contribution to the V_{vdW} term adopts this view. For the CO_2–CO_2 and CO_2–N_2 colliding systems, the dependence of the PES from stretching and bending degrees of freedom was derived in Refs. [55, 56] where the obtained PESs were also improved thanks to a comparison with ab initio data and the measured second virial coefficients.

3.1.3 QCT results for CO_2-CO_2 and CO_2-N_2 collisions

To illustrate the StS rate coefficient calculations for molecular collisions, we consider here the CO_2–CO_2 and the

CO_2–N_2 systems, for their relevance to plasma chemistry, atmospheres and astrochemistry and the prototypical complexity of carbon dioxide as a three-atomic molecule. For both systems the PESs have been obtained in Refs. [55,56], where the dependence of the intermolecular interaction on vibrational motion has been included and the effects on energy transfer have been assessed. The same PESs are here used to simulate the dynamics of the following processes involving CO_2 by the QCT method:

$$CO_2(0,0,n) + CO_2(0,0,1) \rightarrow CO_2(0,0,n+1) + CO_2 \quad (8)$$

$$CO_2(0,0,n) + CO_2 \rightarrow CO_2(v_1,v_2,n-1) + CO_2 \quad (9)$$

where n is the quantum number of the asymmetric stretching (~ 2390 cm^{-1}) and the two zeroes are referred to the symmetric stretching and bending quantum numbers, according to the standard notation. CO_2 represents the molecule in the lowest vibrational state. As stated above, just three quantum numbers for the vibrations of CO_2 are considered. The VV exchange of Eq. 8 is studied at T = 300 K and for $n = 0, \cdots, 9$.

The VT relaxation channel of the asymmetric stretching in Eq. 9 is simulated at T = 300 K, with the quantum numbers $v_1 = 0, 1$ and $v_2 = 1, 2, 3$ combined in such a way that the allowed states are (1,0,0), (1,1,0), (0,1,0), (0,2,0), (0,3,0). This representation for the VV and VT processes has been adopted to facilitate comparison with corresponding SSH derived rate coefficients by Kozak and Bogaerts [118]. In Fig. 3 we show the rate coefficients for the VV and VT processes of Eqs. 8 and 9, compared with equivalent results from [118] obtained by scaling based on SSH theory.

Furthermore, we simulated over a range of temperatures a second VT process, corresponding to the exchange (gain or loss) of a quantum of bending energy

$$CO_2(0,m,0) + CO_2 \rightarrow CO_2(0,m \pm 1,0) + CO_2 \quad (10)$$
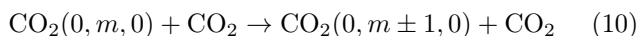
and make the comparison with the equivalent process from [176], where the corresponding thermal rates were obtained by SSH theory extended for polyatomic molecules (see Fig. 4 a). Finally, as an example involving N_2, we run QCT calculations for the following VT transfer process on a range of temperatures

$$CO_2(0,0,1) + N_2(0) \rightarrow CO_2(1,0,1) + N_2(0) \quad (11)$$

obtaining the thermal rate coefficients, in order to assess the effects of the molecular vibrations on the intermolecular interactions (see V_{inter} in Eq. 7). Results are shown in Fig. 4 b, where the same rate coefficients are also reported as coming out by neglecting the dependence of the intermolecular forces from vibrational motion. This corroborates the point emphasized in previous section about geometry deformations, affecting the intermolecular potential and consequently the collision observables.

3.1.4 Boudouard reactions

As will be discussed in the next pages, one of the major component of the dissociation of CO_2 is CO, becoming important in the whole CO_2 plasma kinetics.
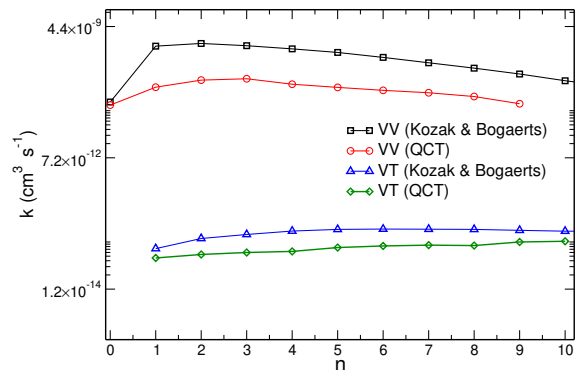

Fig. 3. VV and VT energy transfer upon CO_2+CO_2 collisions, STS rate coefficients for the processes in Eqs. 8 and 9 are reported as a function of the asymmetric stretching quantum number n. The QCT results are compared to those obtained by SSH scaling from [118]. In the VT processes (blue and green plots) the final excited symmetric stretching and bending states can be any one of (1,0,0), (1,1,0), (0,1,0), (0,2,0), (0,3,0).
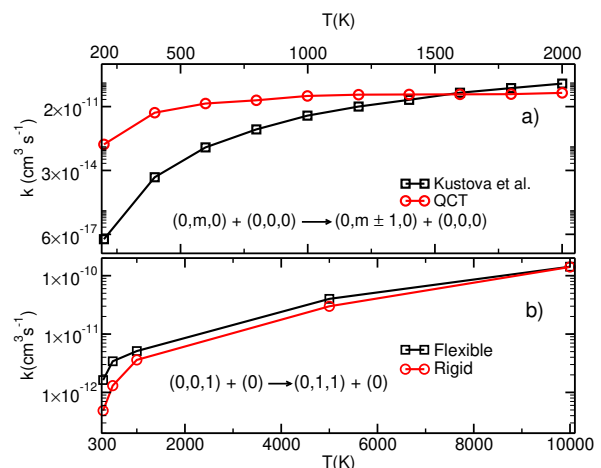

Fig. 4. (a) VT energy transfer in CO_2+CO_2 collisions, STS rate coefficients for the process in Eq. 10 as a function of temperature, comparison between QCT results and SSH rates from [176] and [118], respectively. (b) CO_2+N_2 collisions, rate coefficients for the process in Eq. 11, comparison between rigid (no effect of deformations) and flexible PES.

The first studies on the CO kinetics were developed to understand the corresponding CO laser in the infrared region. Wide use was made by solving a vibrational master equation containing V-V (vibrational-vibrational) and V-T (vibrational translational) energy exchange processes. Maxwell and non-Maxwell electron energy distribution functions were also taken into account to calculate the electron-vibrational energy exchange processes (the e-V) one and the dissociation process either by electron impact or by the so called Boudouard reaction [177]. This method was used by Gorse et al. [177,178] emphasizing the role of the

Boudouard reaction [179,180] against dissociation rates by electron impact. The Boudouard reaction involving only vibrationally excited states of the ground state of the two CO molecules is reported in Eq. (2).

The reaction can also involve an electronically excited molecule, $CO(a^3\Pi, v)$, in a triplet metastable state

$$CO(a^3\Pi, v) + CO(X^1\Sigma_g, w) \Leftrightarrow CO_2 + C \quad (12)$$
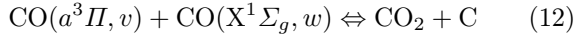
The Boudouard reaction for the ground state (see Eq. (2)) was firstly examined by Rusanov et al. [179, 180] by using a statistical theory of chemical reactions that assumes formation of a long-lived intermediate complex, where the energy moves freely among the modes. The corresponding equation contains the activation energy of the process. The forward rate constant k_f for process in Eq. (2) can be written as [181]
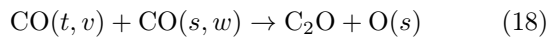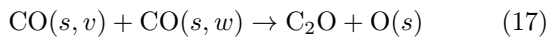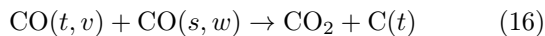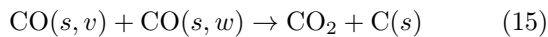
$$k_f = \sum_{v=0}^{v_{max}} \sum_{w=0}^{w=v_{max}} k_f^{v,w} \quad (13)$$

where $k_f^{v,w}$ is given by

$$k_f^{v,w} = v(T)\theta_{v,w} S f_v f_w \left[1 - \frac{E_a}{E_v + E_w}\right]^2 \left(\frac{\omega_{CO}}{\omega_{CO_2}}\right)^2 \quad (14)$$

where $v(T) = 3 \times 10^{-10}(T/300)^{1/2}$ is the frequency of gas kinetic collisions of CO molecules, E_a the activation energy of the process, E_v and E_w are the vibrational energy of the reactants, ω_{CO} and ω_{CO_2} are the vibrational frequencies of CO and CO_2 (in the latter case the one of the asymmetric mode), $\theta_{v,w}$ is a step function (i. e. $\theta_{v,w}=1$ when $E_v + E_w \geq E_a$, $\theta_{v,w} = 0$ when $E_v + E_w < E_a$) and S is a steric factor.

Different values of this activation energy have been proposed in these years, starting with a value of 6 eV estimated by Rusanov et al. [179, 180], followed by a value of 8 eV by Martin [181] and more recently Essenhigh et al. [119] measured an activation energy of 11.6 eV. These differences propagating in the reaction rates are shown in [182]. More recently Barreto et al. [154] determined the reaction rates by using the transition state theory and a quantum chemistry approach to get the forward and backward activation energies of the Boudouard processes, which can be written in compact form in the following way

$$CO(s,v) + CO(s,w) \rightarrow CO_2 + C(s) \quad (15)$$

$$CO(t,v) + CO(s,w) \rightarrow CO_2 + C(t) \quad (16)$$

$$CO(s,v) + CO(s,w) \rightarrow C_2O + O(s) \quad (17)$$

$$CO(t,v) + CO(s,w) \rightarrow C_2O + O(s) \quad (18)$$

The symbols s and t denote singlet and triplet states of CO and v, w represent the vibrational excited states of CO. The transition rate constants, for v=w=0, are determined using the equation

$$k^{TST}(T) = \left(\frac{k_B T}{h}\right) \left(\frac{Q^{\neq}}{Q_{CO}^A Q_{CO}^B}\right) \exp\left(-\frac{V_a^{G^{\neq}}}{RT}\right) \quad (19)$$

where Q_{CO}^A, Q_{CO}^B and $Q^{\neq}$ are the partition functions of the CO reactants and of the transition state, T is the temperature, and k_B and h are the Boltzmann and Planck constants. The term $V_a^{G^{\neq}}$ is the vibrationally adiabatic ground-state potential-energy curve, which is given by the sum of the classical potential energy of the saddle point, $V^{\neq}$, and the zero-point energy, ϵ_{ZPE}. The contribution from the translational mode along the reaction coordinate for the partition function of the transition state, corresponding to an imaginary frequency and accounted by the term $k_B T/h$, has not been considered. The rate constants k of the four reactions as a function of the reciprocal of temperature, 1/T, and fitted by the Arrhenius equation

$$k = A \exp\left(-\frac{E_a}{RT}\right) \quad (20)$$

are shown in Fig. 5. In Eq. 20, E_a represents the activation energy of the different processes and A is the pre-exponential term without considering the vibrational energy. Fig. 6 reports the energy of the different processes including the transition state calculated by using quantum theory [154]. These data were used in the calculation of rate coefficients of the four reactions without considering the role of vibrational energy (i.e. v=w=0). To simplify the notation, reactions can be schematically written as

$$CO + CO \rightarrow TS \rightarrow CO_2 + C \quad (21)$$

$$CO + CO \rightarrow TS' \rightarrow C_2O + O \quad (22)$$
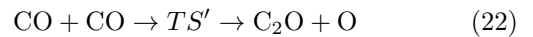
where TS and TS' represent the transition states. In the case of two vibrationally excited molecules participating in the reaction, the simplest approximation consists in considering the total vibrational energy $E_v + E_w$, so that the vibrational energies of both reactants are characterized by equal efficiencies in the reaction. The state-to-state rate constant becomes $k_f^{v,w}$ and the effect of vibrationally excited states on the total rate is given by Eq. 13 with Eq. 14 written in the form

$$k_f^{v,w} = f_v f_w A \exp\left(-\frac{E_a}{k_B T}\right) exp\left(\frac{\alpha(E_v + E_w)}{k_B T}\right) \quad (23)$$

where f_v and f_w are the populations (expressed in molar fractions) of the vibrational states of reactants, while A represents the pre-exponential term in the Arrhenius equation (see Table I). The parameter α was calculated according to the rule of Macheret and Rusanov: $\alpha \approx \frac{E_a}{(E_a + E_a^-)}$, where E_a^- is the apparent activation energy of the inverse reaction; the corresponding results have been reported in Table I. The role of the vibrational energy entering in the different rates is inserted by using the semi-empirical
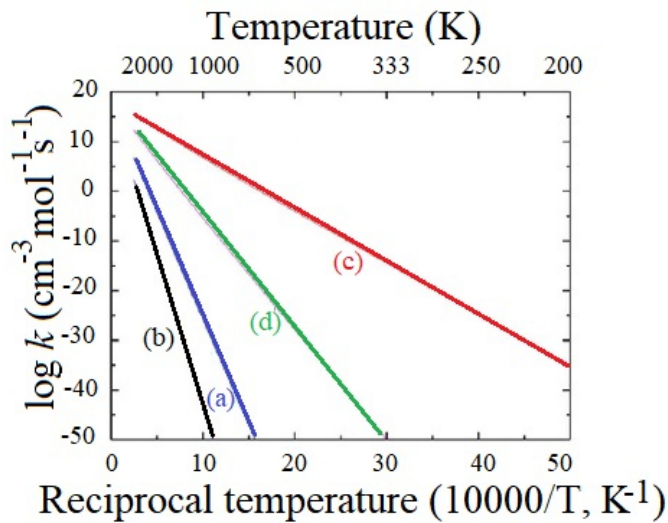
Fig. 5. Rate constants, log k, as a function of 10000/T (bottom axis) and T (top axis) of (a) $CO(s)+CO(s) \rightarrow CO_2+C$ (Eq. 15); (b) $CO(s)+CO(s) \rightarrow CO_2+C$ (Eq. 16); (c) $CO(s)+CO(s) \rightarrow C_2O + O$ (Eq. 17); (d) $CO(s)+CO(t) \rightarrow C_2O + O$ (Eq. 18)

Fig. 6. Energy (in kcal/mol) diagrams for the four reactions, with the corresponding structure and relative energy of the activated complexes, TS(s), TS(t), TS'(s), TS'(t)

method of Macheret et al. [183] able to define for each Arrhenius form a parameter α.

The most important point of the present table is the large difference in the activation energy of the four processes. In particular, the presence of the metastable state in the reactions is such that it strongly decreases the activation energy of process having large differences on the relevant rates. Considerations about reactions involving the triplet state should involve a sort of separation of the vibrational energies between ground and metastable states. This is a problem still far from being solved.

3.2 Electron impact collisions

Electron impact processes are of paramount importance in any plasma, as they are the driving mechanism for plasma-reactivity. Electrons are easily accelerated by electric fields and transfer their energy in collisions where they excite, dissociate and ionize the various neutral molecules in the background gas. Each elementary process is associated with an energy-dependent electron impact cross section, describing in detail how efficient these energy transfer processes are.

Electron impact cross sections can be used with two related, but often non-coincidental, purposes. On the one hand, they can be used to solve the electron Boltzmann equation and obtain an accurate EEDF. In this case, the *full* cross section set must be validated, usually from the comparison of calculated and measured swarm data, *e.g.* electron mobility, diffusion coefficient and Townsend ionization coefficient. Such *consistent* cross section set describes very well the global electron energy transfers on the various energy ranges. However, the individual cross sections considered may contain processes that are not easy to unambiguously identify and/or that correspond to
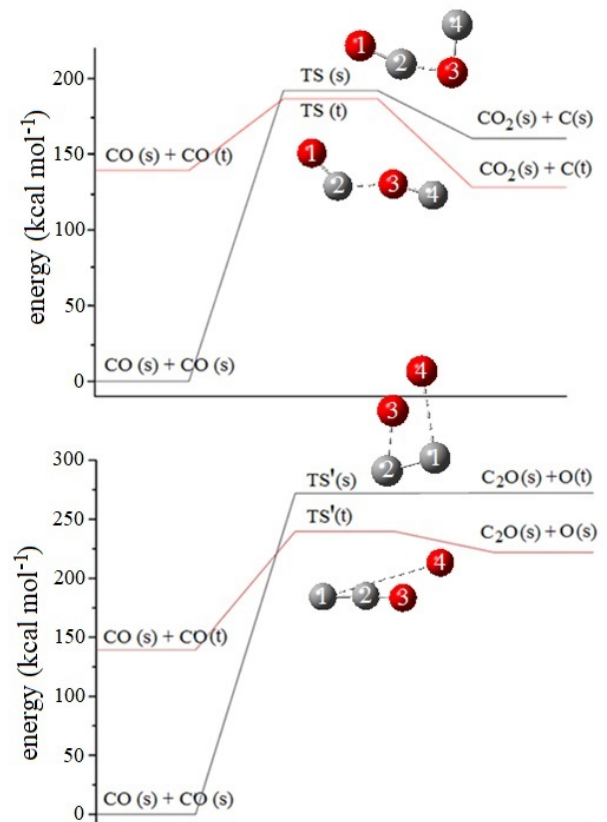
lumped cross sections describing the excitation of several states. On the other hand, they can be used to calculate with precision the electron impact rate coefficient of some specific process, obtained from the integration of the corresponding cross section over the EEDF [184], to be used, *e.g.*, in the interpretation of a particular phenomenon or experiment. Frequently, these cross sections are not part of the complete set. An example is the calculation of the electron impact rate coefficients required to interpret actinometry measurements [185, 186].

It should be clear that the knowledge of a particular cross section with great accuracy should not motivate its blind inclusion or substitution in a consistent set. Indeed, if a very precise measurement or calculation becomes available and this cross section is to become part of a consistent set, a swarm analysis has to be redone, with possible implications on the other cross sections within the set, to ensure the consistency of the set and the correct calculation of the EEDF. It is often preferably to first obtain the EEDF with the previously validated cross section set and only afterwards integrate that particular new cross section over the EEDF to obtain the corresponding rate coefficient.

There are several databases where data on various cross sections can be found. Two open-access databases of relevance for the low-temperature plasma community

Table 1. Values of E_a (in Kcal mol^{-1}), A (in cm^3 mol^{-1} s^{-1}) and α for the reactions in Eq. 15, 16, 17, 18

	E_a(Kcal mol^{-1})	A(cm^3 mol^{-1} s^{-1})	α
CO(s)+CO(s) → CO_2+C	192.76	3.8 10^{13}	0.86
CO(s)+CO(t) → CO_2+C	47.34	4.1 10^{14}	0.45
CO(s)+CO(t) → C_2O+O	273.462	3.5 10^{13}	1
CO(s)+CO(t) → C_2O+O	101.20	1.1 10^{14}	0.85

are the PHYS4ENTRY [57] and LXCat [59] databases. The former has a wealth of information on state-to-state cross sections, while the latter has a larger emphasis on the presentation of complete and consistent cross section sets.

In CO_2 plasmas, CO, O_2 and O may be present with significant concentrations. Therefore, besides CO_2 itself, cross sections for electron impact on these four species are of importance. A brief account of available data and open issues is given in the next few sections.

3.2.1 CO_2

There are several swarm-derived complete cross section sets available in [59]. A new complete and consistent cross section set was derived from a swarm analysis in the last few years by Grofulović *et al* [58, 88]. This cross section set is largely based on the set by Phelps and co-workers [75, 187], with explicit additions from Itikawa [188, 189] and Celiberto *et al* [190–192] regarding the ionization and the vibrational excitation cross sections, respectively. An overview of this cross section set is shown on Figure 7.

The ionization cross sections by Itikawa [188, 189] were used by Stankovich *et al* [193] to calculate the corresponding electron impact rate coefficients in non-equilibrium conditions of a CO_2 plasma sustained by a radio-frequency (RF) electric field. It is shown that in swarm conditions a correct description of the EEDF for reduced electric fields, E/N, below ~ 10 Td is only possible by considering superelastic collisions with vibrationally excited (01^10) molecules [88]. Data from Biagi's Magboltz code [194] were recently added at the LXCat database Biagi-v7.1 [195] and was used by Vialetto *et al* in benchmark Monte Carlo Flux calculations [196]. A brief comparison with data from [88] is also given in [196]. A more detailed comparison of the Biagi cross sections with those from other databases should be done in the near future.

As it is often the case in swarm-derived cross section sets, various cross sections from [75] and from most of the databases available at the LXCat website [59] correspond to lumped processes describing generic energy losses, where the individual processes are not identified [58, 187, 197–199]. This is the case of nearly all the vibrational and electronic excitation cross sections. Regarding vibrational excitation, Celiberto and co-workers calculated the full matrix of cross sections for the electron-impact resonant vibrational excitation within each different vibrational mode up to vibrational quantum numbers of 10 (transitions $v_i \to v_f$ with $0 \leq v_i \leq v_f \leq 10$ on each mode, keeping the other two quantum numbers at
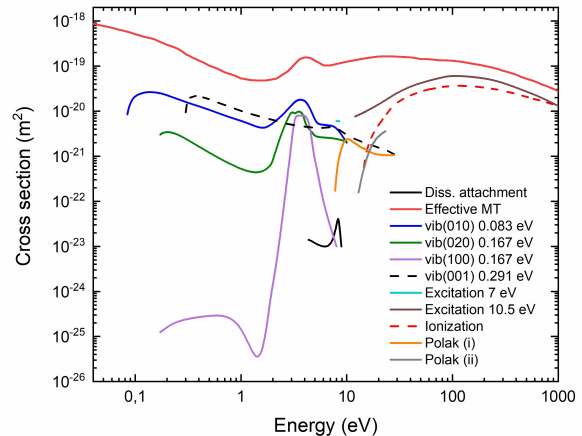

Fig. 7. Overview of the CO_2 electron impact cross section set from [58,88], including the cross sections for: effective momentum transfer (—); dissociative attachment (—); the vibrational excitation of states 010 (—), 020 (—), 100 (—), and 001 (– –); electronic excitation at 7 eV (—) and 10.5 eV (—); and ionization (– –). The figure also includes the cross sections from [200] corresponding to two dissociation channels, with thresholds at ~ 7 eV (—) and 11 eV (—). Additional cross sections and details can be found in [58,88].

0) [190–192]. Note that for the resonant excitation of the bending and asymmetric stretching modes the selection rule $\Delta v = v_f - v_i = 2$ holds. As a consequence, if the data from [190–192] are used in plasma modelling without any addition, no relevant single-quantum transitions are accounted for and the calculated populations of the bending and asymmetric stretch levels surely deviate very strongly from the measured concentrations [200,201]. Nevertheless, the information from [190–192] is invaluable and was used in [88] to partially deconvolute some lumped cross sections, in what has to be seen merely as a first small step in the identification of individual processes. Further studies are needed to obtain the full set of state-dependent cross sections for vibrational excitation, accounting for both resonant and non-resonant contributions.

In what concerns the excitation of electronic states, most complete sets include only two or three cross sections, describing generic losses meant to represent the global excitation of several states. Exceptions are the results in the Biagi [195] and Triniti [199] databases. Of particular interest is the identification of the electron impact dissociation cross section, which in principle is implicitly included in the lumped electronic excitation cross sec-

tions. A detailed analysis of these cross sections is given in [88] and the problem is revisited in [202]. Two main electron impact dissociation channels are available, leading to the formation of either CO or O in an electronically excited state, CO(X)+O(^{1}D) and CO(a)+O(^{3}P), with energy thresholds around 7 and 11 eV, respectively. Different authors use different cross sections to estimate the dissociation rate coefficient. The 7 eV excitation cross section from Phelps [75, 187], as used by [203–205], seems to lead to a reasonable calculation of CO$_2$ dissociation in various conditions [88, 202]. However, in a recent experimental study [89] Morillo-Candas *et al* have shown that electron impact dissociation of CO$_2$ is very well described in the range $E/N \in (45, 105)$ Td by the cross sections calculated by Polak and Slovetsky [206], while the Phelps 7 eV cross section leads to an overestimation of the dissociation rate coefficient. Hence, the dissociation cross section from [206] should be preferably used to calculate the dissociation rate coefficient, even if it is not included explicitly in any consistent cross section set, by direct integration of the EEDF obtained with a consistent set. This procedure does not bring any inconsistency in plasma modelling, as the dissociation cross section is considered to be included as a part of the electronic excitation ones. For values of E/N above ~ 100 Td, it has been very recently suggested that the dissociation cross section from [206] may be underestimated [207]. The argument is based on an approximate analytical theory to calculate the dissociation yield in corona and dbd discharges, associated with the propagation of streamers between the electrodes. According to this theory, for high values of E/N, dissociation could be better described with Phelp's 10.5 eV cross section [187].

The new data available in the Biagi database [195] contains dozens of cross sections for the excitation of electronic states involved in dissociation, assumed to be fully dissociative. These processes are investigated by Vialetto *et al* [196], who conclude that these cross sections somewhat overestimate the dissociation rate coefficient and concur that the cross sections of Polak and Slovetsky [206] are preferred for calculations of the electron impact dissociation rate coefficients. Nevertheless, the data from [195] may help refining the cross sections from [206] in the future.

3.2.2 CO

Complete cross section sets for CO are given in the Triniti [199], Morgan [197], Phelps [187, 208] and IST-Lisbon [58, 209] databases at LXCat. The newest set was developed very recently [209] and is to be used with a two-term Boltzmann solver such as LoKI-B (LisbOn KInetics) [210] or BOLSIG+ [211]. It was constructed based to a large extent on the works of Itikawa [212], Land [208], Hake and Phelps [213], Laporta *et al* [214] and Phelps [215]. In particular, data from [208, 212] were used to construct an elastic momentum transfer cross section and the cross sections for excitation of the electronically excited states, from [213] to build cross sections for rotational excitation

and de-excitation, from [214] to obtain the resonant excitation and de-excitation of vibrational levels, to which a non-resonant contribution to the excitation of $v = 1$ from [213] was added, and from [212] for the processes of dissociative attachment, dissociation and ionization. It includes 15 cross sections for excitation of rotational states of the electronic and vibration ground-state CO($X, v = 0$), 10 cross sections for excitation of vibrational states of the electronic ground state CO(X), and 7 cross sections for excitation of electronically excited states.

The analysis in [209] reveals an inconsistency between the total rotational and effective cross sections reported in the literature, since the effective momentum transfer cross section is lower than the total rotational cross section in the region $10^3 - 10^1$ eV [209]. This inconsistency in the low-energy region is solved in [209] by modifying the first five rotational cross sections and the elastic momentum transfer cross section. The general agreement between measured swarm data and calculations performed with a two-term solver is very satisfactory, validating the use of the set in these conditions. Furthermore, it is shown that even in swarm conditions inelastic and superelastic collisions involving rotationally excited levels, as well as superelastic collisions with the first vibrational excited level, have to be taken into account to accurately calculate the electron energy distribution function. Nevertheless, small discrepancies remain in a narrow region around $E/N \sim 1$ Td. Recent investigation shows that this disagreement stems from the influence of anisotropic scattering, and can be solved by using either an appropriate anisotropic model in a Monte-Carlo calculation or by modifying the two-term solvers to account in an effective way for these effects [216]. This implies that the elastic and rotational cross sections proposed in [209] are not accurate *per se*, but can nevertheless be used in the consistent set to obtain an accurate calculation of the EEDF with a two-term Boltzmann solver. The CO electron impact ionization cross sections of the CO($X^1\Sigma_g^+$) ground state (vibrational state resolved) and of the CO($a^3\Pi$) electronic excited state were calculated by Laricchiuta *et al* [217] by using the binary-encounter-Bethe (BEB) model. The corresponding results are reported in Fig. 8, where the contribution from v=0 and v=40 are displayed. As it can be seen, the ionization cross sections depend on the energy of the excited states (vibrational or electronic) showing different threshold energies (see the insertion detail in Fig. 8) and absolute values.

3.2.3 O$_2$ and O

The electron impact cross sections for O$_2$ and O were recently reviewed in [218, 219]. Only a brief overview is given here and the reader should refer to these papers for further details.

The O$_2$ complete cross section set proposed at the IST-Lisbon database was essentially compiled from [220] and extended using information from [187, 221–223]. Other database include relatively similar cross section sets. Relevant O$_2$ cross sections that are not part of these complete
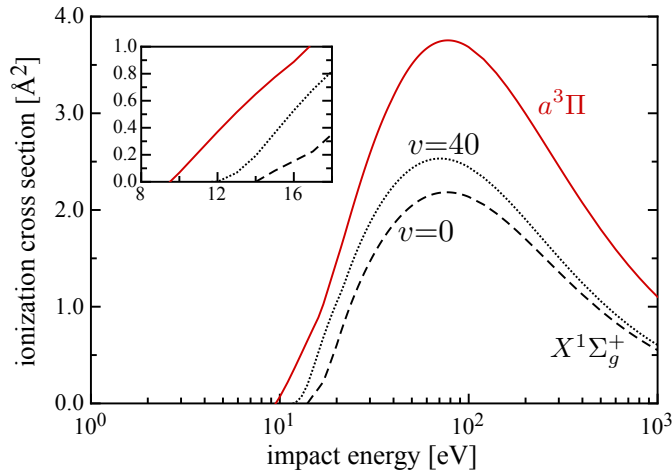
Fig. 8. BEB cross sections for electron impact ionization of the $CO(X^1\Sigma_g^+)$ ground state from v=0 (dashed line) and from v=40 (dotted line) and total ionization cross section for $CO(a^3\Pi)$ calculated by Laricchiuta *et al* [217]. The insertion shows the detail of the different threshold energies.

Fig. 9. Total ionization cross section for the process $O_2(X^3\Sigma_g^-,v)+e \rightarrow O_2^+(X^2\Pi_g, a^4\Pi_u, A^2\Pi_u, b^4\Sigma_g^-)$ as a function of the initial vibrational quantum number for different collision energies, calculated by Kosarim *et al* [236].

sets include: the excitation of $O_2(b\,^1\Sigma_g^+)$ from $O_2(a\,^1\Delta_g)$ [224], $e+O_2(a) \rightarrow e+O_2(b)$; ionization from $O_2(a)$ [225], $e+O_2(a) \rightarrow 2e+O_2^+$; dissociative ionization from $O_2(X)$ [226], $e+O_2(X) \rightarrow 2e+O^++O(^3P)$; dissociative attachment from $O_2(a\,^1\Delta_g)$ [227], $e+O_2(a) \rightarrow O^-+O(^3P)$; electron detachment [228], $e+O^- \rightarrow 2e+O(^3P)$; and the dissociation of ozone [225], $e+O_3 \rightarrow e+O_2(X)+O(^3P)$. In addition, theoretical cross sections are proposed in [229] for the full matrix of e-V transitions up to $v = 42$, while state-dependent dissociative attachment and state-dependent dissociation cross sections are given in [230]. v-dependent cross sections of excitation of $O_2(a,b)$ from $O_2(X)$ were considered in [231]. It is worth noting that the validation of the electron impact dissociation cross section and its v-dependence is still an open problem, with some indications that the dissociation cross sections based on Phelps [220] can be overestimated [232,233].

A complete set of total and dissociative electron impact cross sections of vibrationally excited O_2 molecules through the Schumann-Runge transition, $e + O_2(X^3\Sigma_g^-, v) \rightarrow e + O_2^*(B^3\Sigma_u^-) \rightarrow O(^3P) + O(^1D) + e$, is provided by Laricchiuta *et al* [234] for v up to 30. For the corresponding Herzberg transition, $e + O_2(X^3\Sigma_g^-;v) \rightarrow e + O_2^*(A^3\Sigma_u^+) \rightarrow O(^3P) + O(^3P) + e$, only the cross sections for $v \leq 3$ are available in [235].

Finally, Kosarim *et al* [236] calculated the total electron impact vibrational state resolved ionization cross section of O_2 as the sum of different partial differential cross sections corresponding to different final electronic excited states of the molecular ion O_2^+ $(X^2\Pi_g, a^4\Pi_u, A^2\Pi_u, b^4\Sigma_g^-)$. The results as a function of the initial vibrational quantum number and at different collision energies are reported in Fig. 9.

In what concerns the cross sections for electron impact with oxygen atoms, an important source is the compilation by Laher and Gilmore [237]. The following cross sections
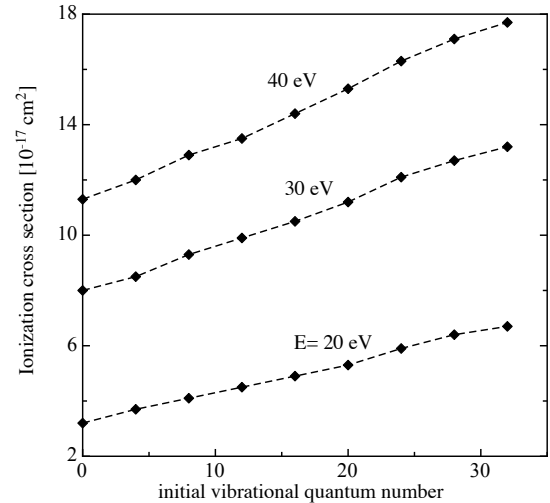
from [237] are included at the IST-Lisbon database [58]: elastic momentum-transfer; excitation of electronic states $O(^1D, ^1S$ and $^3P^0)$; excitation of the most important Rydberg states combined according to their common core, *i.e.* $O(^4S^0)$ representing $O(3s\,^5S^0, 3p\,^5P, 4s\,^3S^0, 3d\,^3D^0, 4p\,^3P$ and $4d\,^3D^0)$, $O(^2D^0)$ representing $O(3d\,^3S^0, 3d\,^3P^0, 3d\,^3D^0, 4d\,^3SPD^0$ and $4s\,^3D^0)$, and $O(^2P^0)$ representing $O(3s\,^3P^0, 3d\,^3P^0$ and $4s\,^3P^0)$; and ionization. A different set of cross sections for electron impact on O is provided by the Triniti database [199].

To conclude this section on elementary collision processes, we would like to stress the need to have complete and accurate state dependent cross-sections and rate coefficient datasets for CO_2 plasma components. In the case of heavy-particle collisions, the SSH, Billing et al. [238] and the FHO theories, at the moment, have provided coherent and extensive data sets for VV and VT exchange processes for the different components of a CO_2 plasma. In our review, we have also reported the calculation of VV and VT rates of CO_2 by using the QCT method with a semi-empirical potential energy surface. A more detailed method for VV and VT processes of O_2-O-N_2 components uses an ab-initio quantum mechanical method for the potential energy surface [239]. No ab-initio calculations exist for the dissociation of CO_2 by heavy-particle impact. In this case, one can use experimental data involving only the ground state. The experimental dissociation results can be corrected by using the Macheret-Fridman semi-empirical method or the generalized Marrone-Treanor model to estimate the role of vibrational excitation on the rates (see sections 5 and 7). The V-V and V-T processes have also recently been investigated in a glow discharge allowing the validation of the rate coefficients of these processes for the low levels of excitation [60,108,240,241]. Nevertheless, it would be particularly interesting to have more experimental data for each individual vibrational level that could be obtained for instance with "pump-probe" experiments.

For electron-impact cross sections, this review has reported a complete and consistent set of cross sections, validated when possible by swarm analysis for the processes in the ground state. The specific case of CO_2 dissociation by direct electron impact on the ground state, which is of particular importance for CO_2 recycling applications, has been investigated experimentally [242]: it was shown that the best effective cross section to describe this process in the low E/N range (between 40 and 100 Td) is the one proposed by Polak and Slovetsky [243]. Semi-empirical methods can be used to describe the dependence of the cross sections on vibrational and electronic energy for direct processes. For resonant electron impact ones, accurate and complete state-specific cross sections are already available in literature for the resonance processes of CO and O_2 [244], but there is not the same level of detail for the CO_2 system for which it is necessary to take into account the coupling of the vibrational modes, going beyond the uncoupled normal-mode model [192].

4 State of the art of 0D kinetic modelling

4.1 General description

The previous section highlighted the inherent complexity of each individual process required to describe CO_2 plasmas. Building on the progress made on the data for each individual collisional process, it is possible to improve a more global description of the kinetics of CO_2 plasmas by developing 0D kinetic models. This type of models, also called global modelling, is very suitable for describing a detailed plasma chemistry, because of its limited calculation time. It is based on solving balance equations for the various plasma species, based on production and loss terms, as defined by chemical reactions:

$$\frac{dn_i}{dt} = \sum_j \left\{ \left(a_{ij}^{(2)} - a_{ij}^{(1)} \right) k_j \prod_l n_l^{a_{ij}^{(1)}} \right\} \quad (24)$$

where $a_{ij}^{(1)}$ and $a_{ij}^{(2)}$ are the stoichiometric coefficients of species i, at the left and right hand side of a reaction j, respectively, n_l is the species density at the left-hand side of the reaction, and k_j is the rate coefficient of reaction j. Typically, the rate coefficients of heavy particle reactions are temperature-dependent and adopted from literature (e.g., NIST database), while the rate coefficients of the electron impact reactions are calculated from the energy-dependent cross sections, in combination with an EEDF, typically calculated with a Boltzmann equation. Besides the species densities, also the electron temperature and gas temperature can be calculated as a function of time, again based on (energy) production and loss terms, defined by chemical reactions (and heating by the electric field, for the electron temperature). Hence, in a 0D model, the plasma composition and other characteristics (electron temperature, gas temperature, etc) are spatially averaged, i.e. their spatial variations are not explicitly taken into account, and they only change as a function of time. This

approximation is good if the plasma is nearly uniform, but global models have also been successfully used to model non-uniform discharges, such as e.g., DBD or ICP. Indeed, although transport by diffusion, migration or convection is often neglected, the temporal variation of the plasma characteristics can be translated into a spatial variation, i.e., as a function of distance travelled through the plasma reactor, based on the gas flow velocity, i.e., equivalence between a batch reactor and a plug flow reactor. In this way, local variations in a plasma reactor, like power deposition, can be mimicked in the model by applying a power deposition profile as a function of time (which corresponds to a residence time of the gas molecules travelling through the reactor). For instance, in a MW plasma, the power deposition is the highest at the position of the waveguide. Likewise, the filamentary behavior of a DBD plasma can be accounted for by applying a number of pulses as a function of time, which represent the microdischarge filaments inside the DBD reactor. When applying this approach, the 0D kinetic model can also be termed as a quasi-1D model. Note, however, that losses by particle transport to the wall (deactivation of metastable and vibrationally excited states at the walls, surface recombination or molecule formation) can also be included in a 0D model, following for instance the approaches proposed in [245–247].

4.2 0D kinetic models developed for CO_2 plasmas

Several groups have developed 0D kinetic models for plasma-based CO_2 conversion. In the 80s and 90s of previous century, some papers reporting CO_2 plasma chemistry modeling were published already, but for applications of CO_2 lasers and without focusing on the vibrational kinetics [150,153,248]. Other papers studied the CO_2 vibrational kinetics for gas flow applications, but without focusing on the plasma chemistry [249,250]. In 1981, Rusanov, Fridman and Sholin were the first to develop a model for CO_2 conversion in a MW plasma, by means of particle and energy conservation equations for the neutral species, and an analytical description of the vibrational distribution function [179]. They reached good agreement with experimental data for the calculated CO_2 conversion and energy efficiency, despite the fact that the model did not yet include the full plasma chemistry with charged species and a self-consistent calculation of the electron density. In the 80s, also the italian group of Molinari and Capitelli [251] showed the importance of including vibrational kinetic modeling for the description of CO_2 dissociation in cold non-equilibrium plasma. They showed the impossibility to rationalize experimental dissociation rates of CO_2 [41] with only the direct electron impact dissociation process, suggesting that another dissociation channel, i.e. that one induced by vibrational excitation, had to be taken into account to describe CO_2 dissociation in non-equilibrium plasma.

In the last two decades, the research on plasma-based CO_2 conversion gained renewed interest, and several plasma chemistry models have been presented in literature, for various plasma types. Typically, the focus was on the role

of the CO$_2$ vibrational levels, as they play a crucial role in energy-efficient CO$_2$ dissociation. We provide here a brief overview, while some typical calculation results will be presented in section 4.3. The group PLASMANT at the University of Antwerp has been pioneering in 0D kinetic modelling of CO$_2$ plasmas [252, 253]. In 2012, Aerts et al. developed a CO$_2$ model for a DBD plasma, which included 8 neutral species (ground state molecules of CO$_2$, CO and O$_2$, as well as radicals), 4 CO$_2$ vibrational and 2 electronic levels, 1 CO vibrational and 4 electronic levels, and 3 O$_2$ vibrational and 2 electronic levels, as well as 11 different positive ions and 6 different negative ions [254]. These species were able to react in 501 different reactions (including various electron impact, ion and neutral reactions). In 2015, the authors extended this model to a large number of microdischarge filaments, describing the CO$_2$ conversion for the actual residence time in a DBD plasma reactor, and comparison with experimental data showed good agreement [255]. In addition, the authors developed a reduced model, considering only 9 different species, i.e., CO$_2$, CO, O, O$_2$, and O$_3$ as neutral species and CO$_2^+$, O$_2^-$, O$^-$, and the electrons as charged species, which react in only 17 different reactions. No vibrationally or electronically excited levels were included in this model, because vibration-induced dissociation was considered of minor importance in a DBD plasma.

In 2014, Kozak and Bogaerts [118] developed a more extensive CO$_2$ model, with major focus on the CO$_2$ vibrational kinetics, and especially the asymmetric stretch mode, which is stated to be most important for CO$_2$ splitting [40]. The species included in the model were the same as in Aerts et al. [254], but with major extension of the CO$_2$ and CO vibrational levels. Indeed, 21 vibrational levels of the CO$_2$ asymmetric stretch mode, i.e., up to the dissociation limit of the molecule, were taken into account, but only 4 effective (combined) levels of the symmetric stretch and bending modes. In addition, 10 CO vibrational levels were included. A detailed description was provided of the state-specific vibration-translation (VT) and vibration-vibration (VV) relaxation reactions, as well as the effect of vibrational excitation on the other chemical reactions. The model was applied to both a DBD plasma (operating at atmospheric pressure), and a microwave (MW) plasma, operating at moderate pressure (20 Torr). In 2015, the authors extended this model to 63 vibrational levels of CO, and applied it in more detail to a MW plasma, to study the effect of various plasma parameters, such as the reduced electric field, electron density and the specific energy input, on the CO$_2$ conversion and energy efficiency [256]. The highest energy efficiency was reported for an SEI around 0.4-1.0 eV/molec and a reduced electric field of 50-100 Td, and for high electron densities (ionization degree greater than 10^{-5}). The model also revealed that the energy efficiency is mainly limited by VT relaxation, giving rise to vibrational energy losses and simultaneous gas heating.

Berthelot and Bogaerts reduced the Kozak-Bogaerts CO$_2$ plasma chemistry model, by lumping the CO$_2$ vibrational levels into a few groups [257]. The model was applied to typical conditions of a MW plasma (i.e., gas pressure between 15 and 750 Torr), and gas temperature rising from 300 to 3000 K). A three-groups model was able to reproduce the shape of the CO$_2$ vibrational distribution function (VDF) and gave the most reliable prediction of the CO$_2$ conversion. The three-groups model was based on a level-lumping procedure in which the 21 vibrational levels of the CO$_2$ asymmetric stretch mode of the kind (0 0 v), instead of being considered separately, were divided into three different groups (group 1: v=1-3; group 2: v=4-14; group 3: v=15-21) and described by a Boltzmann distribution at three different vibrational temperatures. Such a chemistry reduction is required when aiming to describe CO$_2$ plasmas by more-dimensional models (see section 9). The applicability of this level-lumping method was demonstrated by Wang et al., using the same CO$_2$ kinetics model, to describe a classical GA plasma in a 1D framework [258]. The model accounted for the loss of plasma species and heat due to convection by the transverse gas flow, by means of a characteristic frequency of convective cooling, which depends on the gliding arc radius, the relative velocity of the gas flow with respect to the arc and the arc elongation rate.

Other reduction methods were also proposed in literature. Peerenboom et al. applied a dimension reduction method to the above CO$_2$ plasma chemistry model, based on principal component analysis [259]. The reduced model considered only two principal components, and was able to predict the CO$_2$ conversion at varying ionization degrees. de la Fuenta et al. presented a reduction method for the above CO$_2$ plasma chemistry model, based on four key elements: (1) all asymmetric mode vibrational levels were lumped in a single group, which (2) followed a Treanor distribution, (3) the vibrational temperature was calculated from the translational temperature by means of the Landau-Teller formula, and (4) weighted algebraic expressions instead of complex differential equations were used to calculate the rates of the most important reactions, which significantly reduced the calculation time [260]. The reduced set contains 13 species and 44 reactions, and the calculation results were in good agreement with the full Kozak-Bogaerts model. Diomede et al. proposed a method based on solving the non-linear Fokker-Planck equation by the time-dependent diffusion Monte Carlo method [261]. The transport quantities were calculated from the state-to-state rate coefficients of the Kozak-Bogaerts model. This method could reproduce the VDF predicted by the Kozak-Bogaerts model or a Treanor distribution, depending on the choice of the boundary conditions. This approach was further validated by Viegas et al. for the vibrational kinetics of the CO$_2$ asymmetric stretch mode, and shown to be around 1000 times faster than the usual state-to-state method, for calculating the VDF in stationary conditions [262]. In [263], the authors presented an improvement, by a self-consistent numerical solution, which avoids the approximations used in the previous analytical solutions. Finally, Sun et al. applied a chemistry reduction method to the Kozak-Bogaerts model, based on the so-called directed relation graph method [264]. This re-

sulted in a reduced CO$_2$ kinetics model, consisting of 36 or 15 species (depending on whether the 21 asymmetric mode vibrational CO$_2$ levels were explicitly included or lumped into one group), that was applied to a GA plasma. The results of this reduced model were also in very good agreement with those of the full chemistry model. Hence, this reduced chemistry set was also implemented in a 2D model, to describe a low power GA plasma (see also section 9).

The Bari group (Pietanza, Colonna, Capitelli, et al.) also developed several models to study CO$_2$ dissociation in non-equilibrium discharge and post-discharge conditions [205, 265–274], with focus on electron kinetics (see section 5) and by using a similar vibrational model for the CO$_2$ asymmetric stretch mode as the Kozak-Bogaerts model [118, 256]. In particular, they underlined the importance of implementing a time-dependent self-consistent coupling of the electron Boltzmann equation for the EEDF calculation with the state-to-state vibrational and electronic excited state kinetics of the CO$_2$ plasma mixture species [205, 265–269, 273, 274]. Special emphasis was addressed to the effect of superelastic electronic and vibrational collisions in affecting the EEDF and the reaction rates. The authors also developed a detailed state-to-state model for the vibrational and electronic excited state kinetics of CO [270–272], as well as O$_2$ molecules [275].

The Lisbon group (Silva, Grofulovic, Guerra, et al.) developed another CO$_2$ vibrational kinetics model, with less focus on the asymmetric stretch mode, but more details for the symmetric stretch and bending modes [61, 62] (see section 6). They calculated the time evolution of 70 individual CO$_2(X^1\Sigma^+)$ vibrational levels during the afterglow of a pulsed DC glow discharge, to study the vibrational energy transfer in CO$_2$ plasmas. They compared the calculated vibrational and gas temperatures with in situ FTIR experiments, performed at low pressure (few Torr, 50 mA), and obtained very good agreement, which validated the kinetic scheme and the VV and VT rate coefficients, and provided insight in the reaction mechanism for the vibrational kinetics of CO$_2$ [61]. In [62], their model was further extended with electron impact vibrational excitation and de-excitation (eV). The time-dependent calculated densities of the vibrational levels were compared with time-resolved in situ FTIR, and good agreement was reached, validating the eV rate coefficients. In general, the Lisbon model can be considered complementary to the Kozak-Bogaerts model, and in the future, efforts should be made to combine both models, for a comprehensive description of the CO$_2$ vibrational kinetics, including all vibrational modes.

A more complete vibrational energy ladder for CO$_2$ was developed by Armenise and Kustova for the investigation of CO$_2$ non-equilibrium vibrational kinetics in the hypersonic boundary layer of reentering bodies in Mars atmosphere [46, 276–279] (see also section 7). Although their model does not consider plasma, i.e. only preliminary studies of the electron impact processes have been performed [280], they take into account symmetric, bending and asymmetric vibrational levels with all possible combination of their quantum numbers up to a threshold energy of 3 eV, fixed by computational resource limits. The application of this model to the description of CO$_2$ dissociation in plasma discharges could give more insights to the contribution of symmetric and bending modes for the CO$_2$ dissociation, but, at the moment, it is limited by the huge computational cost needed due to a necessary extension to higher threshold energies, i.e. at least up to the dissociation limit of 5.5 eV, and by the lack of electron impact cross sections data for all the vibrational energy levels considered to be included in the electron kinetics. A somewhat similar approach is followed by Bultel and co-workers [281].

Other groups also presented some CO$_2$ plasma chemistry models, based on 0D or 1D fluid models. Cheng et al. applied a 0D kinetic model, based on the Kozak-Bogaerts chemistry set, to a micro-hollow cathode discharge, and reported that electron impact dissociation and heavy species impact dissociation are dominant in different stages of the micro-hollow cathode discharge process for a given applied voltage [282]. Ponduri et al. applied a 1D fluid model with extensive reaction kinetics for the CO$_2$ vibrational levels (i.e., all asymmetric mode levels up to the dissociation limit, and several symmetric mode levels) to a DBD plasma with plane-parallel electrodes [283]. The model revealed that CO was mainly produced during the microdischarge pulses, due to electron impact dissociation. Finally, Moss et al. presented a combination of a 1D fluid model and 0D kinetic model to a ns-pulsed corona discharge in pure CO$_2$ and its mixture with argon [284]. The 1D model treated a single pulsed discharge, and its results were used in the 0D model for the detailed plasma chemistry over long times. The CO$_2$ vibrational kinetics was based on the model by Aerts et al. [254]. The process of CO$_2$ splitting was found to proceed in two phases: the first phase generated a high electron density upon ionization, while the second phase was dominated by direct electron impact dissociation of CO$_2$.

It should be realized that 0D kinetic models contain a lot of different cross sections and rate coefficients, which are not always precisely known. In particular, there are some uncertainties on the most appropriate CO$_2$ electron impact dissociation cross section to be used in the models. Bogaerts et al., [202] as well as Morillo-Candas et al. [89] applied their 0D kinetic models to evaluate several different CO$_2$ electron impact dissociation cross sections available in literature, and both groups showed large differences in the results, depending on which cross section was used. Koelman et al. thoroughly verified all reactions and rate coefficients in the Kozak-Bogaerts model, and compared the chemistry sets implemented in ZDPlasKin and PLASIMO, showing good agreement between both codes [285]. Finally, because the error on the rate coefficients can propagate to the model output, Berthelot and Bogaerts applied a Monte Carlo procedure, based on 400 different combinations of rate coefficients, to evaluate the effect of the uncertainties in the rate coefficients on the calculation results [286]. While the uncertainties were only about 15% for the calculated electron density and temper-

ature, they could rise up to 100% for the calculated CO_2 conversion. Nevertheless, for all conditions evaluated, the trends observed in previous modeling work were still valid.

Besides kinetic models for pure CO_2 plasmas, several models have been developed as well for mixtures of CO_2 with other gases, e.g., CO_2/CH_4 [287–289], CO_2/N_2 [5, 94,290], CO_2/H_2 [291], CO_2/H_2O [292,293], and all combinations $(CO_2/CH_4/N_2/O_2/H_2O)$ [294,295], for various types of plasmas (DBD, MW, GA plasmas) studying the underlying chemistry, but we will not go in more detail, as the focus is here on pure CO_2 plasmas.

4.3 Insights obtained from 0D kinetic models of CO_2 plasmas

Because 0D kinetic models describe a detailed plasma chemistry, they can provide very useful information on the underlying chemistry of CO_2 conversion in various plasma types. Aerts et al. [254,255] predicted that for typical DBD conditions, electron impact dissociation was the most important, mainly from the CO_2 ground state, while the vibrationally excited CO_2 levels contributed for only 6.4 % to the CO_2 splitting. However, this was predicted when only considering one microdischarge pulse and its afterglow, while a DBD consists of many successive microdischarge pulses, and the calculations revealed that the vibrationally excited CO_2 levels can accumulate during such successive microdischarge pulses, so the role of vibrational-induced CO_2 dissociation can be larger. The main pathways for CO_2 dissociation in a DBD plasma, as revealed by this model, are depicted in Fig. 10. The main reactions are electron impact dissociation into CO and O, electron impact ionization into CO_2^+, which recombines with electrons or O_2^- ions into CO and O and/or O_2, and electron dissociative attachment into CO and O^- (black thick lines in Fig. 10). The CO molecules are relatively stable, but they can also recombine with O^- ions or O atoms, to form again CO_2 (thin black lines in Fig. 10). This explains why the CO_2 conversion typically tends to saturate at long enough residence times. In addition, the O atoms will almost immediately recombine into O_2 or O_3, and several other reactions can occur between O, O_2 and O_3, as well as the O^- and O_2^- ions (red lines in Fig. 10).

Kozak and Bogaerts applied their model to both DBD and low-pressure MW plasma, and demonstrated that the CO_2 conversion and energy efficiency were very different in both plasma types, due to the different CO_2 dissociation mechanisms [118]. Indeed, vibration-induced dissociation was found very important in the low-pressure MW plasma, while it was of minor importance at the DBD conditions, explaining the much higher energy efficiency in the MW plasma than in the DBD, in accordance with literature (e.g., [296]). This difference is schematically illustrated in Fig. 11, which presents a few CO_2 electronic and vibrational levels. In a DBD plasma, direct electron impact dissociation is found most important, and it typically proceeds through a dissociative electronically excited level, so it requires electron energies of 7-12 eV. However, theoretically only 5.5 eV is required for C=O bond breaking, so the
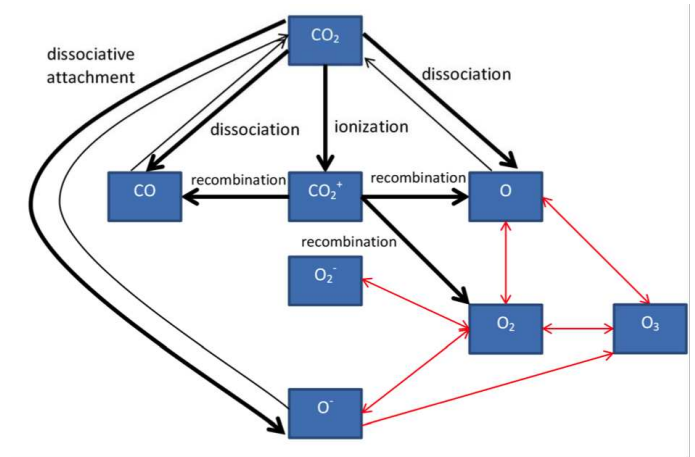

Fig. 10. Simplified chemical reaction scheme of CO_2 splitting and the further reactions between O, O_2 and O_3 in a DBD plasma, as predicted by the model in [255]. The thick black arrow lines represent the most important reactions for CO_2 splitting (mostly attributed to electron impact). The thin black arrow lines point towards the opposite reactions, i.e., recombination of CO with either O^- ions or O atoms, into CO_2. The red arrow lines indicate the conversions between O, O_2 and O_3. Adopted from [252] with permission.

extra energy is simply wasted, explaining the lower energy efficiency for CO_2 splitting in DBD plasma. In contrast, vibrational excitation requires less energy (i.e., below 1 eV for the lowest levels), and the lowest vibrational levels gradually populate the higher levels by VV relaxation (also called ladder-climbing), which leads to dissociation at just the minimum amount of 5.5 eV needed for bond breaking. Hence, vibration-induced dissociation, which occurs in low-pressure MW plasmas, provides a more efficient dissociation pathway, explaining its better energy efficiency. For this reason, many authors focused on the vibrational kinetics in CO_2 0D plasma kinetic models (e.g., [61,62,89,118,202,205,256–272,274,282–286,297–302])

Berthelot and Bogaerts applied the Kozak-Bogaerts model to a CO_2 MW plasma in a wide range of gas pressure, temperature and power density, focusing on the VDF and CO_2 dissociation mechanisms [297]. Lower pressures and temperatures, and higher power densities, resulted in a stronger vibrational-translational (VT) non-equilibrium, i.e., higher vibrational than gas (translational) temperature, also demonstrated by a non-Maxwellian VDF, with clear overpopulation of the higher vibrational levels, which is beneficial for energy-efficient CO_2 conversion through vibration-induced dissociation. This is illustrated in Fig. 12, where the calculated VDF is plotted at 300 K (a) and 2000 K (b), for both low pressure (37.5 Torr) and atmospheric pressure; the power density was adapted to the pressure (see [297] for details). At 300 K, the VDF exhibits a clear plateau shape in the entire pressure range, characteristic of the VT non-equilibrium, but the plateau is higher at lower pressures, because there are less collisions and thus less VT relaxation. At 2000 K, the VDF is nearly thermal (especially at atmospheric pressure), due to the strong VT
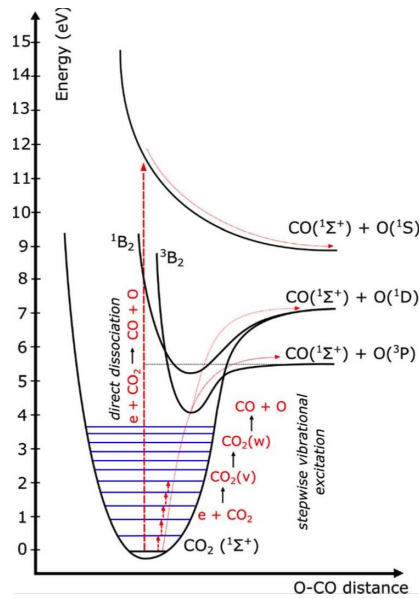
Fig. 11. Schematic picture of some CO_2 electronic and vibrational levels, showing that direct electronic excitation-dissociation (which is predominant in DBD plasmas) requires much more energy than stepwise vibrational excitation (also called vibrational ladder climbing), which is stated to be important in low-pressure MW plasmas. Adopted from [42] with permission.

relaxation. These VDF results were confirmed by Pietanza et al. in [273].

Fig. 13 summarizes the main mechanisms leading to CO_2 conversion, as predicted by the model of Berthelot and Bogaerts [297], at either non-equilibrium conditions (low gas pressure and temperature, and high power density) (a), and equilibrium conditions (high gas pressure and temperature, and low power density) (b). At the non-equilibrium conditions, there is pronounced electron impact vibrational excitation, and VV relaxation, populating the higher vibrational levels, and limited VT relaxation, yielding a non-thermal VDF (see Fig. 12 a). The CO_2 dissociation occurs equally upon collision with any neutrals and upon collision with O atoms, and there is limited recombination, due to the low temperature. On the other hand, at equilibrium conditions, the VDF is thermal (see Fig. 12 b), due to higher VT relaxation, which also causes significant gas heating. Finally, the high temperature causes recombination to be more important, limiting the overall conversion.

Berthelot and Bogaerts also applied the above model to track the different energy transfers taking place in a CO_2 plasma, for different conditions of reduced electric field, gas temperature and ionization degree, at a gas pressure of 75 Torr [298]. The highest conversion and energy efficiency were predicted at a low reduced electric field (10 Td) and a low gas temperature (300 K), again due to the more pronounced vibration-induced dissociation. In addition, the authors revealed that the efficiency by which the vibrational energy is used for CO_2 dissociation, as well as the activation energy of the reaction $CO_2 + O \rightarrow CO +$
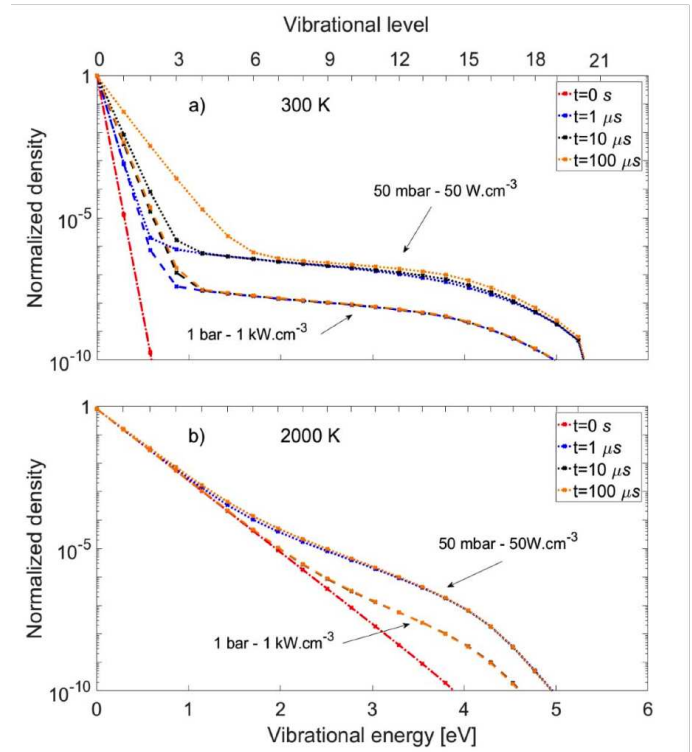

Fig. 12. Calculated vibrational distribution functions (VDFs) of the CO_2 asymmetric stretch mode, at different times (see legend) for a gas temperature of 300 K (a) and 2000 K (b), and two different pressures and power densities. Adopted from [297] with permission.
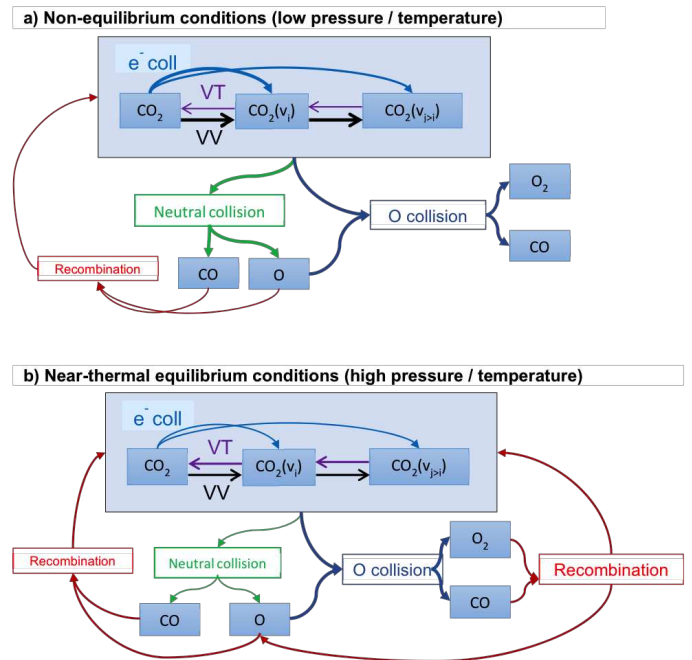

Fig. 13. Dominant reaction pathways of CO_2 splitting, predicted by the model in [297], for non-equilibrium conditions of low pressure and temperature (a), and near-thermal condition of high pressure and temperature. The thickness of the arrow lines indicates the importance of the process.

O_2, are the main limiting factors for the energy efficiency. Indeed, the vibrational energy required to overcome this activation energy barrier is high and the excess energy is typically wasted to heat. It must be mentioned that the VDFs plotted in Fig. 12 were calculated by keeping the temperature fixed. Normally, a higher power density would also lead to a higher gas temperature, leading to more VT relaxation, which will cause further gas heating, as well as depopulation of the higher vibrational levels, and is thus detrimental for vibration-induced dissociation. Thus, in the ideal case of strong VT non-equilibrium, a high power density must be accompanied by a controlled (low) gas temperature. This is however very difficult to realize in practice. In addition, for practical (industrial) applications, atmospheric pressure operation is desirable, which also gives rise to mainly thermal conversion (see further).

Vermeiren and Bogaerts applied the Kozak-Bogaerts model, but with sligthly updated chemistry (see details in the corresponding references), to study how the vibration-induced dissociation pathway can be enhanced, more specifically by supersonic expansion [299] and power pulsing [300]. Combining the model with computational fluid dynamics simulations for the gas flow behavior in a MW CO_2 plasma with Laval nozzle, the authors revealed that supersonic expansion can indeed lead to a VT non-equilibrium in the supersonic acceleration region due to a local drop in gas temperature and pressure, while the inlet and outlet pressure can still be atmospheric (or above), being compatible with industrial operations. However, after the shockwave, the gas pressure and temperature rise again, and the VDF becomes thermal, thus limiting the overall enhancement in energy efficiency. Furthermore, the short residence time of the gas in the plasma region, the shockwave, and the maximum critical heat, and thus power, that can be added to the flow to avoid thermal choking, were found the main obstacles to reaching high energy efficiencies [299]. With respect to pulsing, the authors showed that the highest energy efficiencies can be reached by correctly tuning the plasma pulse and interpulse times. The optimal plasma pulse time, at a reduced pressure of 100 mbar, was found to be around 60 μs, which corresponds to the time needed to reach the highest vibrational temperature (i.e., allowing enough time for the VDF to build up to the highest levels), but not too long, to avoid that the gas temperature would rise as well. At the same time, the interpulse times have to be long enough, i.e., above 0.1 s, so that the gas temperature can entirely drop to room temperature [300]. It has to be realized, however, that in practice, when the pulse-off times are too long, the CO_2 gas would not experience enough pulses within its residence time in the plasma, for sufficient dissociation. In practice, VT relaxation appears quite important in both MW plasmas (at (sub)atmospheric pressure) and GA plasmas, explaining their high gas temperature (3000 K or higher). For this reason, the CO_2 conversion proceeds mainly by thermal reactions in MW and GA plasmas at practical operating conditions, as demonstrated by several models [274, 297, 301–305]. However, Pietanza et al.

recently studied in detail the kinetics vs thermodynamics effects on CO_2 dissociation in high-temperature MW plasmas, with a self-consistent model of the vibrational kinetics of CO_2, CO and O_2, and the electron Boltzmann equation, and they concluded that the assumption of thermodynamic equilibrium in MW CO_2 high temperature plasmas has to be considered with caution, as there are still non-equilibrium effects at play, even at temperatures of 3500-5500 K [274].

Sun et al. applied the Kozak-Bogaerts model to CO_2 splitting in a classical GA plasma (operating at atmospheric pressure), and compared the calculated conversion and energy efficiency with experiments in a range of different operating conditions [301]. Good agreement was reached, so that the model could be used for a reaction pathway analysis, and to pinpoint the limiting factors for the CO_2 conversion. The latter were identified as the reverse reactions (recombination of CO and O, forming CO_2 again) and the small treated gas fraction by the arc. Hence, the authors proposed solutions to overcome these limitations, such as a lower gas temperature, a high frequency discharge, or a higher power density, e.g., by using a micro-scale GA reactor. Also the effect of removing the reverse reactions was evaluated, and showed a large effect on the conversion performance. However, these simulations were only suggested theoretically, and will need to be evaluated in practice.

Kotov and Koelman applied a similar 0D model to a CO_2 MW plasma at reduced pressure (5-100 Torr), and studied the energy redistribution pathways [302]. Despite the fact that the power was initially mainly deposited into the vibrational levels, fast VT transfer caused significant gas heating, and the CO_2 dissociation was revealed to be mainly thermal. Viegas et al. applied a 0D model to describe the plasma chemistry in the core of a vortex-stabilized MW CO_2 plasma, focusing on the pressure-dependent contraction dynamics, in the pressure range between 45 and 225 Torr and temperature range between 3000 and 6500 K [304]. The authors self-consistently coupled the plasma chemistry model with Monte Carlo flux simulations to describe the electron kinetics. The simulation results showed that a rising pressure causes a transition in neutral composition in the plasma core, i.e., from mainly CO_2 and O_2 at low pressures, to a O/CO/C mixture at high pressures, determined mostly by thermal equilibrium and transport processes. This also causes a higher ionization degree in the plasma core (from 10^{-5} to 10^{-4}), which was shown fundamental to drive contraction in a CO_2 MW plasma.

Heijkers and Bogaerts applied the Kozak-Bogaerts model to a gliding arc plasmatron (GAP) and also obtained good agreement between the calculated and experimental conversions and energy efficiencies [306]. They predicted vibration-induced dissociation as the main dissociation mechanism of CO_2, but it occurred mainly from the lowest vibrational levels, because of fast thermalization of the VDF. In other words, the CO_2 conversion at these atmospheric pressure conditions was found to proceed by thermal dissociation. The same authors also applied this model to a ns-

pulsed plasma, and the calculated conversions and energy efficiencies were again in reasonable agreement with experimental results over a wide range of SEI values [307]. Also the time-evolution of the gas temperature and CO$_2$ conversion were in good agreement with the measurements. Vibrational excitation was found to be very important in this ns-pulsed plasma, because of the strong non-equilibrium conditions. A significant part of the CO$_2$ dissociation occurs by electronic excitation-dissociation from the lower vibrational levels. However, VT relaxation and CO + O recombination were again identified as limiting factors for the CO$_2$ conversion and energy efficiency. In addition, another limiting factor was the mixing of the converted gas with fresh gas entering the plasma in between the pulses. The model revealed that extra cooling, slowing down the VT relaxation and the recombination of CO with O atoms, may further enhance the performance. Pannier et al. also studied a ns-pulsed CO$_2$ plasma, in both glow and spark regime, by means of a 0D kinetic model, including the vibrational kinetics of CO and CO$_2$, but also paying particular attention to the CO$_2$ electronic states [308]. Vibrational excitation was stated to be important in the glow regime, but did not translate into significant conversion, while the high electron impact electronic excitation of CO$_2$ and the limited gas heating in the spark regime gave rise to a higher conversion and energy efficiency. Recently, there is growing insight that optimizing the vibration-induced dissociation pathway may not be the most realistic strategy at practical (sub)atmospheric MW and GA plasmas. In fact, experiments indicated that thermal CO$_2$ conversion gives rise to quite high energy efficiencies (up to 40-50%) [7, 8, 309, 310]. Indeed, the rate coefficients of thermal reactions rise with gas temperature, thus enhancing the conversion. Wolf claimed that temperatures around 3000-4000 K are optimal for thermal conversion, to realize significant CO$_2$ conversion at limited thermal losses [311]. Instead of trying to exploit the VT non-equilibrium, which might not be feasible at practical (sub)atmospheric MW and GA plasmas, it may thus be wiser to focus on how to improve the energy efficiency beyond the thermal equilibrium limit [310]. Vermeiren and Bogaerts compared in detail the performance of plasma-induced and thermal CO$_2$ dissociation for a wide range of SEI values, and demonstrated that for warm plasmas, such as (sub)atmospheric pressure MW and GA plasmas, with typical temperatures of 3000-4000 K, the conversion is indeed thermal [305]. Furthermore, the authors examined the effect of cooling/quenching, during and after the plasma, on the CO$_2$ conversion and energy efficiency, and to explain the behavior, they studied in detail the dissociation and recombination rates, as well as the VDFs of CO$_2$, CO, and O$_2$.

Fig. 14 illustrates the conversion (a) and energy efficiency (b) (both left axes) as a function of SEI, for both plasma-induced and thermal conversion, with and without quenching. In the thermal case, the same power is applied as in the plasma case, but simply as heat. The maximum gas temperature is also shown for both the plasma and thermal conditions (right axes). For SEI values
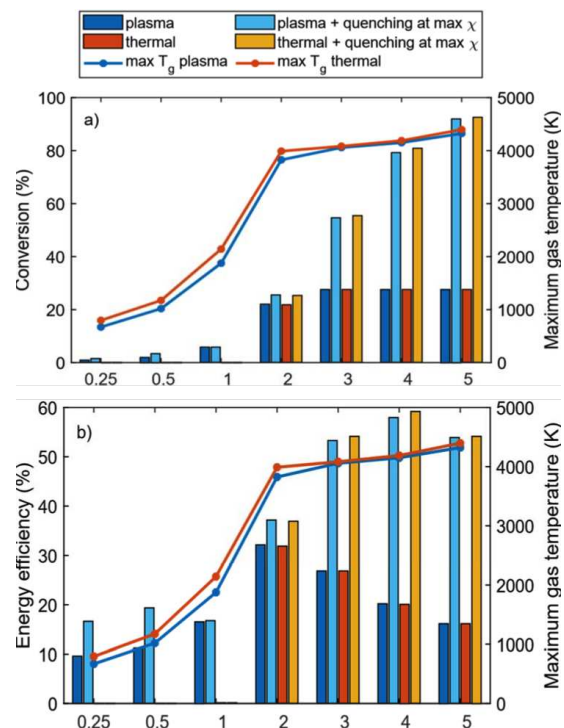

Fig. 14. Calculated CO$_2$ conversion (a; left axis) and energy efficiency (b; left axis) and maximum gas temperature (right axes) as a function of SEI, calculated with the model of [305], for warm plasma conditions, as well as pure thermal conversion, with and without quenching. Adopted from [305] with permission.

≤ 1 eV/molec, the maximum gas temperature is too low for thermal CO$_2$ dissociation. Hence, the thermal process shows negligible conversion. The plasma process exhibits a conversion of about 0.8-5.6%, yielding an energy efficiency of 9.5-16.5%. This is mostly attributed to vibration-induced dissociation. For SEI values ≥ 2 eV/molec, the thermal conversion and corresponding energy efficiency rise, and they are similar to the plasma process, both with and without quenching. Furthermore, the maximum gas temperatures in both cases are also quite similar, due to the high VT relaxation, resulting in VT equilibrium in the plasma. Without quenching, the final CO$_2$ conversion is around 27-28%, due to the slow cooling, which promotes recombination reactions. Upon quenching, both the plasma-induced and thermal conversion and their corresponding energy efficiencies rise dramatically, because the recombination reactions are inhibited at the low gas temperature, thus "freezing" the conversion obtained at the end of the plasma (or thermal case).

Thus, it is clear that quenching after the plasma can greatly enhance the final CO$_2$ conversion. The authors even demonstrated that quenching can also increase the conversion beyond the dissociation in the plasma, known as super-ideal quenching. Indeed, the O atoms, formed by CO$_2$ splitting, can react with another CO$_2$ molecule (CO$_2$ + O $\rightarrow$ CO + O$_2$), instead of recombining with CO, thus making full use of the dissociation products. As mentioned

above, this reaction was pinpointed as the major limiting factor for energy-efficient CO_2 conversion, because of its high energy barrier [298]. However, when CO_2 molecules leave the hot plasma zone and are subject to cooling in the afterglow (or plasma edge) while keeping their high vibrational population (i.e., freezing the VDF), a VT non-equilibrium can be established, because VT relaxation is much slower in this cooler region. This vibrational over-population of CO_2 in the cooler afterglow could then overcome the high energy barrier of the above reaction with O atoms and produce additional CO. The recycling of O atoms through reaction with vibrationally excited CO_2 molecules was also suggested by Silva et al. [312] in a MW post-discharge. This super-ideal quenching may explain the energy efficiencies above the thermal equilibrium limits reported in the 1980s [313, 314]. However, it has to be noted that the reaction $CO_2(v)+O \rightarrow CO+O_2$ has never been proven experimentally, as pointed out in section 2.2. In addition, instead of reacting with vibrationally excited CO_2 molecules, O atoms can quench the vibrationally excited CO_2 molecules in very effective VT exchanges and remove internal energy into gas heating. This effect was recently evinced experimentally in [108] (see also section 8) and in simulations [39]. Moreover, O atoms and O_2 molecules can participate in back reactions converting CO into CO_2. An alternative pathway to dissociation could involve the participation of $O(^1D)$ metastable atoms, but it also remains unproven to date. Thus, the role of O atoms is somewhat ambivalent, with promises of positive and negative effects in dissociation, depending on the exact operating conditions, that still require further clarification.

5 Electron kinetics: importance of the self-consistent approach

In this section, we focus on the electron kinetics and on the importance of implementing a self-consistent approach for the solution of the electron Boltzmann equation for the calculation of the EEDF and the state-to-state (STS) plasma kinetics equations, describing the vibrational, the electronic excited states and the plasma chemistry of heavy particles in CO_2 cold plasmas in discharge and post-discharge conditions. The electrons have a key role in CO_2 conversion in non-equilibrium plasma discharges. After gaining energy from the electric field, they transfer part of their energy to atoms and molecules, pumping vibrational and electronic excited states through electron impact excitation collisions, i.e. inelastic collisions, and promoting CO_2 reactive channels, such as ionization and dissociation, even at low gas temperature. Vibrational and electronic excited states, in turn, give energy back to the electrons thanks to superelastic or second-kind collisions, affecting the EEDF shape and, as a consequence, the electron impact reaction rates. The gained energy in the CO_2 vibrational excitation by electron collisions (i.e. by eV collisions) is spread over the whole vibrational ladder thank to vibrational-vibrational (VV) collisions, which contribute in increasing the vibrational excitation at higher vibrational levels,

creating, in particular conditions, long non-equilibrium plateaux in the CO_2 VDF and promoting CO_2 dissociation. The described scenario confirms the strong coupling between the electron, the vibrational, the electronic excited state and the plasma kinetics, underlying the importance of using a self-consistent approach for the solution of the corresponding kinetic equations. Plasma discharges are also characterized by switched on and off conditions for the electric power density applied, requiring a time-dependent solution of the kinetic equations.

5.1 General equations

The general equations governing the time dependent behavior of the different quantities operating in a reactive plasma mixture are the followings:

1. the electron Boltzmann equation describing the electron kinetics

$$\frac{\partial n(\epsilon,t)}{\partial t} = -\left(\frac{\partial J_E}{\partial t}\right) - \left(\frac{\partial J_{el}}{\partial t}\right) - \left(\frac{\partial J_{ee}}{\partial t}\right) + S_{in} + S_{sup} + S_{rct,f} + S_{rct,b}$$

(25)

where $n(\epsilon,t)$ represent the number density of electrons with energy between ϵ and $\epsilon + d\epsilon$, linked to the $f(\epsilon,t)$, i.e. the EEDF in $eV^{-3/2}$, by $f(\epsilon,t) = \frac{n(\epsilon,t)}{n_e(t)}\epsilon^{-3/2}$, where $n_e(t)$ is the total electron number density. The first three terms, on the right-hand side of Eq. (25), correspond to fluxes of the electrons along the energy axis due to the electric field (J_E), elastic electron-molecule (J_{el}) and electron-electron (J_{ee}) collisions, while the last two source terms are due to inelastic (S_{in}) and superelastic (S_{sup}) (vibrational and electronic) collisions and to electron-induced chemical reactions, such as ionization and dissociation processes, in the forward ($S_{rct,f}$) and backward ($S_{rct,b}$) direction.

2. the STS master equations describing the vibrational kinetics of the molecules accounting for the relevant energy exchange and reactive processes induced by collisions with electron and heavy-particles

$$\frac{dN_v}{dt} = \left(\frac{dN_v}{dt}\right)_{eV} + \left(\frac{dN_v}{dt}\right)_{VT} + \left(\frac{dN_v}{dt}\right)_{VV} + \left(\frac{dN_v}{dt}\right)_{VE} + \left(\frac{dN_v}{dt}\right)_{SE} + \left(\frac{dN_v}{dt}\right)_{React}$$

(26)

where N_v is the vibrational distribution in the vth vibrational level. On the right-hand side of Eq. (26), the contributions due to electron-vibration (eV), vibration-vibration (VV), vibration-to-translational (VT), vibrational-to-electronic (VE), spontaneous emission (SE) processes and to the relevant reactive channels, such as dissociation/recombination and ionization/recombination, are accounted for.

3. the STS master equations describing the electronic excited state kinetics of atoms and molecules

$$\frac{dN_i}{dt} = \left(\frac{dN_i}{dt}\right)_{eE} + \left(\frac{dN_i}{dt}\right)_{SE} + \left(\frac{dN_i}{dt}\right)_{Quench} \quad (27)$$

where N_i is the number density of the ith electronic excited state. The terms on the right-hand side of Eq. (27) correspond to excitation/de-excitation by electron impact (eE), spontaneous emission (SE) and quenching by heavy-particle (Quench) collisions.

4. the equation describing the plasma chemistry of the different species (neutral and ionized) in the reactive plasma, see Eq. (24).

The time dependent self-consistent kinetic approach consists in the simultaneous solution of Eq. (24) and Eq. (25)-(27), which are strongly coupled. The electron impact rate coefficients entering in Eq. (24), (26) and (27) are calculated by integrating the EEDF and the relevant electron impact cross sections on the electron energy axis. On the other hand, the collisional terms included in the electron Boltzmann equation (Eq. 25) are calculated by using the vibrational distribution functions, the electronic excited state population and the plasma composition calculated by Eq. (24), (26) and (27). The self-consistent approach has a long history in literature and was used to describe several plasma mixtures, such as H_2, H, N_2, O_2, N_2-O_2 in discharge and post-discharge, shock wave and expanding flow conditions [231, 275, 315–322]. Recently, the self-consistent model was applied to CO_2 plasmas by Pietanza et al. [269–274] to better understand the role of vibrational excitation in CO_2 conversion by cold non-equilibrium plasmas, giving particular attention to the electron kinetics and to the EEDF's calculation. The next subsections provide a general overview of their work.

5.2 Parametric results of the electron Boltzmann equation

As a first approach, Pietanza et al. [205, 265–267] performed a parametric solution of the electron Boltzmann equation in a pure CO_2 plasma to understand the dependence of the EEDF on the concentrations of CO_2 vibrational and electronic excited states. In these simulations, they considered as parameters the reduced electric field (E/N), the electron molar fraction (χ_e), the vibrational temperatures $T_{1,2}$ and T_3, describing, respectively, the symmetric/bending and the asymmetric CO_2 mode levels and the concentration of the metastable electronic excited state of CO_2 at 10.5 eV, i.e. $\chi_i(10.5 \text{ eV})$. The Hake and Phelps electron impact cross sections database [187] was used for CO_2, which is at the basis of a new more recent available database reported in section 3.2 [58, 88]. The EEDF shape was found to be strongly dependent on the vibrational temperatures and on the electronic excited state concentration, as it can be seen in Fig. 15 a and b, which report the EEDF calculated at (a) E/N=30 Td (discharge) and (b) E/N=0 Td (post-discharge), at different vibrational temperatures, with $\chi_i(10.5 \text{ eV})= 10^{-5}$ and $\chi_e = 10^{-3}$.

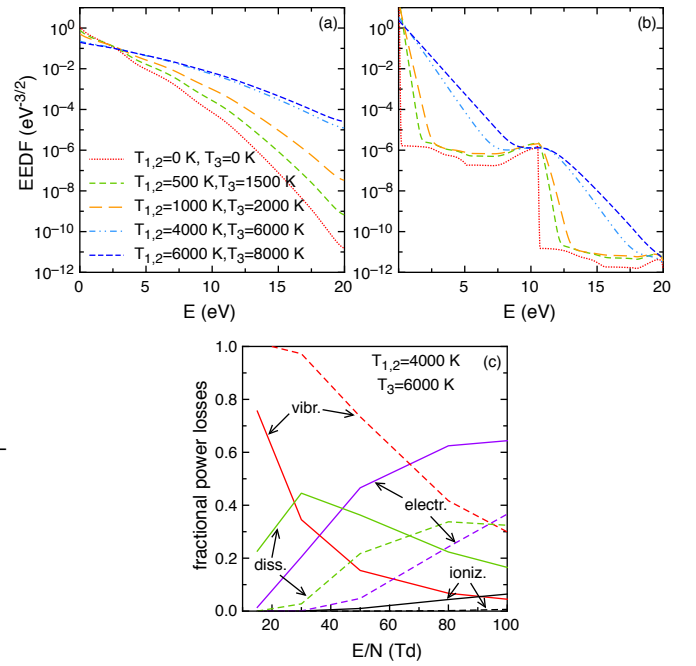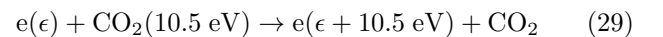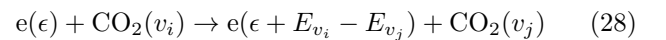**Fig. 15.** CO_2 EEDF calculated with the parametric solution of the electron Boltzmann equation in (a) discharge (E/N=30 Td) and (b) post-discharge (E/N=0 Td) conditions at different $T_{1,2}$ and T_3 temperatures [265]. (c) Fractional power losses as a function of E/N at $T_{1,2}$=4000 K and T_3=6000 K (full lines) and in the cold gas approximation ($T_{1,2}$=T_3=0 K) (dashed lines) [266].

Under discharge (see Fig. 15 a), the EEDF is enlarged by the increase of the vibrational temperatures, respect to the "cold" gas condition ($T_{1,2}$=T_3=0 K), due to the effect of superelastic vibrational and electronic collisions. As a matter of fact, by considering non-zero vibrational temperatures and a fixed concentration of the electronic excited state at 10.5 eV, the following superelastic vibrational and electronic processes start affecting the EEDF

$$\text{e}(\epsilon) + CO_2(v_i) \rightarrow \text{e}(\epsilon + E_{v_i} - E_{v_j}) + CO_2(v_j) \quad (28)$$

$$\text{e}(\epsilon) + CO_2(10.5 \text{ eV}) \rightarrow \text{e}(\epsilon + 10.5 \text{ eV}) + CO_2 \quad (29)$$

These processes create electrons at higher energies, near the threshold energies and their multiples, and the final effect is to push electrons towards higher energies respect to those characterizing the "cold" case. In the post-discharge (Fig. 15 b), a well-defined peak at 10.5 eV distinctively emerges due to the dominant effect of the superelastic electronic collisions involving the 10.5 eV state (see Eq. 29). The peak's height is proportional to the concentration of the 10.5 eV electronic state. The peak is also spread over $0< \epsilon <10.5$ eV through inelastic, elastic and electron-electron collisions, forming a long plateau especially at lower vibrational temperatures. The plateau disappears with the vibrational temperature increase, push-
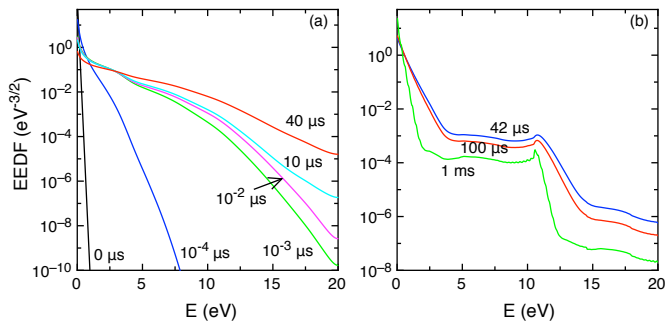
Fig. 16. Time dependent EEDF as a function of the electron energy (a) during the discharge and (b) in the post-discharge for a pure CO$_2$ plasma with T$_{gas}$=400 K, P=20 Torr, t$_{pulse}$=40 μs, E/N= 50 Td, $\chi_e(t = 0)$=10^{-6} [269].

Fig. 17. (a) VDF calculated at the end of the pulse (t$_{pulse}$=40 μs) at different T$_{gas}$ in the range 400-3000 K, at two different α values; (b) PVM and (c) DEM dissociation rate coefficients as a function of $1/T_{gas}$ with α=0.8 (full lines) and α=1 (dashed lines) for a pure CO$_2$ plasma (P=20 Torr, E/N= 50 Td,$\chi_e(t = 0)$=10^{-6}) [269].

ing the EEDF towards a Maxwell distribution. The enlargement of the EEDF due to superelastic vibrational and electronic collisions has a direct effect also on macroscopic quantities, such as electron impact rate coefficients and fractional power losses dissipated in the different CO$_2$ excitation channels by electron impact, making them dependent on the vibrational temperatures and on the concentration of electronic excited states [266]. Fig. 15 c shows the comparison of the fractional power losses (vibrational, dissociative, electronic and ionization) in a CO$_2$ plasma at high vibrational temperatures (T$_{1,2}$=4000 K and T$_3$=6000 K) (see dotted lines) with respect to the cold gas approximation (full lines) [6, 40, 254, 323]. Higher concentration of vibrational states, by enlarging the EEDF, modifies the fractional power losses in the direction of promoting higher threshold processes, i.e. dissociative, electronic excitation and ionization, hindering vibrational excitation.

5.3 Time dependent results: self-consistent model with STS kinetics for CO$_2$

As a further step, Capitelli et al. [321] performed a time dependent self-consistent solution of the electron Boltzmann equation with the STS vibrational and electronic kinetic equations of the CO$_2$ molecule by considering low CO$_2$ dissociation plasma conditions, i.e. short discharge electric field pulse (t$_{pulse} \sim 40\mu s$) and low concentration of dissociation products ($\chi_{CO}, \chi_O \leq 10^{-4}$). This choice was made to temporarily disregard the vibrational and electronic excited state kinetics of CO, O and C atoms in affecting the EEDF with their vibrational and electronic excited states. Fig. 16 shows an example of time dependent EEDF in a CO$_2$ plasma in (a) discharge and (b) post-discharge, calculated in the following conditions, T$_{gas}$=400 K, P=20 Torr, E/N= 50 Td, $\chi_e(t = 0) = 10^{-6}$.

As it can be seen, the EEDF increases during the discharge pulse gaining energy from the electric field and from CO$_2$ excited states through superelastic collisions. In the post-discharge, the plateau due to superelastic electronic collision of the 10.5 eV state is well evident, confirming the parametric results of Fig. 15 b.
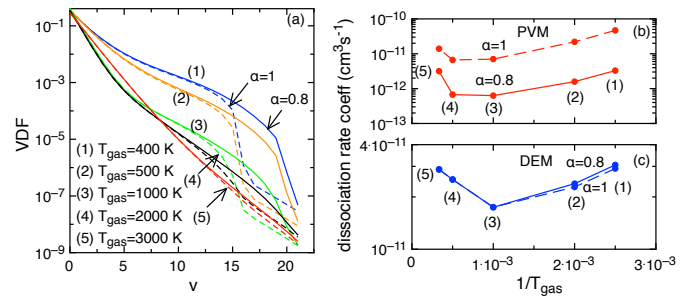
The corresponding CO$_2$ VDF for the asymmetric mode levels, calculated at the end of the discharge ($t = 40\mu s$) and for different T$_{gas}$ in the range 400-3000 K, is reported in Fig. 17 (a) at two different values of the α coefficient of the Fridman-Macheret model for CO$_2$ dissociation [40]. According to this model, the dissociation rate coefficient from higher vibrational levels k$_D$(v, T$_{gas}$) can be calculated from the ground state one k$_0$ (generally described by an Arrhenius rate coefficient) following

$$k_D(v, T_{gas}) = k_0 exp(-\frac{E_a - \alpha E_v}{KT_{gas}}) \qquad (30)$$

where E$_a$ is the activation energy and α a coefficient in the range $0 \leq \alpha \leq 1$. As it can be seen in Eq. (30), the vibrational energy lowers the activation energy barrier of the dissociation process with an efficiency described by the α coefficient: the closer to 1 the α value, the stronger the dissociation from higher vibrational levels. By looking to Fig. 17 a, the CO$_2$ VDF is characterized by an evident non-equilibrium plateau due to VV processes, depleted at higher v by dissociation and VT deactivation. The VV plateau is shorter for α =1 respect to α =0.8 due to a stronger dissociation from higher vibrational levels. This VV plateau is responsible of a very singular behavior of the dissociation rate coefficients as a function of the gas temperature, already shown also for cold molecular plasma involving diatomic molecules [251,324,325]. At lower gas temperature, i.e. when the VV plateau is more pronounced, the dissociation rate coefficients do not follow the classical Arrhenius trend but show a non-Arrhenius behavior as a function of the gas temperature, i.e. the rate increases with the decrease of the gas temperature. This can be observed by looking to Fig. 17 b and c, which show the calculated total rate coefficients ($cm^3 s^{-1}$) as a function of $1/T_{gas}$ for dissociation by vibrational excitation, also called Pure Vibrational Mechanism (PVM), and by Direct Electron impact Mechanism (DEM), described by the following processes CO$_2$(00v) + M $\rightarrow$ CO + O + M and e$^-$ + CO$_2$(00v) $\rightarrow$ e$^-$ + CO + O, respectively. These rate coefficients were calculated by summing, over the CO$_2$ asymmetric vibrational levels, the product

of the corresponding vibrational state resolved rate coefficient and the CO_2 VDF, see [269] for explicit expressions. The reason of this unexpected behavior is linked to the simultaneous and combined effect of VV and VT processes acting on the CO_2 VDF: as the gas temperature decreases, VV plateau are more pronounced and VT deactivation processes less efficient in deactivating the VDF tail, with the consequence that the corresponding CO_2 dissociation rates increases. At higher gas temperature, i.e. for $T_{gas} > 2000$ K, the CO_2 VDF is essentially thermal and the dissociation rate behavior starts again following the Arrhenius trend, i.e the rate increase with the increase of T_{gas}.

5.4 STS kinetics for CO molecules

To extend the CO_2 STS model to higher dissociation conditions, Pietanza et al. [270–272] developed an advanced STS vibrational and electronic excited state kinetics also for CO molecules, by considering 80 vibrational levels in the ground state $CO(X^1\Sigma^+)$ and several electronic excited states for CO, C and O. The STS CO kinetic model, solved self-consistently with the electron Boltzmann equation, was used to describe the behavior of a CO plasma mixture in MW discharges at intermediate pressure [270] and in Nano-Repetitively Pulsed (NRP) discharges with different interpulse delay times [271, 272]. In the latter case, a detailed analysis of the role of the CO electronic excited states in affecting the EEDF was performed by choosing optically thick and thin conditions and by taking into account important quenching processes involving the electronic excited states. Fig. 18 reports an example of CO VDF and EEDF calculated in a MW discharge in the following conditions, i.e. P=5 Torr, T_{gas}=500 K, t_{pulse}=2.5 ms, E/N=60 Td, $\chi_e(t=0) = 10^{-6}$.

The CO vibrational kinetics has strong similarities to CO_2 ones with the formation of VV plateau in the CO VDF, depleted at higher vibrational energy by VT deactivation and CO dissociation. Beside direct dissociation of CO into O and C atoms, also the Boudouard process, i.e. $CO(v)+CO(w) \rightarrow CO_2 + O$ (see also sections 2.2 and 3.1.4) was taken into account, by discussing its influence on the CO VDF as a function of the different estimations of its activation energy available in literature [119, 154, 270, 326]. Also the EEDF has a similar behavior as in the case of CO_2 (see Fig. 16), but with the appearance, in the post-discharge, of a more complex peak structure, due to the introduction of new electronic excited states of the CO, O and C systems. The peak structure is also complicated by the periodicity behavior of superelastic collisions with the energy of the electronic excited states, i.e. for the $CO(a^3\Pi)$ with energy $\Delta\epsilon$=6 eV, the peaks appear at ϵ=6 eV, 12 eV etc, but also by the superposition of more than one superelastic processes involving different electronic states [272]. The superelastic peak's height is proportional to the instant concentration of the electronic excited state related to it, and, as a consequence, the EEDF peak structure changes according to the radiative and quenching processes included in the
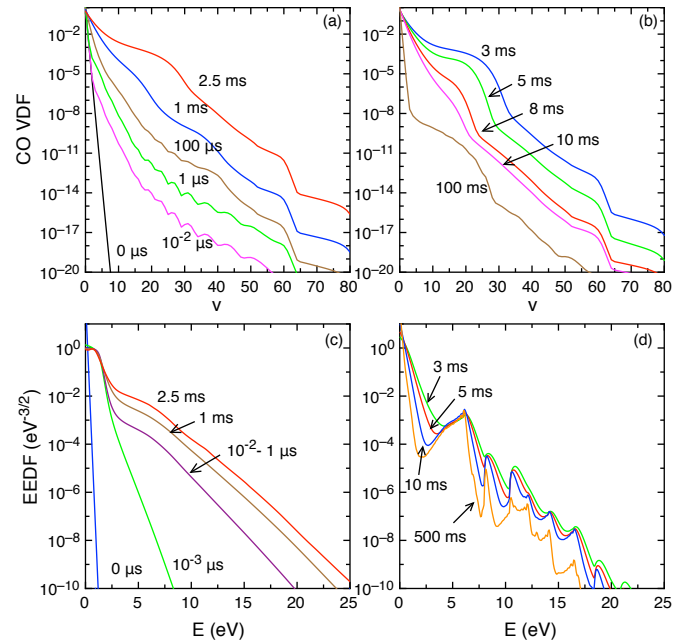

Fig. 18. CO VDF (a, b) and EEDF (c, d) time evolution in discharge (a, c) and post-discharge (b, d) conditions in a MW discharge of pure CO plasma [270].

electronic excited state kinetics. In particular, a different EEDF shape characterizes optically thick or thin plasma conditions, i.e. if radiation from allowed transitions involving the electronic excited states is completely absorbed by or emitted from the plasma, respectively. Among the different quenching processes involving CO, C and O electronic excited states, the most important one affecting the EEDF is the following

$$CO(a^3\Pi, v = 0) + CO \rightarrow CO(X^1\Sigma^+, v = 27) + CO \quad (31)$$
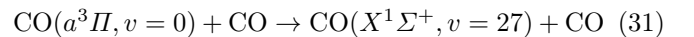
which involves the $a^3\Pi$ state at 6 eV and pumps vibrational quanta in the v=27 level (upper limit) of CO ground state. As an example, Fig. 19 shows the EEDF calculated for a pure CO plasma in a NRP discharge by considering optically thick and thin plasma and by including or not the quenching process in Eq. (31).

The NRP discharge considered is characterized by an interpulse delay time of 1 μs and the results at two different discharge pulses, the first and the sixth, are shown, at the end of the discharge (t=20 ns) (see Fig. 19 (a), (c)) and of the post-discharge (t=1 μs) (see Fig. 19 (b), (d)). In the optically thick case, the electronic excited state concentrations are higher with respect to the thin case, leading to higher peaks in the EEDF. In the thin case, instead, the EEDF loses all the peaks related to the emitting electronic excited states and by including the quenching process in Eq. (31), also the peak at 6 eV disappears with all the corresponding peaks at higher energies. For successive pulses (see the last pulse results in Fig. 19 (c), (d)), the EEDF behavior is similar to the first one, but, after the absorption of several discharge pulses and due
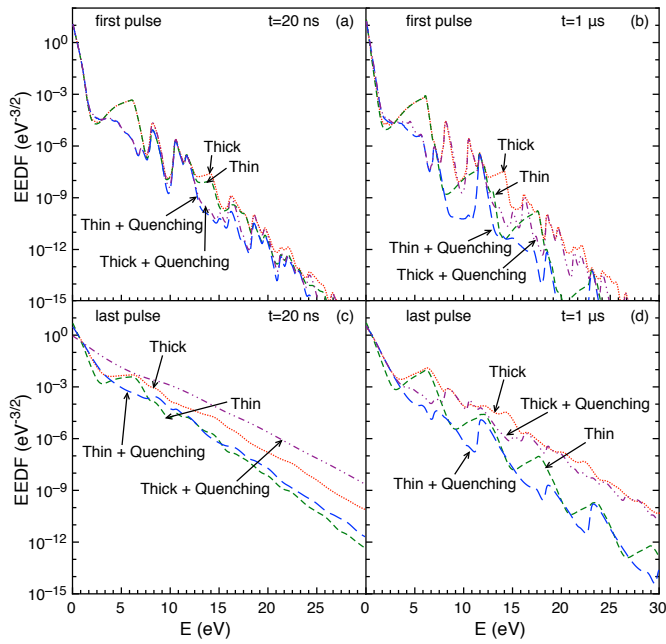
Fig. 19. EEDF calculated in the four kinetic model assumptions (optically thick, thin, thick + quenching, thin + quenching) at the end of the discharge (t=20 ns) and post-discharge (t=1 μs) of the first (n=1) and last (n=6) pulse of a NRP discharge for a pure CO plasma with an interpulse delay time of t_{id}=1 μs (P=760 Torr, T_{gas}=1000 K, E_{max}/N=160 Td) [272].

to the higher vibrational excitation and electron density reached, the EEDF is more enlarged by superelastic collisions and the peaks more smoothed by the stronger effect of e-e collisions.

5.5 Self-consistent model with STS kinetics for $CO_2/CO/O_2$

As a further improvement step, Pietanza et al. [273, 274] inserted the STS CO kinetics in the CO_2 kinetic model, together with a detailed STS kinetics also for O_2 (34 vibrational levels and 2 electronic levels). In this way, the resulting self-consistent model was able to describe in details the vibrational and the electronic excited state kinetics not only for the CO_2 system but also for all its main dissociation products, i.e. CO, O, O_2, C, studying the effect of the corresponding vibrational and electronic excited states on the EEDF. This self-consistent model was applied to MW discharges at intermediate pressure in the gas temperature range 300 K-2000 K in optically thin and thick conditions [273]. In the simulations, instead of E/N, constant power density P_d values were used, to investigate conditions closer to experimental ones, often characterized by well-defined values of this parameter. The calculated CO_2 conversion and energy efficiencies, as well as CO_2 VDFs, were shown to be in satisfactory agreement with the corresponding results predicted by the Antwerp group [256,297] in similar conditions. The following Fig. 20 and 21 show the simultaneous time evolution of CO_2, CO,
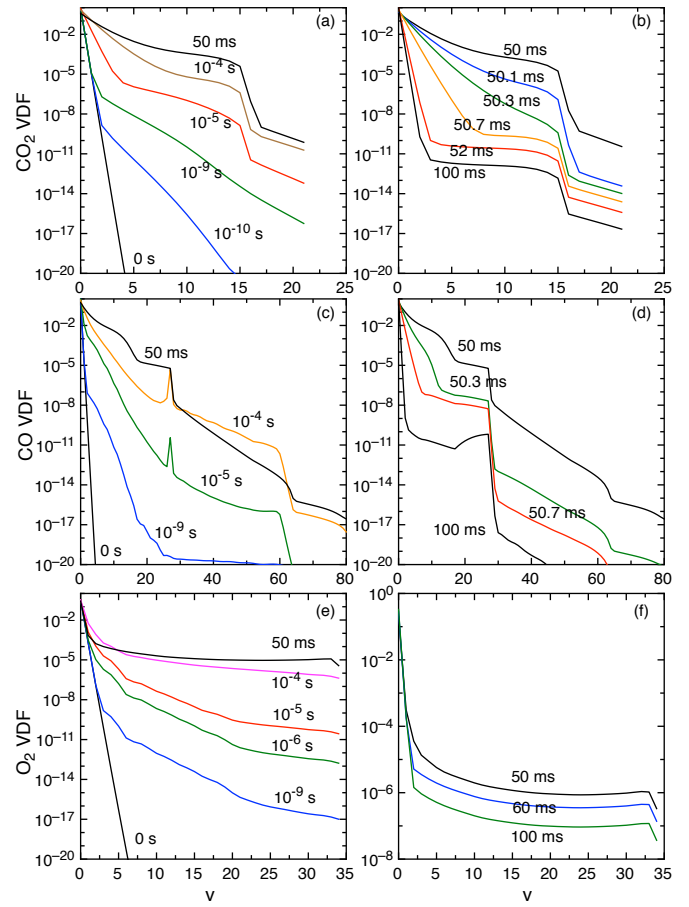

Fig. 20. CO_2, CO and O_2 VDF in discharge (a, c, e) and post-discharge (b, d, f) in the MW discharge characterized by T_{gas}=300 K, P=20 Torr, t_{pulse}=50 ms and P_d=80 W cm^{-3} [273].
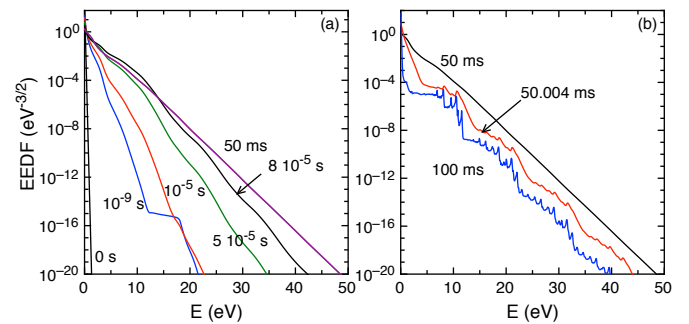

Fig. 21. EEDF time evolution in (a) discharge and (b) post-discharge [273].

O_2 VDF and EEDF in discharge and post-discharge conditions calculated by the self-consistent model of Pietanza et al. [273] in a MW discharge characterized by T_{gas}=300 K, P=20 Torr, t_{pulse}=50 ms and P_d=80 W cm^{-3} and by considering optically thick plasma conditions.

Transient and stationary VDFs have a non-equilibrium behavior both in discharge and post-discharge. They are the result of the simultaneous effect of eV, VV, VT and

dissociation and ionization processes. In particular, eV processes pump preferentially the lowest vibrational levels, while VV processes act essentially in the intermediate v range, creating the non-equilibrium plateau. VT processes deactivate preferentially the tail of the VDF as well as dissociation and ionization processes which occur mainly from the last vibrational levels. In the CO VDF, it is evident the effect of the quenching process of Eq. (31) which creates a peak at v=27, subsequently transformed in a little plateau by VV collisions. The O$_2$ system is characterized by low eV rates and strong VT O$_2$-O deactivation processes and, as a consequence, the corresponding O$_2$ VDF can be described by a Boltzmann distribution at the gas temperature at lower vibrational levels, with the superposition of a long non-equilibrium plateau at higher vibrational levels, created by the three-body recombination of O atoms, i.e. O+O+O → O$_2$(v)+O [275]. The EEDF is strongly affected by superelastic collisions, involving all the vibrational and electronic excited states of CO$_2$, CO, O$_2$, O and C species. To understand which is the main dissociation channel activated in the CO$_2$ plasma mixture in MW discharges at intermediate pressure, a direct comparison of CO$_2$ dissociation rates (cm^{-3} s^{-1}) by vibrational excitation (PVM: CO$_2$(00v) + M → CO + O + M; PVM$_O$: CO$_2$(00v) + O → CO + O$_2$) and by direct electron impact (DEM: e$^-$ + CO$_2$(00v) → e$^-$ + CO + O) were performed at different gas temperatures in the range 300 K-2000 K and with two electron impact CO$_2$ dissociation cross sections (Phelps, E$_{thr}$=7 eV, and Cosby, E$_{trh}$=11.6 eV) (see Fig. 22) [273]. At low gas temperature, i.e. 300 K, the CO$_2$ dissociation occurs preferentially by vibrational excitation and the dissociation rates are very little dependent on the choice of the electron impact cross section (see Fig. 22 (a) and (c)), with the only exception of DEM rates, which increase if the Phelps cross section is considered instead of the Cosby's one. At higher gas temperature, instead, i.e. at 2000 K, the PVM and DEM mechanisms become competitive and the global behavior is strongly depending on the choice of the cross section (see Fig. 22 (b) and (d)). With the Cosby cross section (high threshold), the increase of T$_{gas}$ leads to an increase of DEM rates, which is however not sufficient to overcome the prevailing PVM rates, whose rates decrease with T$_{gas}$ in this gas temperature range due the non-Arrhenius behavior, already shown in Fig. 17 b). As a consequence, the global effect is a decrease of CO$_2$ conversion with the increase of T$_{gas}$ if the Cosby cross section is used. With the Phelps cross section, instead, with the increase of T$_{gas}$, the overall kinetics passes to a regime in which the DEM mechanism starts prevailing, with a more thermal behavior of the discharge, and the CO$_2$ conversion rates globally increases with T$_{gas}$.

Higher gas temperature MW discharges, with T$_{gas}$ in the range 3500-5500 K, were also investigated by Pietanza et al. [274] to compare the self-consistent model results to recent experiments performed by Groen et al. [327] in diffuse and contracted regimes. The kinetic values for the electron density, reduced electric field and electron
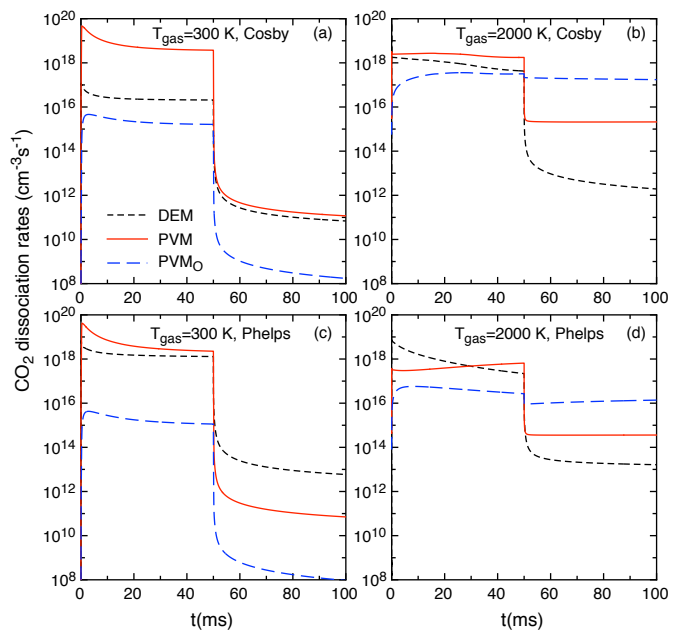

Fig. 22. CO$_2$ dissociation rates in a MW plasma discharge (P=20 Torr, P$_d$=80 Wcm^{-3}, t$_{pulse}$=50 ms, T$_{gas}$ in the range 300 K-2000 K and with different electron impact cross sections, i.e. Cosby and Phelps) [273].

temperature calculated by the self-consistent model were compared to the same quantities measured and/or estimated by Groen et al., finding a good qualitative agreement. Moreover, deviations from thermal distribution for the VDFs and EEDF and from thermal composition were still present even at these high translational temperatures as already pointed out in section 4.3.

6 Step by step validation in low excitation regime

6.1 Preliminary considerations

In an active plasma, many different phenomena are simultaneously at play and a strong coupling of the different kinetics happens as discussed in sections 4 and 5. Therefore, it is usually very difficult to unambiguously identify the dominant mechanisms, the role of the individual processes, and their contribution to specific plasma properties. Modelling and simulation are powerful tools to interpret and predict the behaviour of complex molecular plasmas. However, their reliability critically depends on a correct identification of the energy transfer pathways, electron impact mechanisms, heavy-particle chemical reactions, and the corresponding cross sections and/or rate coefficients. To circumvent these difficulties, a step-by-step model validation strategy has been pursued over the last few years in a joint international effort, with dedicated experiments performed at the Laboratoire de Physique des Plasmas, Ecole Polytechnique, France, and at the Technische Universiteit Eindhoven, The Netherlands, and modelling and

simulations developed at the Portuguese group N-Plasmas Reactive: modeling and Engineering (N-PRiME) from Instituto Superior Técnico, Universidade de Lisboa. The experiments are designed in such a way as to evince particular aspects of the complex coupled kinetics, in conditions where other effects are not present or have negligible contributions. In this way it is possible to isolate, understand and validate partial aspects of the plasma behaviour, progressively building the different modules that will ultimately lead to a *reaction mechanism* - defined here as a set of reactions and rate coefficients, validated against benchmark experiments - for CO_2 plasmas.

The experimental work leverages on the studies carried out by Klarenaar *et al* [201], in which the time-dependent population of various individual CO_2 vibrational levels in a pulsed DC glow discharge were measured through time-resolved *in situ* Fourier transform infrared (FTIR) spectroscopy. Throughout these studies special attention was given to "single-pulse" measurements, where the residence time of the gas in the plasma reactor is well below the pulse off time, purging the plasma reactor of most CO and O_2 before the next discharge [201]. These data provided the initial framework for model validation through the envisaged step-by-step strategy, starting with a low-excitation regime in which only the lowest vibrational levels are populated and the role of dissociation products is vanishingly small. Under this approach it was possible to: (i) study the time-resolved evolution of the lower vibrationally excited CO_2 levels during the afterglow of CO_2 discharges, validating the vibrational kinetics involving the lower ~ 70 states and the corresponding rate coefficients for vibration-to-vibration (V-V) and vibration-to-translation (V-T) energy exchanges [61]; (ii) investigate the effect of electrons on the distribution of the lower vibrationally excited CO_2 levels in pulsed and continuous glow discharges, validating the electron impact processes of excitation and de-excitation of vibrational levels (e-V) [62]; (iii) investigate the influence of N_2 on the CO_2 vibrational distribution function and dissociation yield in pulsed glow discharges [94]; (iv) validate of the electron-impact dissociation cross sections of CO_2 [89]; (v) study the gas heating in the afterglow of pulsed CO_2 glow discharges, further validating the V-V and V-T mechanisms and rate coefficients [63]; and (vi) propose a reaction mechanism to predict the formation of dissociation products in CO_2 discharges in conditions where the vibrational kinetics can modify the EEDF but has no direct influence on chemical reactions [148].

The remainder of this section overviews some of the investigation dedicated to the study of CO_2 plasma kinetics under a low-excitation regime. Subsection 6.2 presents the general modelling framework and discusses the theoretical formulation and related system of equations used to model the different kinetics inherent to CO_2 plasmas. Subsection 6.3 examines isolated aspects of the complex kinetics of CO_2 plasmas, based on the comparisons of the results obtained from the model with the experimentally measured data.

6.2 Modelling framework

It is important to highlight some basic concepts and approximations associated with the CO_2 kinetics considered in the description of the vibrational kinetics in [61–63, 89, 94, 201]. CO_2 is a linear triatomic molecule with three fundamental modes of vibration: the symmetric stretching mode, the doubly degenerate bending mode and the asymmetric stretching mode. These modes are characterized by the quantum numbers v_1, v_2, v_3 and l_2, with the rule $l_2 = v_2, v_2-2,...,1$ or 0 depending on whether v_2 is odd or even. In order to characterize a CO_2 vibrational level one can use the notation $CO_2(v_1 v_2^{l_2} v_3)$. Furthermore, as it is often mentioned in literature [328], due to an accidental degeneracy between the v_1 and $2v_2$ modes in CO_2 there is a mixing of vibrational levels with the same type of symmetry (the same l_2 number) which increases the energy difference between them, *i.e.*, one level is shifted up in energy and the other is shifted down, so that the separation of the two levels is larger than expected (Fermi resonance). The new "mixed" energy levels loose their meaning of bending and symmetric stretching states, being often presented by placing both sets of symbols within parenthesis with a ranking number. For example, the states $(02^00,10^00)_I$ and $(02^00,10^00)_{II}$ represent the Q-branches in CO_2 at 1285 cm^{-1} and 1388 cm^{-1} above the ground state. Following the description of Blauer and Nickerson [328], it is assumed that the states in Fermi resonance are strongly coupled and the Fermi states are replaced by an average effective state [61,201]. Any attempt to consider the states in Fermi resonance individually goes beyond the scope of the studies in [61–63, 89, 94, 201]. Under this framework, and considering a low excitation regime, it is also assumed that the system is well described by $v_2^{max} = v_3^{max} = 5$, where v_2^{max} and v_3^{max} correspond to the maximum values for the bending and asymmetric quantum numbers, respectively and $v_1^{max} = 2$ corresponds to the maximum value for the symmetric stretching quantum numbers [61,62]. This leads to a total of about 70 CO_2 vibrational levels.

In order to describe the time-evolution of the vibrationally excited states considered, a set of time-dependent rate balance equations involving different creation and loss molecular mechanisms is considered, as already introduced in section 5 (see Eq. (26)) but with the following terms

$$\frac{dN_v}{dt} = \left(\frac{dN_v}{dt}\right)_{eV} + \left(\frac{dN_v}{dt}\right)_{VT} + \left(\frac{dN_v}{dt}\right)_{VV} + \left(\frac{dN_v}{dt}\right)_{Wall}. \quad (32)$$

where $v \equiv v_1 v_2^{l_2} v_3$ denotes a generic CO_2 vibrational level. The first term includes all the creation and loss mechanisms leading to vibrationally excited states as a result of electron impact collisions. In [61–63, 94, 148], for the calculation of the electron impact reaction rate coefficients, the EEDF is self-consistently calculated by solving the steady-state, homogeneous electron Boltzmann equation in the two-term expansion approximation using the LisbOn KInetics (LOKI) Bolzmann solver [210], while taking into account the various elastic and inelastic colli-

sions between electrons and vibrationally excited CO$_2$ [88] and CO [209] molecules. As carefully described in [62] and briefly reviewed in section 3.2, the eV cross sections for CO$_2$ are obtained from a direct deconvolution of the available lumped cross sections according to the statistical weights of the various levels, and the missing cross sections are generated using Fridman's approximation [40].

The second and third terms represent the vibrational exchanges due to VT and VV collisions, respectively. Most of the reaction rates for these mechanisms are compiled based on scaling laws adapted from the SSH theory [48, 329] as done, *e.g.*, in [118], and on the data survey of Blauer and Nickerson [328], which combines experimental results and theoretical studies to obtain the most important deactivation channels. In addition, for the quasi-resonant vibrational exchanges involving the asymmetric mode of vibration the rate coefficients are obtained from the theory of long-range forces of Sharma and Brau [330] and the experimental work of Kreutz et al [331]. In such cases, it is assumed that the rate coefficients decrease with the gas temperature, which should be valid for the region of low gas temperatures (below ~ 1000 K) [61].

Finally, the last term represents the deactivation of vibrationally excited states at the reactor walls. Here, it is considered that when a vibrationally excited molecule hits the reactor surface, it has a probability γ_v of losing its vibrational energy to the ground state, so that the loss frequency, ν_{wall}, in a cylindrical discharge of radius R, becomes

$$\nu_{wall} = \left(\frac{1}{D} \left(\frac{R}{2.405} \right)^2 + \frac{2R(1 - \gamma_v/2)}{\gamma_v \langle v \rangle} \right), \qquad (33)$$

where D is the diffusion coefficient (calculated according to Hirschfelder [332]), $\langle v \rangle$ is the thermal speed [94]. It is further assumed that $\gamma_v = 0.2$ for a Pyrex surface in all the CO$_2$ vibrational levels, based on the deactivation probabilities found in literature for the bending and asymmetric levels in the range of $\sim 0.18 - 0.4$ [333]. Despite the lack of data for the symmetric mode of vibration, it seems reasonable to assume that the deactivation probability is in the same order of magnitude.

6.3 Step-by-step model validation

This section presents and analyzes different isolated aspects of CO$_2$ plasma kinetics, comparing the results of the simulations with the experimental measurements.

6.3.1 Vibrational kinetics

The first step undertaken towards the establishment of a reaction mechanism for CO$_2$ plasma kinetics was based on the study of the discharge afterglow under the single pulse measurements of [201], where it is possible to neglect electron impact collisions, i.e. first term in Eq. (32). As an illustration of the comparison between the modelling results and the experimental data, Fig. 23 shows the

normalized density of the first few vibrationally excited levels associated to the symmetric and bending modes of vibration during the afterglow of the pulsed DC glow discharge operating at p = 5 Torr, I = 50 mA, for a pulse of 5 ms and 150 ms off time. More specifically, Fig. 23(a) shows the first three non-Fermi (i.e. states with $v_2 = l_2$) bending states, while Fig. 23(b) contains the first two coupled Fermi levels. For these levels we observe an excellent agreement between the calculated and experimentally determined populations, which validates the set of rate coefficients under the studied conditions. As observed by Klarenaar et al. [201], the results indicate a fast decay and relaxation (within the ms scale) of the vibrationally excited states as they quicky thermalize after the plasma-off. Note that in these simulations the gas temperature is used as an input data and is taken from experiment. Relative to the evolution of the asymmetric mode of vibration, it is interesting to note a small disagreement between the experimental data and modelling results at the end of the afterglow. This is shown in Fig. 24 through the evolution of the first vibrationally excited asymmetric state which deviates from the experimental data for afterglow times larger than about 2 ms after the plasma is turned off. Several reasons can explain this disagreement and they are mostly likely related to an omission of some creation/loss term in Eq. (32) (e.g. spontaneous emission) or an underestimation of the VT relaxation processes of the type

$$CO_2(00^01) + M \rightarrow CO_2(mn^lp) + M \qquad (34)$$
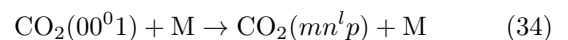
Deactivation channels for processes in Eq. (34) are taken into account according to the data survey of Blauer [328] which relates the most important relaxation products from theory with experimental data (see references within [328]). The rather wide spread of experimental results may introduce a certain error in the calculated density of the state CO$_2(00^01)$ and compromise the capability to reproduce the correct relaxation in the afterglow. In addition to the previous point, another source of error relative to the calculation of the CO$_2(00^01)$ state density can come from the reaction rate coefficients used to describe quasi-resonant VV exchanges, considered only to be due to long-range forces. Considering the rather large range of gas temperatures presented in these time-resolved experiments (300-1200 K [201]) better rate coefficients for VV exchanges are required in order to take into account both short- and long-range contributions.

After validation of the vibrational kinetics involving heavy-particle processes [61], electron impact collisions were taken into account to analyze the active part of a pulsed DC glow discharge [62]. Fig. 25 shows the evolution of the first vibrationally excited level associated with the bending mode of vibration. The electron density profile required for the first term in Eq. (32) was estimated based on the discharge current and the CO$_2$ ionization coefficient [62], while the self-consistent reduced electric field is determined from the electron and ion rate balance equations, using the requirement that under steady-state conditions the total rate of ionization must compensate the
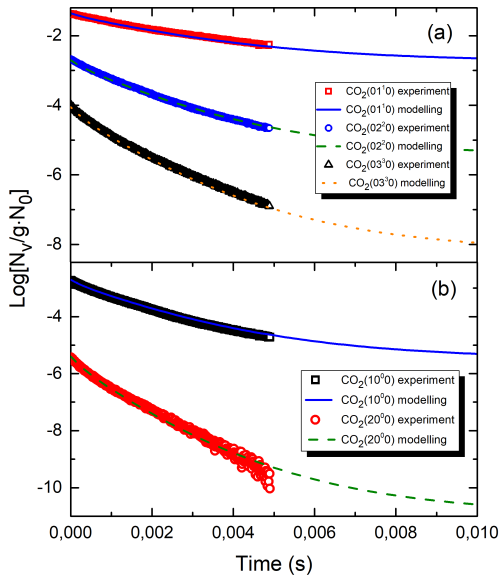
Fig. 23. Normalized state densities during the afterglow of a pulsed DC glow discharge at $p = 5$ Torr, $I = 50$ mA and $\Delta t = 5$ ms for (a) first CO$_2$ vibrational levels associated to the bending mode (non-Fermi states) and (b) first vibrational levels associated to the coupled Fermi levels. N_0 and g are the ground state density and statistical weight respectively.
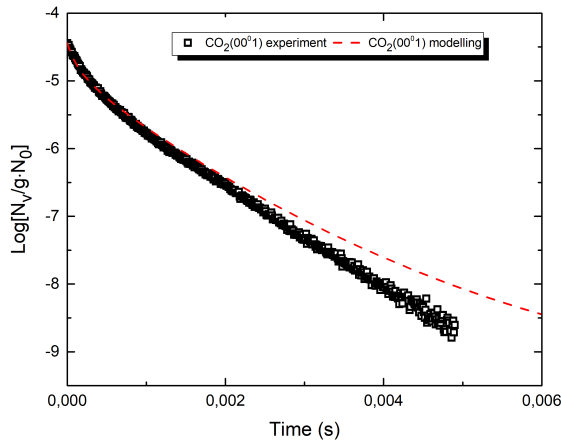

Fig. 24. Normalized density associated to the first vibrationally excited level of the asymmetric mode of CO$_2$ during the afterglow of a pulsed DC glow discharge (same conditions as presented in figure 1).

rate of electron loss by ambipolar diffusion to the wall. For the conditions of Fig. 25, the calculated reduced electric field is about 55 Td. The simulation results are in generally good agreement with the experimental data, albeit predicting a slightly slower growth of the bending populations as compared with the experiment. Possible explanations may involve more complex deconvolution procedures of the lumped cross sections and/or an influence of vibrational transfers from the asymmetric mode in colli-
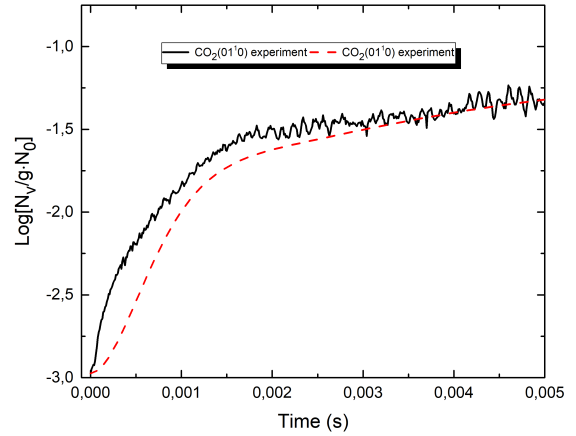

Fig. 25. Normalized density associated to the first vibrationally excited level of the bending mode of CO$_2$ during the active part of a pulsed DC glow discharge (same conditions as presented in figure 1)

sions involving oxygen molecules or excited atoms. Preliminary results point towards a higher likelihood of the latter mechanisms, but at present it is premature to draw definitive conclusions. Regarding the time evolution of the normalized density of the first asymmetric mode level in the active part of the discharge, the modeling and the experimental results are in good agreement, with only a slightly slower growth of the calculated density as compared with the experimental data, as already observed for the afterglow results of Fig. 24 [62].

6.3.2 Gas heating

An extra validation of the reaction mechanism for VT and VV processes established under the previous studies was made through the investigation of the time-dependent evolution of the energy transfer into gas heating in the afterglow of pulsed CO$_2$ glow discharges [63]. Considering a gas discharge under isobaric conditions and assuming that the heat conduction is the dominant cooling mechanism, the temporal evolution of the radially averaged gas temperature, T_g, was studied according to

$$n_m c_p \frac{\partial T_g}{\partial t} = Q_{in} - \frac{8\lambda_g(T_g - T_w)}{R^2}, \qquad (35)$$

where n_m is the molar density, c_p is the molar heat capacity at constant pressure, Q_{in} is the mean input power transfer to the translational model, λ_g is the thermal conductivity and T_w is the temperature at the discharge wall. The model describes very well the gas heating along the afterglow of discharges operated in pure CO$_2$ with negligible dissociation [63]. This work confirmed that the relaxation of the first vibrationally excited CO$_2$ levels is mostly governed by the creation and loss mechanisms considered in Eq. (32), with the deactivation at the wall having a major contribution to gas heating at low pressures (below ~ 1 Torr).

6.3.3 Electron impact dissociation

Under the framework developed in the previous sections it was possible to explore other aspects of the CO_2 kinetics. In particular, an investigation of electron impact dissociation and an assessment of the different CO_2 electron impact dissociation cross sections available in the literature was performed [89]. To carried out this investigation, a careful experimental approach was designed to evince CO_2 electron impact dissociation while avoiding any influence from other dissociation mechanisms or chemical reactions. On the other hand, a small set of chemical reactions included involving CO and Oxygen formation was added to the model and different electron impact dissociation cross sections were tested and evaluated [88,89]. The modelling and experimental results agree remarkably well when the theoretical calculations from Polak and Slovetsky [206] for the CO_2 dissociation cross sections are used. Therefore, the results establish the validity of the dissociation rate coefficients derived from these cross sections in the range of reduced electric fields between 45 and 105 Td. Moreover, this validation suggests that the energy loss cross sections proposed by Phelps [75, 187], which are widely used in the literature as representative of dissociation, probably include energy loss processes besides dissociation, an hypothesis already advanced in [88].

As noted in section 3.2, a recent analysis relying on estimations made using an analytical model for streamer discharges [207] suggests that, for high values of E/N (above 100 Td and up to 600 Td), the dissociation rate coefficients calculated from the cross sections in [206] can be underestimated. This would mean that the high-energy part of the cross sections from [206] or the higher energy threshold dissociation cross section from [206] (see section 3.2) would be accordingly underestimated.

6.3.4 Reaction mechanism for vibrationally-cold CO_2 plasmas

Another step towards a more complete and thorough validation of CO_2 decomposition in a plasma environment driven by electron-impact processes was given recently by A.F. Silva *et al* [148]. The CO_2 model is extended in order to couple self-consistently the electron Boltzmann equation with a system of rate balance equations describing the creation and destruction of the most important charged and neutral heavy species. The simulations are validated against measurements taken in continuous CO_2 DC glow discharges in a relatively large range of experimental conditions: pressures from 0.4 to 5 Torr, discharge currents from 10 to 50 mA and gas flowing at 2 to 8 sccm. The corresponding reduced electric fields range from 50 to 100 Td. The model includes a comprehensive list of reactions, electron impact cross sections and heavy-particle rate coefficients, validated from the comparison with experimental data on the product formation, namely the densities of ground-state atomic oxygen $O(^3P)$ and carbon monoxide $CO(X\ ^1\Sigma^+)$ molecules, as well as on the

reduced electric field and discharge power. A state-to-state vibrational kinetics is not included, since in these conditions vibrationally-driven chemistry and dissociation is not significant. Nevertheless, vibrational distributions are accounted for in the calculation of the EEDF, using the experimental values of the corresponding vibrational temperatures, as collisions with vibrationally excited CO_2 and CO molecules can modify the shape of the EEDF [209, 269, 270]. Important modifications in the EEDF are also brought by the changes in the mixture composition due to dissociation, as electrons start channeling their energy to the excitation of CO and, to a lesser extent, O_2 and O [148]. Following the experimental evidence of an important role of the electronically excited state $CO(a\ ^3\Pi_r)$ in the decomposition of CO_2 [131], its kinetics is included and carefully discussed in the model. The addition of the state-to-state CO_2 vibrational kinetics within low-excitation conditions, i.e., accounting for the same ~ 70 individual vibrational levels and corresponding reactions and rate coefficients as in [61,62], was achieved very recently [39].

The validation of the vibrational kinetics of CO_2 and CO in a plasma by comparing model and experiment is for the moment still limited to the low excitation regime. On the one hand, the available spectroscopic data do not easily allow to treat very strongly excited CO_2 spectra. On the other hand, models describing the full state-to-state vibrational levels by coupling electronic, vibrational and chemical kinetics in a self-consistent way would still suffer from too much uncertainty on many elementary process parameters. It is however possible to have a description of all the vibrational levels with full STS models when electron impact processes can be ignored. This is relevant to study heat shields for atmospheric entry plasma as described in the following section.

7 Vibrational kinetics in hypersonic entry problems

7.1 General considerations

Interest to high-temperature carbon dioxide kinetics is tightly connected to Mars exploration programs, such as Mars Pathfinder, Mars Sample Return Orbiter, Mars Space Laboratory, Exomars [334–336]. In hypersonic applications, vibrational kinetics is strongly coupled with chemical reactions, and such coupling may considerably affect the flow parameters and surface heating. Additional difficulties in modeling hypersonic entry arise due to the necessity of including the transport terms to the fluid-dynamic equations; this is particularly challenging for the STS approach. Models can be validated using experimentally measured surface heat fluxes [337–339]; however, reliable experimental data on CO_2 flows under Mars entry conditions are scarce. In the absence of experimental studies, detailed STS simulations of CO_2 kinetics, dynamics and heat transfer may be considered as benchmark solutions for the assessment of numerically efficient reduced-order approaches, as is shown in [340,341].

During the last decade, many studies of high temperature non-equilibrium CO_2 flows have been carried out using several approaches of various complexity: multi-temperature [47, 342–346], STS [46, 276–279] and reduced order coarse-graining techniques [347–349]. Different effects are discussed such as the influence of the flow conditions, thermo-chemical model, models for transport properties and radiation. In the present section, we discuss some recent results obtained by Armenise and Kustova in the frame of the STS simulations of a 1D CO_2 flow along the stagnation line with the emphasis on the coupled vibrational-chemical kinetics and heat flux. This STS simulations in Mars entry conditions have, as input data, a full set of VV and VT CO_2-CO_2 and CO_2-CO collision rates involving a more complete CO_2 vibrational energy level scheme. This full set can be, in principle, exploited also in STS models describing CO_2 dissociation in plasma discharges, even if linking of the numerous vibrational states becomes prohibitively expensive when electrons enter in the system. The hypersonic entry scenario case can provide also knowledge for better description of CO_2 recombination in plasmas. As a matter of fact, the boundary layer conditions are very similar to post-discharge as in supersonic expansion microwave [299, 350]. In the shock layer of atmospheric entry body, there is a high temperature plasma, cooling while diffusing towards the low temperature surface [351, 352]. An interesting application of the present section can be also to explore the possibility to create O_2 on the Mars soil from CO_2 taken from Mars atmosphere and transforming the CO_2 in CO and O_2 by using plasma discharges [2, 37–39].

7.2 Full STS model

Under high-temperature conditions, reduced STS models [40, 254] taking into account all levels of the asymmetric mode and just a few lowest states of symmetric and bending modes, as those presented in sections 4, 5 and 6, are not applicable since they may cause considerable errors in thermodynamic functions (in particular, the specific vibrational energy). Armenise and Kustova's full STS model takes into account CO_2 vibrational states given by all possible combinations of the quantum numbers of symmetric, bending and asymmetric modes. Only the bound states located below the dissociation energy, $E_D = 5.517$ eV, are taken into account, and for anharmonic oscillators, the number of states is about nine thousands [46]. Since computational resources used in [46] were not capable to solve nine thousands differential equations describing the viscous flow in the STS approach, the model was limited by the threshold of 3 eV, thus taking into account only 1224 vibrational states. This approximation is justified by the strong interaction among the normal modes for the high vibrational states of CO_2, i.e. at vibrational energies above 2 eV; this strong interaction causes the modes are no more well defined as at low vibrational energies but they turn into quasicontinuum of states [279]. Along with CO_2 molecules, the model includes species which appear due to carbon dioxide decomposition: CO,

O_2, O, C. Implementation of the full vibrational ladder allows to account for intramode VV_3, VT_1, VT_2 and VT_3 exchanges, intermode VV_{1-2}, VV_{2-3} and VV_{1-2-3} transitions, vibrational energy transitions between different molecules VV_{3-CO}, VV_{2-CO} and VV_{1-2-CO}, as well as state-specific dissociation-recombination reactions and exchange reactions, i.e. $CO_2(v_1,v_2,v_3)+O \rightleftharpoons CO(w)+O_2(v)$, where v_1, v_2, v_3 are the quantum numbers of symmetric, bending and asymmetric modes, correspondingly. Such a kinetic scheme is described in details in [277–279].

To proceed with simulations, state-resolved rate coefficients of vibrational energy transitions and chemical reactions are needed. Experimental data are available for the selected transitions between the lowest states [353–356]; these data are often interpolated for the higher states using the formulas of the SSH theory [48], see [46, 250]. However, the range of validity of experimental measurements is limited by low temperatures. One has to mention a few works on the quasi-classical trajectory calculations of the rate coefficients in CO_2 [54, 55, 357]; unfortunately, the results are obtained only for several transitions and thus cannot be used in full STS simulations. Theoretical approaches include the first-order perturbation SSH theory [48] and the forced harmonic oscillator (FHO) model [49,50,170], which recently was extended for three-atomic gases [52,53]. The results discussed hereafter are obtained using the SSH model [48] which provides the complete set of rate coefficients for vibrational transitions.

State-resolved exchange reaction rate coefficients are calculated using the theoretical model proposed in [279]; the model takes into account vibrational excitation of both the reagents and products. The state-resolved dissociation rate coefficients are calculated by means of the generalized Marrone-Treanor model [250, 278]. The thermal equilibrium reaction rate coefficients are given by the Arrhenius law with parameters suggested by McKenzie [358] and Park [342].

7.3 Transport properties

One of the most challenging tasks is implementation of the state-resolved transport coefficients. In the STS approach, the total heat flux $\mathbf{q}$ includes several contributions responsible for various dissipative processes [359, 360]:

$$\mathbf{q} = \mathbf{q}_F + \mathbf{q}_{MD} + \mathbf{q}_{TD} + \mathbf{q}_{DVE}, \qquad (36)$$

where $\mathbf{q}_F$, $\mathbf{q}_{MD}$, $\mathbf{q}_{TD}$, $\mathbf{q}_{DVE}$ are the terms connected to thermal conduction (Fourier flux), mass diffusion, thermal diffusion and diffusion of vibrational energy carried by excited molecules, respectively. For CO_2 flows, these contributions are written explicitly in [46, 276]. They depend on the gradients of temperature, species mass fractions, vibrational level populations, and state-resolved transport coefficients: thermal conductivity, viscosity, multi-component diffusion coefficients for each pair of vibrational states, and thermal diffusion coefficients. The general kinetic-theory algorithm for the calculation of state-specific transport coefficients is developed in [361, 362] (for some

peculiarities of CO_2 transport properties, see also [250, 363, 364]). It requires numerical solution of the transport linear systems and expresses the transport coefficients as functions of collision integrals, temperature, molar fractions of all vibrational states and atomic species. Keeping in mind that the transport systems are of the order of N (N is the number of vibrational states in a mixture), and the number of diffusion coefficients is about N^2, direct implementation of this transport model to the fluid-dynamic solver is not feasible at present time.

To overcome the problem, Armenise and Kustova propose using a post-processing technique introduced in [365, 366] to evaluate the heat flux. The problem is split into several stages. First, in order to study the flow-field and VDF, the fluid-dynamic equations with simplified transport terms depending on the constant Prandtl and Schmidt numbers are solved. Once the solution is obtained, the state-resolved transport coefficients are calculated as functions of temperature, mixture composition and VDFs. Gradients of fluid-dynamic variables obtained at the first step are then used in order to calculate the heat flux.

7.4 Stagnation line flow

Armenise and Kustova simulate the flow along the stagnation line in the boundary layer of a hypersonic vehicle on the basis of the simplified system of 1D boundary layer equations, written in self-similar variables (ξ, η):

$$\frac{\partial^2 c_v}{\partial \eta^2} + f\text{Sc}\frac{\partial c_v}{\partial \eta} = S_v, \qquad v = 1, ..., N \qquad (37)$$

$$\frac{\partial^2 \theta}{\partial \eta^2} + f\text{Pr}\frac{\partial \theta}{\partial \eta} = S_T. \qquad (38)$$

η is the coordinate normal to the surface, i.e. the one along the stagnation line, f is the stream function. Eqs. (37) are the continuity equations for different species mass fractions c_v, whereas Eq. (38) is the energy equation for the dimensionless temperature θ. Different species in the considered $CO_2/O_2/CO/O/C$ mixture are the vibrational states of CO_2, O_2 and CO molecules, and atoms O and C. Sc and Pr are the Schmidt and Prandtl numbers. On the right hand side, S_v and S_T are the source terms in which the STS chemical kinetics is included. The details can be found in [46].

The boundary conditions needed to solve Eqs (37)–(38) are the boundary layer edge pressure p_e, temperature T_e, the equilibrium distributions at the boundary layer edge; the surface temperature T_w, the parameter β has the meaning of the residence time of a fluid element in a particular point of the boundary layer. Moreover, the surface is assumed non-catalytic, that means zero gradients of each species mass fraction on the surface.

The results reported below are obtained for the test case corresponding to experiments in the Hypulse facility [337]. The following boundary conditions and mixture composition are fixed: $T_w = 700$ K, $T_e = 4555$ K, $p_e = 952$ Torr, $\beta = 1.283 \cdot 10^5$ s^{-1}, 35.32% of CO_2, 41.2% of CO, 6.42% of O_2, 17.06% of O, and 4.25×10^{-5}% of C.

7.5 Results on STS simulations of hypersonic Mars entry

Let us start with the comparison of the VDF obtained by Armenise and Kustova for different chemical models and kinetic schemes. For this purpose, the above test case with the full kinetic scheme including all processes (vibrational transitions, dissociation-recombination, and exchange reactions) and with the reduced scheme including only dissociation and recombination (Diss./Rec.) is considered. Two sets of parameters in the Arrhenius law are used, those of McKenzie [358] and Park [342]. Fig. 26 shows, as a function of the CO_2 vibrational energy, the boundary layer edge equilibrium CO_2 vibrational distributions (in green), as well as the CO_2 VDF on the surface obtained when only the dissociation-recombination reactions (in blue) and all the processes (in red) are included in the solution of the boundary layer system (Eq. (37)–(38)). The top plot is for the McKenzie model, the bottom for that of Park. Note that the calculated CO_2 VDF as a function of the vibrational energy takes the form of a 'cloud of points'and not a simple curve, as it happens for diatomic molecules, due to the non-biunique correspondence between the vibrational states and the vibrational energies. Indeed comparable energies can correspond to completely different vibrational quantum terns (v_1, v_2, v_3). For the Diss./Rec. kinetic scheme, the McKenzie model yields strongly dominating CO_2 recombination close to the surface, with significantly over-populated high states, whereas the Park model shows prevailing CO_2 dissociation, leading to the depletion of upper levels. As is shown in [279], these differences between models appear for the exchange reactions, too. The choice of the model strongly affects the results also when all the processes are considered (red points in the figure): the McKenzie model leads to higher VDF which is obviousely out of equilibrium. The Park model yields almost Boltzmann VDF on the surface. Thus the use of different parameters in the Arrhenius law leads to a significant modification of the surface VDF and shifts the chemical reaction mechanism.

In Fig. 27, the CO_2 average vibrational energies along the stagnation line calculated in the same test cases are compared. It is seen that when only dissociation and recombination are taken into account, the vibrational energy on the surface occurs much higher; including vibrational energy transitions and exchange reactions to the kinetic scheme yields a strong decrease in the CO_2 vibrational energy. Analysis carried out in [279] shows that the main role in this deactivation belongs to the vibrational kinetics and, to a much lesser extent, to exchange reactions.

It has been stressed above that, in hypersonic applications, it is important to take into account all vibrational states of the involved molecules. This can be seen from Fig. 27 where the vibrational energy calculated using the model based on the set of vibrational levels proposed in [254], i.e. all states of the asymmetric mode and a few lowest states of other modes is also plotted. This model is further referred as AMK (asymmetric mode kinetics); in the present simulations, the AMK model is used together with the McKenzie chemistry and full kinetic scheme in-
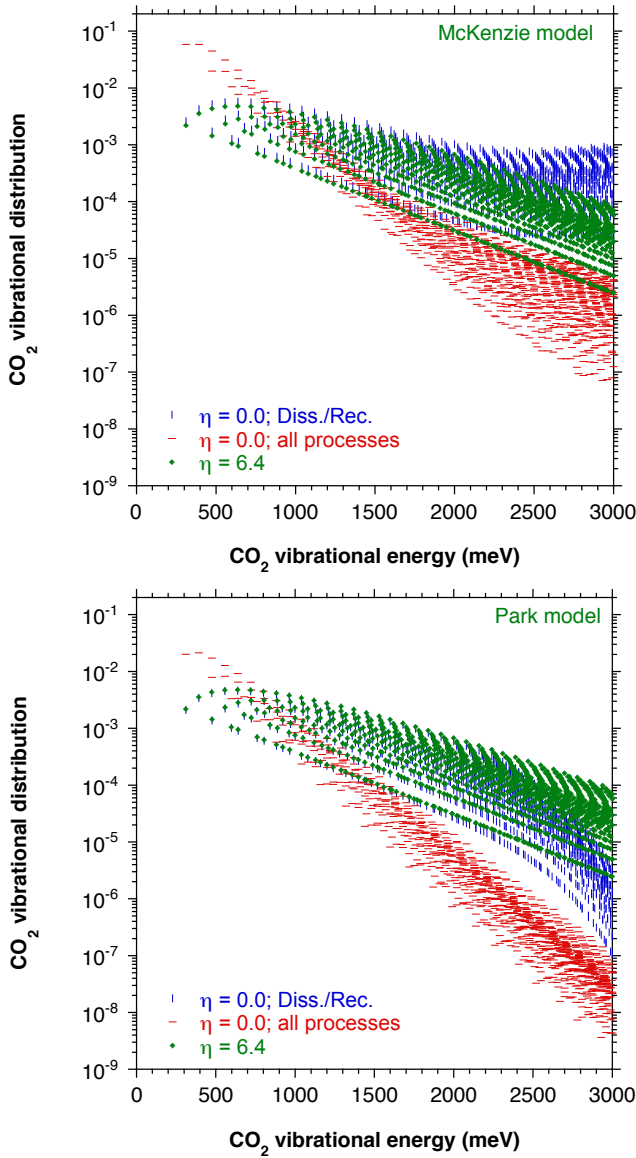
Fig. 26. CO_2 vibrational distributions calculated by Armenise and Kustova with the McKenzie model (top) and the Park model (bottom).

cluding all processes. The CO_2 average vibrational energy trend obtained using the AMK model is almost the same as the trend obtained by considering only dissociation and recombination with the McKenzie model, however the values are lower than in the latter case. Whereas near the surface, the vibrational energy is not far from that obtained with other models, near the external edge it converges to a much lower equilibrium value. This confirms the necessity of taking into account all vibrational states under high-temperature conditions (see [278] for detailed discussion).

Let us discuss now the heat flux. First of all, the main contribution to the total heat flux near the surface is given by thermal conductivity and thermal diffusion [276, 277] whereas the role of mass diffusion and vibrational energy diffusion is weak due to non-catalytic boundary condi-
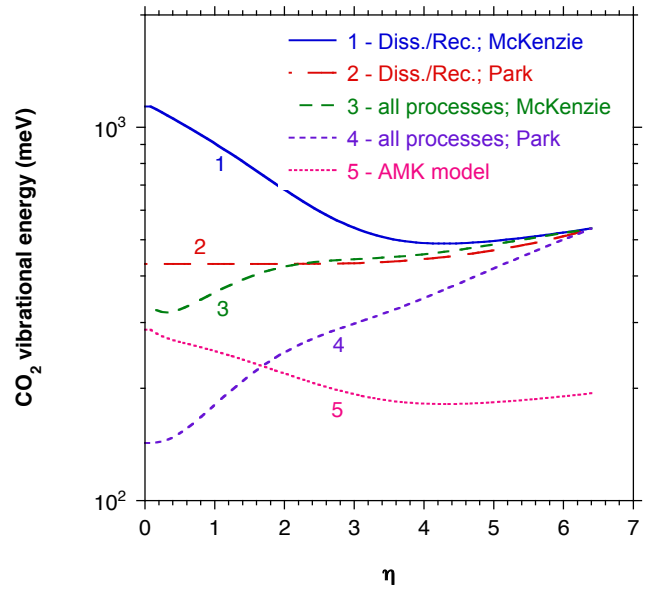

Fig. 27. CO_2 vibrational energy calculated by Armenise and Kustova with the McKenzie and the Park models and different kinetic schemes. AMK corresponds to the set of vibrational states proposed in [254].

tions; moreover, contributions of $\mathbf{q}_F$ and $\mathbf{q}_{TD}$ are comparable. Next, the values of the calculated heat flux due to thermal conductivity are close to that measured in experiment [337], $\mathbf{q}_{exp} = 8.2 \pm 1$ MW/m^2; the lowest heat flux of 6.36 MW/m^2 is obtained for the Park model, and the highest, 9.70 MW/m^2, for the McKenzie chemistry. Thus, one can conclude that the effect of chemical reactions is important even for a non-catalytic surface. The total heat flux calculated by Armenise and Kustova for the considered test cases is presented in Fig. 28. It is interesting that the two Diss./Rec. schemes with the Park and McKenzie models yield significantly different results whereas adding other kinetic processes leads to closer values near the surface. The total heat flux obtained with the AMK model, is almost the same as the one obtained by considering only dissociation and recombination reactions with the McKenzie model. There is, however, a discrepancy near the surface. Nevertheless, the surface heat flux calculated on the basis of the AMK model is close to the flux obtained using the Park model and the complete kinetic scheme.

8 Role of surfaces

The influence of surfaces on the plasma dynamics is obviously of prime importance when the pressure is low enough for diffusion to the wall to be fast compared with collision processes. For example, in the "glow" discharge at a few mbar presented in the previous section 7, the vibrational de-excitation of CO_2 at the walls can be the dominant gas heating mechanism for $p=1$ Torr [63] and have a significant effect in the relaxation of the vibrationally excited
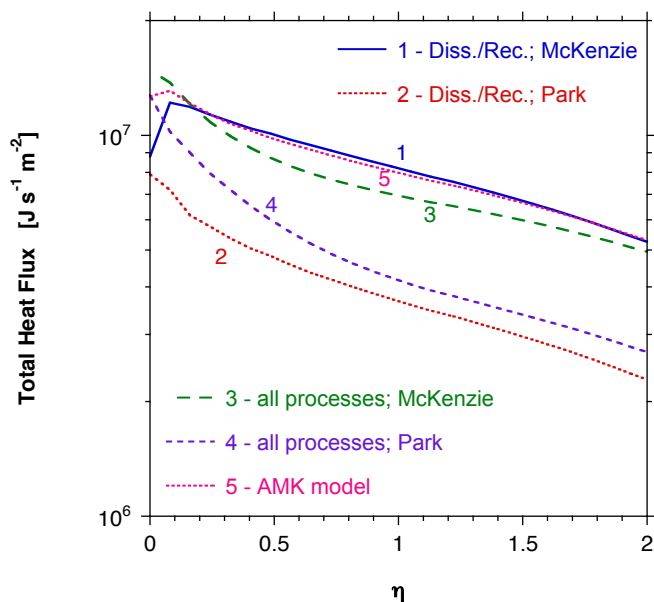
Fig. 28. Heat flux calculated by Armenise and Kustova with the McKenzie and the Park models and different kinetic schemes.

states in the afterglow [94], and most of the oxygen atoms recombine into O_2 (or CO_2) on surfaces. The very purpose of certain applications at reduced pressure such as the coating or functionalisation of polymers [21, 367], or the design of spacecraft heat shields [32, 33, 135] necessarily requires an understanding of the microscopic mechanisms of plasma-surface interaction. However, it would be wrong to believe that surfaces play an important role only at low pressure. Plasma/catalysis coupling for CO_2 conversion for instance is a good example of the key role that plasma-surface interaction can have even at atmospheric pressure.

Despite the importance of surface mechanisms, the information available in the literature remains scarce. The studies carried out often focus on one aspect only of plasma-surface interaction which is at the heart of the targeted application without considering other effects which may influence the plasma. For example, most of the measurements of vibrational de-excitation on surfaces have been performed to optimise CO_2 lasers and involve only an extremely limited number of the lower vibrational levels [165–167, 169], while most of the O atoms recombination probability at the walls have been measured in the context of space heat shields [368–371]. As a result, there is still a lack of global understanding of surface influence on CO_2 plasmas. This is partly due to the strong specificity of each parameter controlling the surface mechanisms according to the physico-chemical characteristics of each material, both at the microscopic and macroscopic levels. For example, there is not a single value for the recombination probability of oxygen atoms (γ_O) on a quartz surface: this probability depends on the topology of the surface, its stoichiometry and the surface coverage, all of which fluctuate when the surface is under direct plasma exposure. In ad-

dition, the surface temperature and the excitation state of the species coming from the gas phase and interacting with the wall will also influence the surface processes. Giving a reaction rate for a surface process is therefore very delicate and requires to characterize all these parameters simultaneously. The situation is even more complex in high pressure plasmas which tend to filament and therefore induce very strong spatial inhomogeneity. For example, the local surface temperature in the footprint of a streamer is never precisely known, but can largely influence the surface reactivity induced at this location.

Another issue is the difficulty to describe all the possible interaction mechanisms that can arise at plasma-surface with a single type of model. Indeed, mechanisms as different as ion bombardment, mobility of atoms and molecules on surfaces, chemical reactivity at the walls, the charge of dielectrics in contact with the plasma, or secondary emission phenomena, each require specific approaches to be described on different spatial and temporal scales. For instance, the latter can range from the fs associated with the vibrational motion of the surface and adsorbed species to few seconds or even minutes associated with surface modifications observed experimentally. Ranging from the smaller (shorter) to the larger (longer) space (time) scales, models can rely on density functional theory (DFT), molecular dynamics, kinetic Monte Carlo, coarse-grained deterministic models, or macroscopic formulations. A brief overview of these different approaches is given, *e.g*, in the sections devoted to plasma-surface interactions in refs [184, 219]. Moreover the description of these surfaces mechanisms are generally complex to couple with a fine description of the plasma bulk phase.

In the remainder of this section, some of the most studied mechanisms of plasma-surface interactions are described one by one starting with i) collisions of vibrationally excited molecules with surfaces, ii) recombination of oxygen atoms at the walls, iii) initiation of plasma filaments at atmospheric pressure in the pores of catalysts and the associated chemical reactivity.

8.1 Collisions of vibrationally excited molecules with surfaces

As described in the previous sections, energy transfers on the vibrational levels of CO_2 (and CO) are essential in the description of CO_2 plasmas. The collision of vibrationally excited CO_2 or CO molecules with surfaces is in itself a complex phenomenon. Indeed most of the time, in gas phase kinetic models, CO_2(v) interaction with surfaces is treated as simply the loss of one vibrational quanta with a certain probability γ_v. However the internal energy state with which the molecule leaves the surface can actually be much more varied.

For the optimisation of the CO_2 lasers it was important to minimise the vibrational de-excitation, in particular of the first asymmetrical CO_2(001) level. Parameters such as de-excitation probability and accommodation coefficient have been measured typically in experiments exciting a specific vibrational level with a pulsed laser,

and collecting fluorescence after interaction of the excited molecular beam with various materials [372] as already mentioned in section 2.4. This has been done for the first asymmetric stretch level $CO_2(001)$ on dielectric materials (quartz [165], Teflon, Brass, Mylar or Pyrex [166,169]) and metals (stainless steel, silver or nickel [168]) but also, for instance $CO_2(101)$ and $CO(v=2)$, on polycrystalline silver [167]. These measurements have shown large de-excitation probabilities (typically from 0.1 to 0.4 for $CO_2(001)$) decaying with the gas and surface temperatures. They have also suggested an influence on the accommodation coefficient of the type of molecules adsorbed on the surface, which may favour more or less the energy transfer to the wall. In particular, the capability of a material to adsorb CO_2 favours the energy transfer from $CO_2(v)$ to the wall. Semiclassical molecular dynamics calculations of oxygen atomic recombination have addressed the question of the internal state of the formed $O_2(X,v)$ molecule and of the energy transfer between the surface phonons and the O atoms, calculating the energy transferred to the surface [373,374]. However, molecular dynamics simulations of the vibrational energy transfers from excited gas molecules to surfaces are scarce [375] and often focus on the deactivation in liquid surfaces [376–378].

In the case of planetary entry heat shields, vibrational de-excitation can be a significant source of surface heating. The kinetic energy of the molecules impacting the surface can be high, and some works investigate the translational, rotational and vibrational states of the molecules after colliding onto the surface. Experimentally the change of CO and CO_2 ro-vibrational state can be monitored by infrared emission after impacting a heated platinum plate for instance [379]. The sticking coefficient of CO_2 appears to increase with vibrational energy state for low translational energy as measured by time resolved electron energy loss spectroscopy in [380]. Incoming vibrationally excited molecules can also react chemically on the surface by dissociative adsorption [381], where quasi-classical trajectory calculations performed over a potential energy surface (PES) for the dissociative chemisorption of CO_2 on Ni(100) has revealed an increase of dissociative chemisorption with the vibrational excitation of the incoming molecule, or enhanced chemical reactions with previously adsorbed species [191,372].

The behaviour of an excited molecule impinging on a surface is therefore a complex dynamic interaction which depends on the molecular internal energy, the gas and surface temperatures, the species covering the surface, the impact energy and orientation angle as well, as the structural and chemical characteristic of the material itself. Thus there is an important lack of experimental and modelling data to address this important issue not only for heat shields, but for any use of CO_2 plasmas. Many different approaches are being considered to address this topic, combining experiment and modelling such as in [382], with classical trajectory calculations describing the rotational distribution CO_2 molecules resulting from the impact of molecular beam on perfluorinated monolayer. "Exotic" reaction pathways can also be evidenced on surface such as

the dissociation of CO_2^+ ions into C and O_2 on Au surface for large ion energy [383]. However one of the most studied chemical reactions on surfaces exposed to CO_2 plasma is probably the recombination of O atoms.

8.2 Surface recombination of atomic oxygen

The recombination of oxygen atoms on surfaces is a key process in many ways:

– it is an exothermic process that can help to heat surfaces (like heat shields);
– the high chemical reactivity of oxygen atoms gives them an essential role in different domains, such as polymer treatment processes, or plasma-catalysis coupling;
– oxygen atoms can contribute to the reverse reaction mechanism giving back CO_2 from CO, and to the vibrational de-excitation of CO_2.

The key role of O atoms as very efficient quenchers of the CO_2 vibrations, even though already described in the CO_2 laser community, has been recently clearly evidenced by using large surface area silica surfaces to strongly recombine O atoms and monitoring the changes in the CO_2 vibrational distributions [108]. The effect is further investigated by modelling in a couple of preliminary simulations [39,94] that confirm its importance in low-pressure discharges.

Experimentally, the O atom recombination probability (γ_O) deduced from its loss frequency is the parameter that has been the most investigated either by emission spectroscopy (actinometry), laser induced fluorescence, or calorimetry, as described in section 2.4 [32,33,93,134, 135,384,385]. Different materials have been investigated, although most of the data have been obtained on Silica based materials, and in particular β-cristobalite. Even considering a given material, the recombination probability can vary with the roughness of the surface [108,386]. Typical γ_O values measured are in the range 10^{-4}-10^{-2} often with an Arrhenius dependence with surface temperature [387]. However, when a wide range of values of the surface temperature are considered, complex non-Arrhenius and even non-monotonic dependencies have been observed [388], usually explained by a competition between the Eley-Rideal (ER) and Langmuir-Hinshelwood (LH) surface recombination mechanisms [389]. Moreover, it has been shown both in pure O_2 plasmas [390] and in CO_2 plasmas [93] that γ_O also follows an Arrhenius law with the gas temperature suggesting an influence of the kinetic energy of the incoming O atoms. Despite the variability of γ_O values with temperatures and materials, general trends can be evidenced. For instance, γ_O values are systematically higher in O_2 plasma than in CO_2 plasma [93,191], which could be a consequence of lower reaction rate of back reaction CO+O on surface than the recombination into O_2 [130,135,150]. It is also worth noting that in pure O_2 plasma, γ_O values are in general higher when the surface is under plasma exposure than in temporal or spatial

post-discharge [390, 391] while such difference is not observed in CO_2 plasma [93]. It is usually claimed that O atoms recombination proceed through ER at moderate-to-high surface temperatures and that LH becomes important at low surface temperature for which the surface coverage of O atoms becomes larger. However the mechanisms responsible for O atoms recombination are still under debate. Different modelling approaches have been used to get insight into these mechanisms, including DFT [392–395], molecular dynamics [373, 396–398], Kinetic Monte Carlo [399–406] and mesoscopic deterministic models [368, 371, 388, 389, 407–411].

8.3 Role of surfaces in plasma-catalyst coupling

Surfaces also play a key role in the context of plasma catalysis which is one of the most promising approach to achieve efficient CO_2 recycling. In spite of the numerous results obtained already in plasma-catalytic CO_2 conversion, the underlying mechanisms are not yet completely understood. Modelling can help to unravel these mechanisms, but models describing plasma-catalyst surface interactions are very scarce, and until now have often been applied to other molecular systems than CO_2. Here we briefly describe some examples of the most advanced model results, even if they are not applied to CO_2 (e.g. NH_3 or CH_4) as they highlight the specificity of the chemical reactions induced on catalytic surfaces directly exposed to a plasma. These mechanisms, which differ significantly from what is observed in thermal catalysis, are essential to understand and optimise for developing efficient CO_2 conversion processes.

Some models have been developed to describe the catalyst surface chemistry upon impact of plasma species, by means of 0D (microkinetics) plasma chemistry and/or catalyst surface chemistry models, e.g., for plasma-catalytic NH_3 synthesis [412–415], non-oxidative coupling of CH_4 [416], and very recently also for CO_2 hydrogenation [417] and CH_4 partial oxidation [418]. Such models reveal the reaction pathways at the catalyst surface and the role of plasma-generated radicals and (vibrationally or electronically) excited.

A very interesting point is that reactions occuring on a catalytic surface under direct plasma exposure can exhibit a Non-Arrhenius behavior of the reaction rates. Indeed, the use of plasma catalysis gives rise to hybrid reactions in which the reactants are excited by electron impact before to proceed to reactive pathway on active sites of the catalysts [419]. Fig. 29 reports the experimental data measured by Nozaki and Okazaki [419] of the reaction rate as a function of $1/T_{gas}$ for the steam reforming of methane in a flow of N_2 and H_2O using a DBD reactor packed with a Ni/Al_2O_3 catalyst by considering the effect of catalyst with and without the plasma. As observed in Fig. 29 (left panel), the electron action in plasma environment does not cause significant modification in the activation energy, suggesting a unique elementary process in both processes. However, there is a perceptible difference in pre-factor parameter describing the rate, suggesting the synergetic ef-

fect of plasma and catalysis in increasing the rate. As observed in Fig. 29, a variation of the apparent activation energy of the process as a function of $1/T_{gas}$ is manifest in both cases, having the same trend for the corresponding change in the catalyzed reaction. Such convex curvature in Arrhenius plot (super-Arrhenius behavior), is usually described by the break-temperature formula [420, 421] (see left panel), invoking two distinct mechanisms. However, recent progress in uniformly interpreting deviation from Arrhenius behavior recommends the use of the following deformed version of the Arrhenius law

$$k(T) = A \left(1 - d \frac{\epsilon^{\ddagger}}{RT} \right)^{\frac{1}{d}}, d = \frac{RT_0}{\epsilon^{\ddagger}} \qquad (39)$$

called Aquilanti-Mundim formula, which simplifies the interpretation assuming the curvature as manifestation of collective phenomena, including particle diffusion effect and constraints on proposed microscopic model [420, 422–424]. In Fig. 29 (right panel), a fit of the rate is provided by the Aquilanti-Mundim formula, requiring one parameter less than the break-temperature model of the left panel, and providing physical meaning for the two parameters, $\epsilon^{\ddagger}$ as an Arrhenius-Eyring type reaction barrier and T_0 as the minimal temperature for the onset of the process without and with plasma. When d, which is a combination of previous parameters (see Fig.29) tends to zero, the Arrhenius formula is recovered [423]. The use of the formula permits to quantify the increase of the catalyzing action by the plasma as a factor four, according to ratio of A prefactors. At low temperature, it is apparent that the process suffers an intrinsic decrease in efficiency, without and with plasma catalyst: this is seen in an equivalence between both processes converging to the same same energy *ca* 4 kJ/mol, quantified by the common T_0 (*ca* 493 K) provided by application of eq. 39

Other approaches can be used to investigate the modified reactivity of the surface when exposed to the plasma. For instance the change of reactivity due to surface charging and effect of electric field induced onto the surface can be described by density functional theory (DFT) simulations, for CO_2 activation on (Al_2O_3-supported or TiO_2-supported) Cu, Ti and Ni surfaces [398, 425, 426]. The authors reported that a negative surface charge significantly enhances the reductive power of the catalyst, thus promoting CO_2 splitting into CO and O. Furthermore, the relative activity of the transition metals was found to be changed upon charging, suggesting that controlled surface charging may allow tuning of the catalyst activity and selectivity. In a typical DBD reactor, the plasma streamers will be statistically distributed over the entire dielectric surface. Therefore, even though the time and area of interaction of an individual streamer with the surface is relatively small in proportion to the macroscopic surface area, the surface deposition of charge is sufficient to induce a large surface field for the essential period of the applied voltage. Moreover, the plasma-catalyst coupling can also be studied with reduced pressure plasma sources, which are much more homogeneous than DBDs. Hence, plasma-
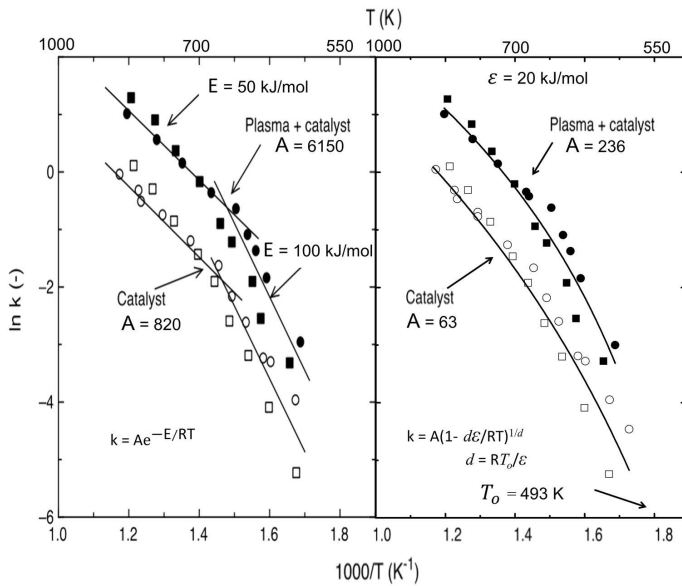
Fig. 29. The plasma reforming of CH_4 in a DBD reactor packed with 12 % Ni/Al_2O_3 catalyst. Left hand panel: Arrhenius-break plot. Right hand panel: super-Arrhenius plot uniformly described by Eq. (39).

induced catalyst surface charging may be important to explain plasma-catalyst synergistic effects.

Furthermore, the plasma does not only affect the catalyst surface chemistry and reactivity, but vice versa, the catalyst (packing) also affects the plasma behavior, such as electric field enhancement near the contact points of beads in packed bed DBDs [427], as well as streamer propagation in packed bed DBDs [428, 429] and in more complicated packing geometries, such as honeycomb and 3D fiber deposition (3DFD) structures [430]. An important research question in plasma catalysis is whether plasma (streamers) can penetrate into catalyst pores, because this defines the catalyst surface area exposed to the plasma (species), and thus the surface area available for plasma-catalytic reactions. A few research groups tried to answer this question by experiments. Holzer et al. reported the presence of short-lived oxidants inside porous catalysts for pore sizes around 10 nm, and suggested this is either due to formation inside the pores in case of strong electric fields, or due to diffusion into the pores and stabilization of these species upon adsorption on the pore inner surface, thus prolonging their lifetime inside the pores [431, 432]. On the other hand, Hensel et al. demonstrated that micro-discharges could only be formed inside pores for pore sizes around 15 μm, while only surface discharges were created outside the pore for pore sizes of 800 nm [433]. When studying the physical properties of micro-discharges for various pore sizes, discharge powers, and gas mixtures, the authors concluded that the onset voltage for micro-discharge formation inside pores drops upon rising pore size [434]. Hence, the pore size and amplitude of the applied voltage were identified as the critical parameters for micro-discharge formation inside pores [435].

By means of modeling, additional insight can be obtained on the inherent mechanisms behind micro-discharge formation in catalyst pores, and it was revealed that the pore size must be larger than the Debye length to allow plasma formation inside the pores [436]. Zhang et al. developed a 2D fluid model for the plasma behavior inside catalyst pores with μm dimensions, in a helium DBD [437], and studied the effect of different dielectric constants of the support material [438], as well as the effect of the pore shape [439]. The calculations revealed that the electric field is significantly enhanced near tip-like structures, and the pore shape greatly determined the electric field enhancement, and thus the plasma properties. These fluid simulations predicted that plasma species can only be created inside catalyst pores with dimensions above 10 μm, as defined by the Debye length at the conditions under study, for (support) materials with dielectric constants below 50. While such pore sizes are of interest for structured catalysts, catalytic supports typically have nm-sized pores, which are thus too small for plasma formation inside the pores. However, these fluid simulations were applied to a uniform helium plasma, while for plasma catalysis, reactive gases are used, which exhibit streamer formation. The latter are characterized by much higher electron densities, and thus smaller Debye lengths. Hence, Zhang et al. performed PIC/MCC simulations to study plasma streamer penetration inside catalyst pores of both μm and nm sizes [440–442], for a DBD operating in dry air in filamentary mode. These calculations revealed that plasma streamers can indeed penetrate in catalyst pores of several 100 nm. This is illustrated in Fig. 30, which depicts the electron number density profiles inside pores with different diameters, calculated by the PIC/MCC simulations, for an applied voltage of -8 kV [436, 441]. The electron density reaches a maximum inside the pores for pore diameters of 600 nm and above, while it is negligible for a pore diameter of 400 nm. At the conditions presented in this figure, the Debye length was calculated to be 415 nm, which explains why plasma streamers could not penetrate into pores of 400 nm diameter, while they can penetrate into larger pores. The Debye length is in the order of a few 100 nm up to 1 μm at typical DBD conditions in air, depending on the operating conditions (defining the electron density and temperature in the plasma streamer). For higher applied voltages, plasma streamers may be able to penetrate into smaller pores, due to the higher plasma density and thus shorter Debye length.

Most of the studies conducted in plasma catalysis to date have been carried out in DBD reactors. The streamers developing in these reactors generate very important spatial inhomogeneities and deposit local surface charges, which make the fine understanding of the interaction mechanisms very difficult. The development of new techniques of *in situ* measurements under direct plasma exposure is necessary to have a better understanding of these mechanisms. Moreover, the study of plasma-catalyst coupling can be extended to other configurations than DBD, with more homogeneous plasma allowing a better control of the interaction with the catalyst.
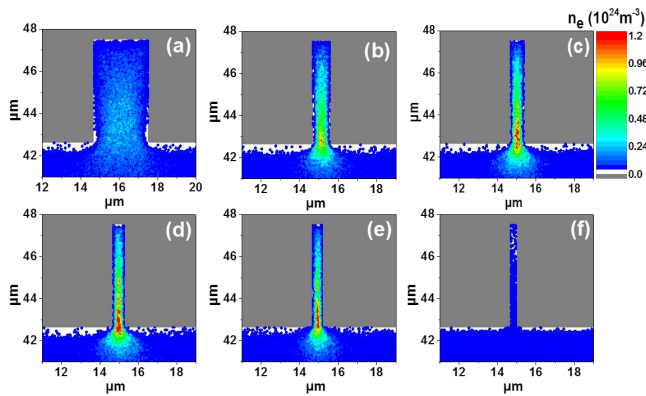
Fig. 30. Calculated electron density profiles, in (m^{-3}), near and inside a pore, with diameter of (a) 3 μm, (b) 1 μm, (c) 800 nm, (d) 700 nm, (e) 600 nm, (f) 400 nm, as obtained from PIC/MCC simulations in dry air, for an applied DC voltage of -8 kV. Adapted from [436] with permission.

9 2D/3D fluid models, necessity for spatial distribution description

The above 0D and 1D modelling approaches typically consider simple plasma setups, without focusing on reactor design. To investigate which reactor designs can lead to improved CO_2 conversion, 2D or even 3D fluid dynamics models are needed. However, such models require a long calculation time, certainly in case of complex geometries or gas flow patterns, such as supersonic flow or reverse vortex flow, which are of interest for improved CO_2 conversion (e.g., [8, 9, 443]). Therefore, a compromise must be made, by reducing the kinetic scheme, to keep the calculation time feasible. Several 2D or 3D models for plasma reactors typically used for CO_2 conversion, such as (packed bed) DBDs, MW and GA plasmas, are therefore in first instance developed in simple gases (e.g., helium or argon, or sometimes air), with limited chemistry (e.g., [427–429,444–462]). This gives useful information, e.g., on electric field enhancement near the contact points of packing beads in a packed bed DBD [427,444,445], on streamer propagation in a packed bed DBD [428, 429, 446–449], on plasma confinement in a MW plasma [450–454], or on arc behavior and gas flow patterns in a GA plasma [455–462].

Nevertheless, the plasma may not behave in the same way in CO_2 as in these (more) simple gases. Therefore, it is important to develop 2D or 3D fluid dynamics models in CO_2 as well. For the sake of computation time, this requires simplified kinetic schemes, as typically obtained from 0D modeling (see section 4).

Wang et al. developed a self-consistent 2D model for a classical GA plasma, with non-equilibrium CO_2 plasma chemistry [10]. The model was based on the chemistry set of the Kozák-Bogaerts 0D model (see section 4), but reduced for the sake of computation time. It considered five different neutral ground state species (CO_2, CO, O_2, O, C), five different ions, the electrons, and 11 different excited species, i.e., the four effective symmetric mode CO_2 vibrational levels of the Kozák-Bogaerts model, three

lumped groups for the CO_2 asymmetric mode levels, following the level lumping method of Berthelot and Bogaerts, as well as one CO_2 electronically excited level, and three O_2 vibrational levels. The model calculated the densities of all the plasma species, the electron temperature and gas temperature and the electric field in the GA plasma, as well as the gas flow profile. The species densities and the electron mean energy were calculated with continuity equations based on transport and on production and loss terms defined by the chemical reactions (and by Joule heating for the electron energy). The species transport was based on drift in the electric field and diffusion due to concentration gradients. The model assumed electrical neutrality in the arc plasma, and the ambipolar electric field was calculated from the charged species densities. The gas temperature was obtained by the heat transfer equation, and the gas flow, which was responsible for the arc displacement, was described by the Navier-Stokes equations, providing a solution for the mass density and the mass-averaged velocity. These Navier-Stokes equations were first solved separately, and the obtained velocity distribution was used as input in the other equations for the plasma behaviour and the gas heating. The calculated electron number density, CO_2 conversion and energy efficiency were compared with experiments, and showed reasonable agreement. The authors investigated the plasma characteristics in a whole GA cycle, and also performed a chemical kinetics analysis for the different pathways for CO_2 conversion.

Zhang et al. applied two fully coupled flow-plasma models (in 3D and 2D) for a magnetically stabilized GA plasma [463]. The 3D model was developed for argon, and allowed to compare the arc dynamics with those of a traditional (gas-driven) GA reactor, while the 2D model (developed in CO_2, with the same chemistry set as in [10]) provided more detailed information on how the external magnetic field can reduce the gas temperature by enhanced heat transfer, and how it can generate a velocity difference between the arc movement and the gas flow, to enhance the plasma-treated gas fraction, thus showing the potential of an external magnetic field to control the GA behavior.

Sun et al. presented a 2D model for a classical GA plasma, using a reduced chemistry obtained by the so-called directed relation graph method (see section 4) [264]. The authors showed the calculated 2D profiles of electron temperature, electron density, gas temperature and vibrational temperature at different moments in time, providing useful insights in the arc behavior of the CO_2 GA plasma.

Wolf et al. developed a 2D axisymmetric tubular chemical kinetics model, to study the effect of discharge contraction and vortex-induced radial turbulent transport on the CO production and destruction mechanisms in a vortex-stabilized CO_2 MW plasma reactor, in combination with experiments [303]. In this model, the power deposition was assumed to lead to direct gas heating, so vibrational kinetics was neglected, which was justified by the fast thermalization and the fact that thermal conversion dominates over vibration-induced dissociation at the high tempera-
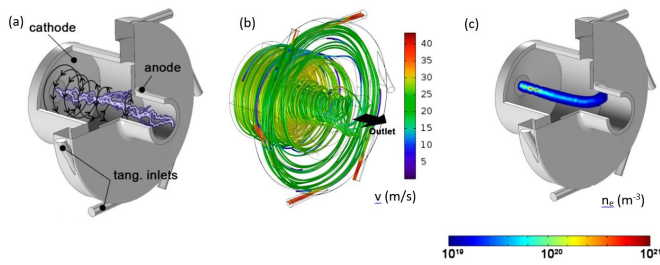
Fig. 31. (a) Internal structure of the GAP reactor, with schematic vortex gas flow pattern (black) and artistic representation of the arc (purple); (b) Calculated gas flow path lines, with velocity in m/s, showing the outer and inner vortex; and (c) calculated electron density profile $[m^{-3}]$ in the stabilized arc, after 5.3 ms, for 240 mA of arc current and an inlet gas flow rate of 22 L/min. Adopted from [464] with permission.

Fig. 32. Schematic illustration of the dual-vortex plasmatron (DVP) design, with artistic view of the position of the arc (purple). Adopted from [465] with permission.

tures under study. Five different species (CO_2, CO, O_2, O, C) and 26 chemical reactions were taken into account. The calculated CO_2 conversion and energy efficiency were in good agreement with experiments in a broad pressure range (from 80 to 600 mbar). The energy efficiency showed a maximum between 100 and 200 mbar, attributed to a discharge mode transition.

Trenchev et al. combined a 3D turbulent gas flow model with a 2D plasma and gas heating model for a gliding arc plasmatron (GAP) in CO_2 [464]. The CO_2 plasma chemistry included in this model was again the same as in [10]. In addition, the authors also developed a complete 3D gas flow and plasma model with simplified argon chemistry, to evaluate the gliding arc evolution in space and time. Indeed, the CO_2 plasma model could only be run in 2D within a reasonable calculation time, so the authors used the approach of "downgrading" a 3D argon model into 2D, and compared both, to validate the accuracy of this method. The difference between the 3D and 2D argon models was acceptable, so it could be assumed that the 2D CO_2 model also provided a reasonable picture of the plasma behavior.

Fig. 31 a illustrates the inner structure of the GAP, as used in the model, with schematic illustration of the vortex gas flow and artistic view of the arc position. The calculated 3D gas flow path lines and electron density profile, are depicted in Fig. 31 b and 31 c. The latter illustrates the position of the stabilized arc in the center of the GAP reactor. More details can be found in [464].

This model also showed the importance of including turbulent heat transfer, to obtain realistic values for gas temperature. The calculation results for electron temperature and density and gas temperature were compared with experiments from literature, to validate the model. The insights obtained in this study allowed to pinpoint the limitations in the GAP reactor design, such as non-uniform gas treatment, limiting the conversion, as well as the development of a hot cathode spot, resulting in severe electrode degradation. This also allowed the authors to propose solutions for improvement.
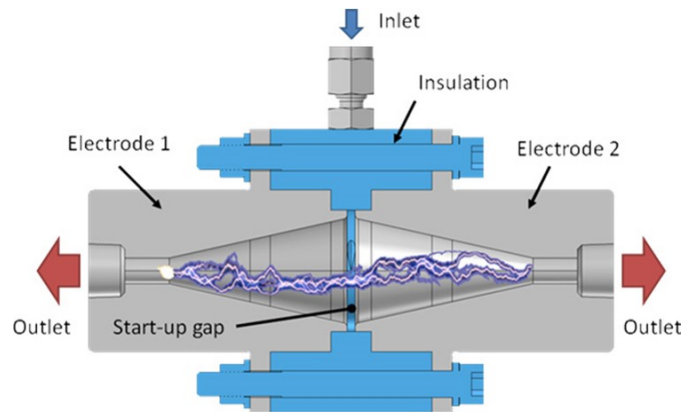
Indeed, in a later paper, the same authors proposed an improved design, called dual-vortex plasmatron (DVP), applying a similar modeling approach, i.e., combined Navier-Stokes equations for the gas flow behavior and 3D plasma model (in argon, for the same reason as above) [465]. This DVP is a GA plasma reactor with innovative electrode configuration, to solve the above problems (see Fig. 32). Indeed, the arc is elongated in two directions, so the gas residence time inside the arc is prolonged, thereby increasing the CO_2 conversion. At the same time, the cathode spot is actively cooled by rotation of the arc and gas convection. The measured CO_2 conversion and corresponding energy efficiency were indeed very promising. The combined fluid dynamics and plasma model allowed to study the gas flow and arc behavior in the reactor and to explain the experimental results.

The same authors also applied the combination of a 3D fluid dynamics model for the gas flow pattern and a 2D CO_2 plasma model to an atmospheric pressure glow discharge (APGD) [466]. In addition, they proposed improved designs based on 3D fluid dynamics simulations and insights obtained from the plasma model.

Fig. 33 (a) illustrates the basic APGD design, with a pin-to-plate configuration and simple gas inlet. It gave rise to an overall CO_2 conversion of only 3 – 4.5% (see Fig. 33 (d)), which could be explained from the model, as the plasma was confined to the center of the reactor. The conversion inside the plasma reached 75%, but due to the limited fraction of gas passing through the plasma, the overall conversion was much lower. The energy efficiency was around 30 % (see also Fig. 33 (d)). The authors proposed a modified setup, by employing a vortex flow generator, and Fig. 33 (b) illustrates the calculated gas flow path lines in this modified setup. The fluid dynamics simulations revealed that this vortex flow reduces the cathode temperature due to turbulence, and thus enables operation at higher power with longer interelectrode distance (22 mm instead of 18 mm in the basic design) without melting. Furthermore, the turbulence allowed somewhat more gas to pass through the plasma. Both effects lead to
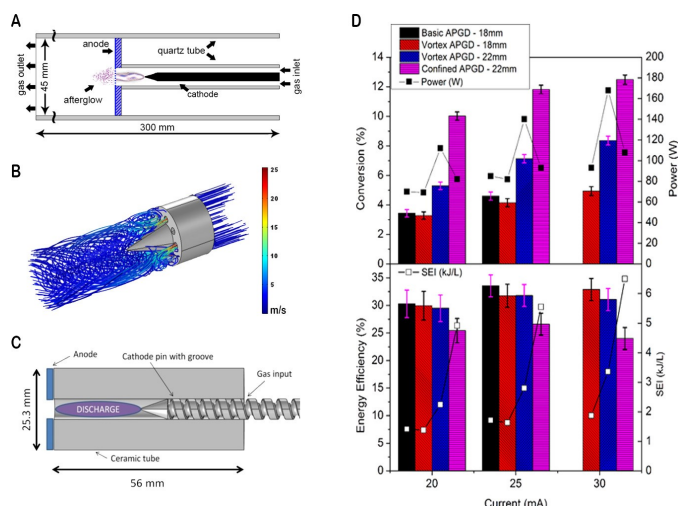
Fig. 33. Schematic illustration of the basic (A), vortex (B) and confined (C) APGD designs, as well as (D) conversion and energy efficiency obtained in these setups, at atmospheric pressure, at three different currents. The plasma power and corresponding SEI are also illustrated in (D). Adopted from [466] with permission.

a longer residence time of the gas in the plasma and to a higher conversion of about 8 % at the longer interelectrode distance of 22 mm (Fig. 33 (d)).

To further enhance the gas fraction passing through the plasma, the authors also designed a "confined" configuration, based on a ceramic tube with inner radius equal to the plasma radius, predicted by the model (see Fig. 33 c). A spiral groove in the cathode pin allowed to guide the gas into the tube and to cool the cathode pin, preventing it from melting, so that again a higher power could be used. In this confined design, the plasma fills the entire reactor, and thus all the gas molecules pass through the plasma, resulting in a higher conversion of up to 12.5 %, i.e., 3 times higher than in the basic APGD and 1.5-2 times higher than in the vortex flow design. On the other hand, the plasma is now in direct contact with the walls, causing heat losses and loss of plasma species towards the walls, resulting in a somewhat lower energy efficiency than in the basic and vortex flow APGD, i.e., ca. 26 %. The authors concluded that further improvements could be made, based on the concept of the confined configuration, in combination with turbulence and reducing the heat losses towards the walls. This example clearly shows how combined 3D fluid dynamics simulations and 2D (or 3D) plasma modelling is very useful to guide the experimental reactor design improvements.

10 Conclusions and perspectives

This review article presents both a comprehensive summary of the knowledge on CO$_2$ plasma kinetics and the experimental and theoretical results obtained in the last few years by different European research teams on the ac-

tivation of CO$_2$ in non-equilibrium plasmas under different conditions.

From an experimental point of view, very diverse measurements have been carried out (molecular beam experiments, swarm analyses, *in situ* infrared absorption in plasma discharges, *etc.*) often by distinct communities depending on the targeted applications (CO$_2$ lasers, spacecraft heat shields design, surface treatment, CO$_2$ recycling, *etc.*). All these experiments can provide valuable information and gathering them shows that many data have been measured on processes involving excited states, whether they are excited electronic states, vibrationally excited molecules or radicals (especially atomic oxygen). General trends can then be identified, such as the difficulty to keep the CO$_2$ vibrational temperature out of equilibrium for CO$_2$ partial density higher than 10^{23}m^{-3}. Despite this extensive literature, several important issues remain with the currently available experimental data: i) each parameter measured (density of a species, rate of a reaction, strength of the electric field, etc...) is measured in a specific configuration that is very difficult to compare with other studies, ii) the data on vibrational excitation are still limited to a low level of excitation, iii) the role of excited electronic states, in particular CO(a$^3\Pi$) and O(^1D), on the EEDFs as well as on the vibrational and chemical kinetics remains too little investigated; iv) the intense research effort carried out recently on CO$_2$ conversion too often provides only performance parameters (conversion rate, energy efficiency) without sufficiently measuring some essential properties of the plasma discharges used (electric field, electron density, vibrational temperatures, *etc.*). Despite these shortcomings, the recent work mentioned in this review shows the growing contribution of model/experiment comparisons, and in particular the interest of designing experiments specifically dedicated to validate particular points of the models.

From the modeling point of view, an important milestone in the understanding of CO$_2$ plasma conversion was represented by the work made by the group of Bogaerts et al [118, 256, 297] with their simulations based on a detailed 0D global model, including the vibrational kinetics of the asymmetric mode of CO$_2$ and an extended plasma chemistry, describing the relevant chemical processes involving both neutral and ion species. On the other hand, Pietanza et al [269, 273, 274] reported results of their state to state kinetics coupled to a time dependent solution of the EEDF, this approach becoming important when the EEDF is far from equilibrium, as occurring in different conditions characterizing MW and nano-pulse discharges, even at high gas temperature, in which thermal equilibrium is generally assumed. Another important step forward in the development of simulation codes for the CO$_2$ plasma description was made jointly by the group of Guerra et al. in collaboration with the experimental groups of Guaitella et al. and Engeln et al..They described in a very accurate way the behavior of a DC CO$_2$ glow discharges at low dissociation conditions, with the inclusion in the model of the first few (approximately 70) CO$_2$ mixed vibrational levels. A systematic mutual step-by-

step validation procedure of their results allowed to separately investigate the role of V-V and V-T transfers [60, 61], e-V excitation [62] and gas heating [63, 64]. Two particularly revealing results of the benefit of a joint model / experiment approach are the identification of the best CO_2 dissociation cross section by electron impact for E/N values below 100 Td [89], and the evidence of the key role of $CO(a^3\Pi)$ in the 'back reaction mechanisms 'with O_2 at low gas temperature giving back CO_2 [131, 148]. A much more extended vibrational kinetic model for the CO_2 system was proposed by Armenise and Kustova [46, 277], but applied to the investigation of the hypersonic entry of vehicles in Mars atmosphere. In their case, however, electrons do not appear in the model (the temperature is not so high for their generation), simplifying the global kinetic description. Under hypersonic flow conditions, the STS model has to account for all vibrational states in the stretching and bending modes. The flow dynamics and heat flux strongly depend on the parameters in the Arrhenius law; using different sets of parameters yields various dominating reaction mechanisms.

Important input data for kinetic models are electron impact cross sections and heavy particle rate coefficients. For this reason, the present review reported an in-depth analysis of an approach based on numerical scattering calculations, the QCT method (see section 3), relying on the use of appropriate full dimensional PESs, which in principle can provide complete sets of vibrational energy exchange rate coefficients for VV and VT energy transfers involving CO_2 and other species and also for vibrationally activated CO_2 dissociation. Examples of QCT calculations of VV and VT rate coefficients for the CO_2-CO_2 and CO_2-N_2 performed by Lombardi et al. [55, 56] were reported. A focus on the Boudouard collision process [154], important for the CO kinetics, was also provided, showing the recent calculations by quantum mechanical approach of its activation energy. Moreover, an accurate overview of the most recent available electron impact cross sections sets used for the EEDF calculations in CO_2 plasma kinetic models was also presented.

All the points mentioned above illustrate the complexity of obtaining an accurate and detailed description of CO_2 plasmas even in 0D. However, in order to get closer to real systems, it is essential to take into account the important effects induced on the one hand by the surfaces in contact with the plasma, and on the other hand by the sometimes very complex fluid dynamics taking place in CO_2 conversion reactors. The plasma/surface interaction is generally still poorly understood and a research topic in itself, especially for relatively high pressures (above a few mbar). In the case of CO_2 plasmas, the vibrational de-excitation and recombination of oxygen atoms on different materials would require further experimental and theoretical work. Plasma/catalysis coupling is a special case of plasma/surface interaction which certainly represents a promising way for CO_2 conversion. The demonstration of the singular reactivity induced by plasma on the surface of catalytic materials exhibiting reaction rates deviating from the usual Arrhenius laws, as well as the

fundamental role of the charges deposited on the surface on the adsorption/desorption processes and the initiation of the plasma filaments themselves, are among the recent results of the groups of Aquilanti et al and Bogaerts et al which illustrate the key role of surfaces on the plasma dynamics.

The present review has opened the way to new perspectives for collaboration among the different modeling and experimental research groups to improve the accuracy of the CO_2 plasma description. In particular, several open problems still need to be addressed and could be summarized in the following few points:

1. development of more accurate electron impact cross sections and heavy particle rate coefficients involving excited states for both CO_2 and CO molecules and minority species;
2. development of a more complete vibrational energy level scheme for CO_2;
3. design of new experiments and simulations to allow for joint step-by-step validation procedure in broader range of conditions.

Concerning the first point, we would like to focus the attention on two important processes, namely the dissociation of CO_2 by electron impact and the same process by collisions with heavy particles, which are of fundamental importance for the description of CO_2 dissociation in plasmas. After many discussions, the accepted electron impact dissociation cross section by electron impact from ground state at low-to-moderate reduced electric fields is the one proposed at the beginning of plasma chemistry by Polak et al [206]. This cross section is the best one for reproducing recent experimental results for conditions characterized by low excitation regime [89]. However, for higher excitation, the dissociation cross sections from higher vibrational levels should be included in models. Usually, these cross sections are calculated starting from the ground state cross section by using approximated scaling laws or just with a shift of the threshold energy according to the vibrational energy of the level. A crucial point is to provide a more accurate description of the dependence of such cross sections on the excited states (vibrational or electronic). This can be done by using appropriate quantum mechanical calculations [236].

Similar observations can be made for the dissociation process of CO_2 by heavy particles, i.e. $CO_2(v) + M \rightarrow CO + O + M$. This process is described by an Arrhenius rate coefficient, in which the activation energy is corrected by a phenomenological parameter (α) introduced many years ago by Fridman and Macheret to describe the decrease of the activation energy of the process with the vibrational energy of the involved levels, or by the Marrone-Treanor model. Also in this case, a robust scattering calculation approach based on the presented QCT method would be beneficial for calculating the corresponding rate coefficients with their dependence on the vibrational level energies. For the CO system, cross sections and their dependence on the vibrational quantum number are much better known than the corresponding values for CO_2. As an example, Laporta et al [244] reported a quantum mechanical cal-

culation of the resonant dissociative attachment process, i.e. e + $CO(X^1\Sigma^+,v) \rightarrow CO^-(X^2\Pi) \rightarrow C(^3P) + O(^2P)$, showing a large dependence of the process on the vibrational quantum number. However, more theoretical and experimental studies are necessary to better describe some processes for the CO system, such as that one involving the $CO(a^3\Pi)$ state, i.e. $CO(a^3\Pi + CO(v=0) \rightarrow CO(v=0) + CO(v=27)$, in which the electronic excited energy is converted into the vibrational energy of the CO ground state, in particular of the v=27 state. This reaction could in principle pump different vibrational levels of CO with different effects on the CO VDF.

According to the second point, a more complete vibrational energy level scheme for CO_2 should be developed. As already pointed out in the review, the existing vibrational state-to-state models for studying CO_2 activation by non-equilibrium plasma take into account essentially the pure asymmetric mode levels, adding some low-lying CO_2 bending and symmetric levels. However, a new paradigm for the vibrational model levels of CO_2 should be developed in the future in order to include a more complete manifold of vibrational levels (depending also on computer resources) as already done by Armenise and Kustova [278, 364], but, at the same time, attention should be addressed to the construction of a coherent kinetic scheme in which all the included levels have their corresponding heavy particle rate coefficients and electron impact cross sections.

For the third point, until now the systematic validation between model and experiment could be carried out almost only in the case of glow discharge thanks to the great reproducibility and the homogeneity of these discharges. Low pressure glow discharges can still be used as an ideal benchmark for models in low excitation conditions since it is fairly reproduced even by 0D calculations. Work is in progress to cast light into some of remaining questions involving the CO_2 plasma kinetics and evolve towards a general reaction mechanism for CO_2 plasmas. In particular, ongoing investigation pursues the following axes: (i) investigation of vibrational energy exchanges within the complete vibrational ladder of CO_2 [467]; (ii) validation of the vibrational energy transfer rate coefficients for collisions between CO_2 and other species, namely CO_2-CO and CO_2-O; (iii) influence of impurities such as N_2 [94] and H_2O [468] and other admixtures on the CO_2 kinetics. It is also essential to extend the model/experiment comparisons to other discharge regimes which requires efforts from both experimentalists and modelers:

- the basic parameters controlling the plasma properties (electric field, electron density, gas temperature) should be measured in different CO_2 plasma discharges;
- the inhomogeneity of plasmas discharges studied must be evaluated by time and space resolved measurement methods, such as laser induced fluorescence techniques;
- emphasis should be put on model outputs that are easily measured experimentally, such as attempting to calculate the radiations from excited electronic states easily detectable in emission spectroscopy.

It would be particularly beneficial if standardised reactors could be developed to allow more relevant comparisons of the experimental measurements made by different groups, and thus serve more easily as reference for comparisons with models. Beyond the measurements performed in plasma discharges, it would be very valuable to perform new measurements on elementary processes in molecular beam and pump probe experiments for instance.

The study of CO_2 plasmas has received a great deal of attention in recent years, largely due to environmental concerns. However, the scope of this research goes far beyond CO_2 plasmas themselves and can benefit the understanding of all non-equilibrium plasmas in molecular gases. Indeed, CO_2 is at the same time a complex case study (triatomic molecule with three modes of vibration, two of which are coupled, *etc.*), but on which decades of research in different communities have made it possible to accumulate spectroscopic data, reaction rates, and data on fundamental processes that now allow to explore in detail the energy transfers and complex interactions at play in a plasma of a triatomic molecule. The tools and methods developed today for CO_2 can undoubtedly be useful to solve similar problems in cold plasmas in other gases such as SO_2, CH_4, NH_3, *etc.*. Vibrational excitation is a key feature of any cold plasma in a molecular gas. Achieving a detailed description of vibrational phenomena and their coupling with electronic and chemical phenomena in the test case of CO_2 will open the door to many areas of plasma chemical synthesis as well as studies in planetology and astrophysics.

Acknowledgement

Authors contribution

Pietanza and Guaitella are lead authors of the Topical Review having managed and organized the different contri-

butions. All the authors were involved in the preparation of the manuscript. All the authors have read and approved the final manuscript.

References

1. L.F. Spencer, A.D. Gallimore, Plasma Chemistry and Plasma Processing **31**, 79 (2011)
2. D. Premathilake, R.A. Outlaw, R.A. Quinlan, C.E. Byvik, Earth and Space Science **6**, 557 (2019)
3. Q. Huang, D. Zhang, D. Wang, K. Liu, A.W. Kleyn, Journal of Physics D: Applied Physics **50**, 294001 (2017)
4. R. Yang, D. Zhang, K. Zhu, H. Zhou, X. Ye, A.W. Kleyn, Y. Hu, Q. Huang, Acta Physico-Chimica Sinica **35**, 292 (2018)
5. S. Heijkers, R. Snoeckx, T. Kozák, T. Silva, T. Godfroid, N. Britun, R. Snyders, A. Bogaerts, The Journal of Physical Chemistry C **119**, 12815 (2015)
6. T. Silva, N. Britun, T. Godfroid, R. Snyders, Plasma Sources Science and Technology **23**, 025009 (2014)
7. N. den Harder, D.C.M. van den Bekerom, R.S. Al, M.F. Graswinckel, J.M. Palomares, F.J.J. Peeters, S. Ponduri, T. Minea, W.A. Bongers, M.C.M. van de Sanden et al., Plasma Processes and Polymers **14**, 1600120 (2017)
8. W. Bongers, H. Bouwmeester, B. Wolf, F. Peeters, S. Welzel, D. van den Bekerom, N. den Harder, A. Goede, M. Graswinckel, P.W. Groen et al., Plasma Processes and Polymers **14**, 1600126 (2017)
9. T. Nunnally, K. Gutsol, A. Rabinovich, A. Fridman, A. Gutsol, A. Kemoun, Journal of Physics D: Applied Physics **44**, 274009 (2011)
10. W. Wang, D. Mei, X. Tu, A. Bogaerts, Chemical Engineering Journal **330**, 11 (2017)
11. J.L. Liu, H.W. Park, W.J. Chung, D.W. Park, Plasma Chemistry and Plasma Processing **36**, 437 (2016)
12. R. Aerts, R. Snoeckx, A. Bogaerts, Plasma Processes and Polymers **11**, 985 (2014)
13. F. Brehmer, S. Welzel, M.C.M. van de Sanden, R. Engeln, Journal of Applied Physics **116**, 123303 (2014)
14. X. Duan, Y. Li, W. Ge, B. Wang, Greenhouse Gases: Science and Technology **5**, 131 (2015)
15. O. Taylan, H. Berberoglu, Plasma Sources Science and Technology **24**, 015006 (2014)
16. M.S. Bak, S. Im, M. Cappelli, IEEE Transactions on Plasma Science **43**, 1002 (2015)
17. M. Scapinello, L.M. Martini, G. Dilecce, P. Tosi, Journal of Physics D: Applied Physics **49**, 075602 (2016)
18. W.J. Witteman, *The CO$_2$ laser*, Vol. 53 (Springer, 2013)
19. L. d'Hendecourt, M. Jourdain de Muizon, Astronomy and Astrophysics **223**, L5 (1989)
20. S. Wyckoff, J. Theobald, Advances in Space Research **9**, 157 (1989)
21. A. Bousquet, G. Cartry, A. Granier, Plasma Sources Science and Technology **16**, 597 (2007)
22. M. Pérez-Mendoza, M. Domingo-García, F. López-Garzón, Carbon **37**, 1463 (1999)
23. D.J. Babu, S. Yadav, T. Heinlein, G. Cherkashinin, J.J. Schneider, The Journal of Physical Chemistry C **118**, 12028 (2014)
24. S. Ramos, G. Vasconcelos, E. Antunes, A. Lobo, V. Trava-Airoldi, E. Corat, Diamond and Related Materials **19**, 752 (2010)
25. T. Gokus, R.R. Nair, A. Bonetti, M. Böhmler, A. Lombardo, K.S. Novoselov, A.K. Geim, A.C. Ferrari, A. Hartschuh, ACS Nano **3**, 3963 (2009)
26. A. Nourbakhsh, M. Cantoro, T. Vosch, G. Pourtois, F. Clemente, M.H. van der Veen, J. Hofkens, M.M. Heyns, S.D. Gendt, B.F. Sels, Nanotechnology **21**, 435203 (2010)
27. N. Médard, J.C. Soutif, F. Poncin-Epaillard, Surface and Coatings Technology **160**, 197 (2002)
28. I. Gancarz, G. Poźniak, M. Bryjak, European Polymer Journal **35**, 1419 (1999)
29. A. Fahmy, A. Schönhals, Plasma Processes and Polymers **13**, 499 (2016)
30. V. Marieu, P. Reynier, L. Marraffa, D. Vennemann, F.D. Filippis, S. Caristia, Acta Astronautica **61**, 604 (2007)
31. G. Herdrich, M. Auweter-Kurtz, H.L. Kurtz, T. Laux, M. Winter, Journal of Thermophysics and Heat Transfer **16**, 440 (2002)
32. A.F. Kolesnikov, I.S. Pershin, S.A. Vasil'evskii, M.I. Yakushin, Journal of Spacecraft and Rockets **37**, 573 (2000)
33. N. Bykova, S. Vasil'evskii, A. Gordeev, A.F. Kolesnikov, I. Fershin, M. Yakushin, Fluid dynamics **32**, 876 (1997)
34. D. Vacher, M.L. da Silva, P. André, G. Faure, M. Dudeck, Plasma Sources Science and Technology **17**, 035012 (2008)
35. X. Lin, L.Z. Chen, J.P. Li, F. Li, X.L. Yu, Journal of Thermophysics and Heat Transfer **32**, 503 (2018)
36. K. Koizumi, M. Boero, Y. Shigeta, A. Oshiyama, The Journal of Physical Chemistry Letters **4**, 1592 (2013)
37. D. Wu, R.A. Outlaw, R.L. Ash, Journal of Vacuum Science & Technology A **14**, 408 (1996)
38. V. Guerra, T. Silva, P. Ogloblina, M. Grofulović, L. Terraz, M.L. da Silva, C.D. Pintassilgo, L.L. Alves, O. Guaitella, Plasma Sources Science and Technology **26**, 11LT01 (2017)
39. P. Ogloblina, A.S. Morillo-Candas, A.F.S. da Silva, T.P. Silva, A. Tejero-del Caz, L.L. Alves, O. Guaitella, V. Guerra, Plasma Sources Science and Technology (2021)
40. A.A. Fridman, *Plasma Chemistry* (Cambridge University Press, Cambridge, UK, 2008)
41. P. Capezzuto, F. Cramarossa, R. D'Agostino, E. Molinari, The Journal of Physical Chemistry **80**, 882 (1976)
42. R. Snoeckx, A. Bogaerts, Chem. Soc. Rev. **46**, 5805 (2017)
43. N. Britun, T. Silva, G. Chen, T. Godfroid, J. van der Mullen, R. Snyders, Journal of Physics D: Applied Physics **51**, 144002 (2018)
44. Y. Qin, G. Niu, X. Wang, D. Luo, Y. Duan, Journal of CO$_2$ Utilization **28**, 283 (2018)
45. A. George, B. Shen, M. Craven, Y. Wang, D. Kang, C. Wu, X. Tu, Renewable and Sustainable Energy Reviews **135**, 109702 (2021)
46. I. Armenise, E. Kustova, Chem. Phys. **415**, 269 (2013)
47. I. Armenise, P. Reynier, E. Kustova, J. Thermophys. Heat Transfer **30**, 705 (2016)
48. R.N. Schwartz, Z.I. Slawsky, K.F. Herzfeld, The Journal of Chemical Physics **20**, 1591 (1952)
49. C.E. Treanor, The Journal of Chemical Physics **43**, 532 (1965)
50. A. Zelechow, D. Rapp, T.E. Sharp, The Journal of Chemical Physics **49**, 286 (1968)

51. I.V. Adamovich, S.O. Macheret, J.W. Rich, C.E. Treanor, Journal of Thermophysics and Heat Transfer **12**, 57 (1998)

52. J.a. Vargas, B. Lopez, M. Lino da Silva, The Journal of Physical Chemistry A **125**, 493 (2021)

53. E. Kustova, M. Mekhonoshina, Phys. Fluids **32**, 096101 (2020)

54. A. Lombardi, N. Faginas-Lago, L. Pacifici, G. Grossi, J. Chem. Phys. **143**, 034307 (2015)

55. M. Bartolomei, F. Pirani, A. Laganà, A. Lombardi, J Comput Chem **33**, 1806 (2012)

56. A. Lombardi, F. Pirani, A. Laganà, M. Bartolomei, Journal of computational chemistry **37**, 1463 (2016)

57. PHYS4ENTRY Database. retrieved on January 2021, http://phys4entrydb.ba.imip.cnr.it/Phys4EntryDB/

58. IST-Lisbon database, www.lxcat.net, retrieved on October 5, 2020

59. LXCat, *LXCat database*

60. B.L.M. Klarenaar, A.S. Morillo-Candas, M. Grofulović, M.C.M. van de Sanden, R. Engeln, O. Guaitella, Plasma Sources Science and Technology **28**, 035011 (2019)

61. T. Silva, M. Grofulović, B.L.M. Klarenaar, A.S. Morillo-Candas, O. Guaitella, R. Engeln, C.D. Pintassilgo, V. Guerra, Plasma Sources Science and Technology **27**, 015019 (2018)

62. M. Grofulović, T. Silva, B.L.M. Klarenaar, A.S. Morillo-Candas, O. Guaitella, R. Engeln, C.D. Pintassilgo, V. Guerra, Plasma Sources Science and Technology **27**, 115009 (2018)

63. T. Silva, M. Grofulović, L. Terraz, C.D. Pintassilgo, V. Guerra, Plasma Chem. Plasma Process. **40**, 713 (2020)

64. M. Grofulović, B.L.M. Klarenaar, O. Guaitella, V. Guerra, R. Engeln, Plasma Sources Science and Technology **28**, 045014 (2019)

65. S. Trajmar, D.F. Register, A. Chutjian, Physics Reports **97**, 219 (1983)

66. Y. Itikawa, M. Brunger, O. Madelung, W. Martienssen, *Numerical Data and Functional Relationships in Science and Technology: Elementary Particles, Nuclei and Atoms. Photon and Electron Interactions with Atoms, Molecules and Ions/Ed. by Y. Itikawa. Interactions of Photons and Electrons with Molecules/M. Brunger...* (Springer, 2003)

67. A. Zecca, G.P. Karwasz, R.S. Brusa, La Rivista del Nuovo Cimento (1978-1999) **19**, 1 (1996)

68. G.P. Karwasz, R.S. Brusa, A. Zecca, Riv Nuovo Cimento **24**, 1 (2001)

69. J. Gallagher, E. Beaty, J. Dutton, L. Pitchford, Journal of Physical and Chemical Reference Data **12**, 109 (1983)

70. L.G.H. Huxley, R.W. Crompton, *Diffusion and drift of electrons in gases* (Wiley-Interscience: New York, 1974)

71. H. Blevin, M. Hasan, Australian Journal of Physics **20**, 735 (1967)

72. P. Purdie, J. Fletcher, Journal of Physics D: Applied Physics **22**, 759 (1989)

73. D.K. Davies, Journal of Applied Physics **47**, 1916 (1976)

74. P. Haefliger, C. Franck, Review of Scientific instruments **89**, 023114 (2018)

75. J.J. Lowke, A.V. Phelps, B.W. Irwin, J. Appl. Phys. **44**, 4464 (1973)

76. H. Saelee, J. Lucas, J. Limbeek, IEE Journal on Solid-State and Electron Devices **1**, 111 (1977)

77. M. Elford, G. Haddad, Australian Journal of Physics **33**, 517 (1980)

78. M. Yousfi, J. de Urquijo, A. Juarez, E. Basurto, J.L. Hernandez-Avila, IEEE Transactions on Plasma Science **37**, 764 (2009)

79. M. Vass, I. Korolov, D. Loffhagen, N. Pinhão, Z. Donkó, Plasma Sources Science and Technology **26**, 065007 (2017)

80. D. Rapp, P. Englander-Golden, The Journal of Chemical Physics **43**, 1464 (1965)

81. H. Straub, B. Lindsay, K. Smith, R. Stebbings, The Journal of chemical physics **105**, 4015 (1996)

82. H. Straub, P. Renault, B. Lindsay, K. Smith, R. Stebbings, Physical Review A **54**, 2146 (1996)

83. M. Mangan, B. Lindsay, R. Stebbings, Journal of Physics B: Atomic, Molecular and Optical Physics **33**, 3225 (2000)

84. T. Antoni, K. Jung, H. Ehrhardt, E. Chang, Journal of Physics B: Atomic and Molecular Physics **19**, 1377 (1986)

85. D. Register, H. Nishimura, S. Trajmar, Journal of Physics B: Atomic and Molecular Physics **13**, 1651 (1980)

86. M. Ristić, G. Poparić, D. Belić, Physical Review A **83**, 042714 (2011)

87. M.J. Brunger, S.J. Buckman, Physics reports **357**, 215 (2002)

88. M. Grofulović, L.L. Alves, V. Guerra, J. Phys. D: Appl. Phys. **49**, 395207 (2016)

89. A.S. Morillo-Candas, T. Silva, B.L.M. Klarenaar, M. Grofulović, V. Guerra, O. Guaitella, Plasma Sources Science and Technology **29**, 01LT01 (2020)

90. K.H. Kim, K.Y. Kim, Y.H. Hong, H.J. Moon, C.W. Chung, Physics of Plasmas **26**, 123516 (2019)

91. D. Zhang, Q. Huang, E.J. Devid, E. Schuler, N.R. Shiju, G. Rothenberg, G. van Rooij, R. Yang, K. Liu, A.W. Kleyn, The Journal of Physical Chemistry C **122**, 19338 (2018)

92. H. Li, Y. Zhou, V.M. Donnelly, The Journal of Physical Chemistry A **124**, 7271 (2020)

93. A. Morillo-Candas, C. Drag, J.P. Booth, T. Dias, V. Guerra, O. Guaitella, Plasma Sources Science and Technology **28**, 075010 (2019)

94. L. Terraz, T. Silva, A.S. Morillo-Candas, O. Guaitella, A. Tejero-del-Caz, L.L. Alves, V. Guerra, J. Phys. D: Appl. Phys. **53**, 094002 (2020)

95. R. Buser, J. Sullivan, Journal of Applied Physics **41**, 472 (1970)

96. N. Aleksandrov, S. Kindysheva, A. Kirpichnikov, I. Kosarev, S. Starikovskaia, A.Y. Starikovskii, Journal of Physics D: Applied Physics **40**, 4493 (2007)

97. F. Javier, S.H. Moreno, A.I. Stankiewicz, G.D. Stefanidis, International Journal of Hydrogen Energy **41**, 21067 (2016)

98. A. van de Steeg, T. Butterworth, D. van den Bekerom, A.F.S. da Silva, R. Van de Sanden, G.J. Van Rooij, Plasma Sources Science and Technology (2020)

99. X. Wang, Y. Gao, S. Zhang, H. Sun, J. Li, T. Shao, Applied Energy **243**, 132 (2019)

100. C. Montesano, S. Quercetti, L.M. Martini, G. Dilecce, P. Tosi, Journal of CO2 Utilization **39**, 101157 (2020)

101. G. Willems, A. Hecimovic, K. Sgonina, E. Carbone, J. Benedikt, Plasma Physics and Controlled Fusion **62**, 034005 (2020)

102. I. Adamovich, S. Saupe, M. Grassi, O. Schulz, S. Macheret, J. Rich, Chemical Physics **173**, 491 (1993)

103. E. Carbone, F. D'Isa, A. Hecimovic, U. Fantz, Plasma Sources Science and Technology **29**, 055003 (2020)
104. L. Spencer, A. Gallimore, Plasma Sources Science and Technology **22**, 015019 (2012)
105. D. van den Bekerom, A. van de Steeg, M. van de Sanden, G. Van Rooij, Journal of Physics D: Applied Physics **53**, 054002 (2019)
106. Y. Babou, P. Rivière, M.Y. Perrin, A. Soufiani, Plasma Sources Science and Technology **17**, 045010 (2008)
107. M. Damen, L. Martini, R. Engeln, Plasma Sources Science and Technology **29**, 095017 (2020)
108. A.S. Morillo-Candas, B.L.M. Klarenaar, C. Amoedo, V. Guerra, O. Guaitella, Journal of Physics D: Applied Physics **54**, 095208 (2020)
109. C. Stewig, S. Schüttler, T. Urbanietz, M. Böke, A. von Keudell, Journal of Physics D: Applied Physics **53**, 125205 (2020)
110. K. Siemsen, J. Reid, C. Dang, IEEE Journal of Quantum Electronics **16**, 668 (1980)
111. M.V. Spiridonov, S. McKenna-Lawlor, S.Y. Savinov, Journal of Quantitative Spectroscopy and Radiative Transfer **52**, 621 (1994)
112. S. Andreev, A. Mazurenko, M. Kerimkulov, V. Ochkin, S.Y. Savinov, S. Tskhai, Technical Physics C/C of Zhurnal Tekhnicheskoi Fiziki **39**, 466 (1994)
113. S. Andreev, V. Zakharov, V. Ochkin, S.Y. Savinov, Spectrochimica Acta Part A: Molecular and Biomolecular Spectroscopy **60**, 3361 (2004)
114. B.L.M. Klarenaar, M. Grofulović, A.S. Morillo-Candas, D.C.M. van den Bekerom, M.A. Damen, M.C.M. van de Sanden, O. Guaitella, R. Engeln, Plasma Sources Science and Technology **27**, 045009 (2018)
115. M.I. Buchwald, G.J. Wolga, The Journal of Chemical Physics **62**, 2828 (1975)
116. A. Nave, B. Baudrillart, S. Hamann, F. Bénédic, G. Lombardi, A. Gicquel, J. Van Helden, J. Röpcke, Plasma Sources Science and Technology **25**, 065002 (2016)
117. T. Kishimoto, N. Wenzel, H. Grosse-Wilde, G. Lüpke, G. Marowsky, Spectrochimica Acta Part B: Atomic Spectroscopy **47**, 51 (1992)
118. T. Kozák, A. Bogaerts, Plasma Sources Science and Technology **23**, 045004 (2014)
119. K.A. Essenhigh, Y.G. Utkin, C. Bernard, I.V. Adamovich, J. William Rich, Chemical Physics **330**, 506 (2006)
120. J. Cramp, J. Lambert, Chemical Physics Letters **22**, 146 (1973)
121. D.S. Pollock, G.B.I. Scott, L.F. Phillips, Geophysical Research Letters **20**, 727 (1993)
122. K.J. Castle, L.A. Black, M.W. Simione, J.A. Dodd, Journal of Geophysical Research: Space Physics **117** (2012)
123. K.J. Castle, K.M. Kleissas, J.M. Rhinehart, E.S. Hwang, J.A. Dodd, Journal of Geophysical Research: Space Physics **111** (2006)
124. R.E. Center, The Journal of Chemical Physics **58**, 5230 (1973)
125. A. Feofilov, A. Kutepov, C.Y. She, A. Smith, W. Pesnell, R. Goldberg, Atmospheric Chemistry and Physics **12**, 9013 (2012)
126. J.M. Samaniego, F. Egolfopoulos, C. Bowman, Combustion Science and Technology **109**, 183 (1995)
127. A. Pravilov, L. Smirnova, Kinetics and Catalysis **22**, 641 (1981)
128. M.M. Kopp, O. Mathieu, E.L. Petersen, International Journal of Chemical Kinetics **47**, 50 (2015)
129. F. Peeters, H. Hendrickx, A. van de Steeg, T. Righart, A. Wolf, G. van Rooij, W. Bongers, M. van de Sanden, *Chemiluminescence as a diagnostic tool in CO$_2$ microwave plasma*, in *Proceedings of the ISPC 2019, 24th International Symposium on Plasma Chemistry* (2019)
130. D. Otorbaev, Chemical Physics **196**, 543 (1995)
131. A.S. Morillo-Candas, V. Guerra, O. Guaitella, The Journal of Physical Chemistry C **124**, 17459 (2020)
132. T. Mikoviny, J. Skalny, J. Orszagh, N. Mason, Journal of physics D: Applied physics **40**, 6646 (2007)
133. A. Vesel, M. Mozetic, A. Drenik, M. Balat-Pichelin, Chemical Physics **382**, 127 (2011)
134. M. Balat-Pichelin, J. Iacono, P. Boubert, Ceramics International **42**, 2761 (2016)
135. S. Sepka, Y.K. Chen, J. Marschall, R.A. Copeland, Journal of Thermophysics and Heat Transfer **14**, 45 (2000)
136. D.R. Harding, R.E. Weston, G.W. Flynn, The Journal of Chemical Physics **88**, 3590 (1988)
137. A.J. Sedlacek, D.R. Harding, R.E. Weston Jr, T.G. Kreutz, G.W. Flynn, The Journal of chemical physics **91**, 7550 (1989)
138. L. Zhu, T.G. Kreutz, S.A. Hewitt, G.W. Flynn, The Journal of Chemical Physics **93**, 3277 (1990)
139. H.F. Chen, H.C. Chiang, H. Matsui, S. Tsuchiya, Y.P. Lee, The Journal of Physical Chemistry A **113**, 3431 (2009)
140. J.J. Gilijamse, S. Hoekstra, S.A. Meek, M. Metsälä, S.Y.T. van de Meerakker, G. Meijer, G.C. Groenenboom, The Journal of Chemical Physics **127**, 221102 (2007)
141. R.T. Jongma, G. Berden, G. Meijer, The Journal of chemical physics **107**, 7034 (1997)
142. R.R. Conway, Journal of Geophysical Research: Space Physics **86**, 4767 (1981)
143. T. Sawada, D. Sellin, A. Green, Journal of Geophysical Research **77**, 4819 (1972)
144. L. Mu-Tao, V. McKoy, Journal of Physics B: Atomic and Molecular Physics **15**, 3971 (1982)
145. N. Mason, W. Newell, Journal of Physics B: Atomic, Molecular and Optical Physics **21**, 1293 (1988)
146. A. Middleton, M. Brunger, P. Teubner, Journal of Physics B: Atomic, Molecular and Optical Physics **26**, 1743 (1993)
147. M.P. Skrzypkowski, T. Gougousi, R. Johnsen, M.F. Golde, The Journal of Chemical Physics **108**, 8400 (1998)
148. A.F.S. da Silva, A.S. Morillo-Candas, A. Tejero-del Caz, L.L. Alves, O. Guaitella, V. Guerra, Plasma Sources Science and Technology **29**, 125020 (2020)
149. T. Slanger, G. Black, J. Fournier, Journal of Photochemistry **4**, 329 (1975)
150. A. Cenian, A. Chernukho, V. Borodin, G. Śliwiński, Contributions to Plasma Physics **34**, 25 (1994)
151. I.J. Wysong, Chemical Physics Letters **329**, 42 (2000)
152. K. Schofield, Journal of Physical and Chemical Reference Data **8**, 723 (1979)
153. A. Cenian, A. Chernukho, V. Borodin, Contributions to Plasma Physics **35**, 273 (1995)
154. P.R.P. Barreto, H.d.O. Euclides, A.F. Albernaz, V. Aquilanti, M. Capitelli, G. Grossi, A. Lombardi, S. Macheret, F. Palazzetti, The European Physical Journal D **71**, 259 (2017)

155. P.B. Davies, P.A. Martin, Molecular Physics **70**, 89 (1990)

156. M. Yaron, A. Von Engel, P. Vidaud, Chemical Physics Letters **37**, 159 (1976)

157. R.B. Boodaghians, P.M. Borrell, P. Borrell, Chemical Physics Letters **97**, 193 (1983)

158. S. Löhle, T. Laux, M. Auweter-Kurtz, G. Herdrich, *LIF Measurements of NO in N$_2$/O$_2$ and N$_2$/CO$_2$ Plasma Flows*, in *36th AIAA Thermophysics Conference* (2003), p. 3487

159. H. Burghaus, G. Herdrich, S. Fasoulas, Vacuum p. 109901 (2020)

160. N. Bykova, L. Kuznetsova, Plasma physics reports **30**, 962 (2004)

161. B.A. Cruden, D. Prabhu, R. Martinez, Journal of Spacecraft and Rockets **49**, 1069 (2012)

162. S. Depraz, M.Y. Perrin, A. Soufiani, Journal of Quantitative Spectroscopy and Radiative Transfer **113**, 1 (2012)

163. M. Matsui, K. Tanaka, S. Yamagishi, S. Matsumoto, Y. Yamagiwa, K. Komurasaki, Y. Arakawa, Frontier of Applied Plasma Technology **4**, 1 (2011)

164. G. Yamada, S. Otsuta, T. Matsuno, H. Kawazoe, Transactions of the Japan Society for Aeronautical and Space Sciences, Aerospace Technology Japan **11**, 87 (2013)

165. L. Doyennette, M. Margottin-Maclou, H. Gueguen, A. Carion, L. Henry, The Journal of Chemical Physics **60**, 697 (1974)

166. M. Kovacs, D. Ramachandra Rao, A. Javan, The Journal of Chemical Physics **48**, 3339 (1968)

167. J. Misewich, P.L. Houston, R.P. Merrill, The Journal of Chemical Physics **82**, 1577 (1985)

168. J. Misewich, C.N. Plum, G. Blyholder, P.L. Houston, R.P. Merrill, The Journal of Chemical Physics **78**, 4245 (1983)

169. M. Margottin-Maclou, L. Doyennette, L. Henry, Applied Optics **10**, 1768 (1971)

170. I. Adamovich, S. Macheret, J. Rich, C. Treanor, J. Thermophys. Heat Transfer **12**, 57 (1998)

171. W.L. Hase, R.J. Duchovic, H.X. et al., Quantum Chemistry Program. Exchange Bull. **16**, 43 (1996)

172. G. Billing, Computer Physics Reports **1**, 239 (1984)

173. A. Lombardi, F. Pirani, M. Bartolomei, C. Coletti, A. Laganà, Frontiers in Chemistry **7**, 309 (2019)

174. P. Schuster, Berichte der Bunsengesellschaft für physikalische Chemie **87**, 291 (1983)

175. F. Pirani, S. Brizi, L.F. Roncaratti, P. Casavecchia, D. Cappelletti, F. Vecchiocattivi, Phys. Chem. Chem. Phys. **10**, 5489 (2008)

176. E. Kustova, E. Nagnibeda, I. Armenise, The Open Plasma Physics Journal **7**, 76 (2014)

177. C. Gorse, M. Cacciatore, M. Capitelli, Chemical Physics **85**, 165 (1984)

178. C. Gorse, M. Capitelli, Chemical Physics **85**, 177 (1984)

179. V.D. Rusanov, A.A. Fridman, G.V. Sholin, Soviet Physics Uspekhi **24**, 447 (1981)

180. V.D. Rusanov, A.A. Fridman, Soviet Physics Doklady **21**, 739 (1976)

181. J.P. Martin, M.Y. Perrin, P.I. Porshnev, Chemical Physics Letters **332**, 283 (2000)

182. L.D. Pietanza, V. Aquilanti, P. Barreto, M. Capitelli, G. Colonna, A. Lombardi, S. Macheret, F. Palazzetti, in *Hypersonic Meteoroid Entry Physics* (IOP Publishing, 2019), 2053-2563, pp. 18–1 to 18–19, ISBN 978-0-7503-1668-2

183. S. Macheret, H. Luo, A. Alexeenko, in *Hypersonic Meteoroid Entry Physics* (IOP Publishing, 2019), 2053-2563, pp. 17–1 to 17–14, ISBN 978-0-7503-1668-2

184. L.L. Alves, A. Bogaerts, V. Guerra, M.M. Turner, Plasma Sources Science and Technology **27**, 023002 (2018)

185. D. Pagnon, J. Amorim, J. Nahorny, M. Touzeau, M. Vialle, J. Phys. D: Appl. Phys. **28**, 1856 (1995)

186. T. Tsutsumi, A. Greb, A.R. Gibson, M. Hori, D. O'Connell, T. Gans, J. Appl. Phys. **121**, 143301 (2017)

187. Phelps database, `www.lxcat.net`, retrieved on October 5, 2020

188. Y. Itikawa, J. Phys. Chem. Ref. Data **31**, 749 (2002)

189. Itikawa database, `www.lxcat.net`, retrieved on October 5, 2020

190. R. Celiberto, V. Laporta, A. Laricchiuta, J. Tennyson, J.M. Wadehra, Open Plasma Phys. J. **7 (suppl 1:M2)**, 33 (2014)

191. R. Celiberto, I. Armenise, M. Cacciatore, M. Capitelli, F. Esposito, P. Gamallo, R.K. Janev, A. Laganà, V. Laporta, A. Laricchiuta et al., Plasma Sources Sci. Technol. **25**, 033004 (2016)

192. V. Laporta, J. Tennyson, R. Celiberto, Plasma Sources Sci. Technol **25**, 06LT2 (2016)

193. V.V. Stanković, M.M. Ristić, M.M. Vojnović, M.M. Aoneas, G.B. Poparić, Plasma Chemistry and Plasma Processing **40**, 1621 (2020)

194. S. Biagi, *Magboltz - transport of electrons in gas mixtures*, `magboltz.web.cern.ch/magboltz/`, accessed on October 5, 2020

195. Biagi-v7.1 database, `www.lxcat.net`, retrieved on October 5, 2020

196. L. Vialetto, P. Viegas, S. Longo, P. Diomede, Plasma Sources Sci. Technol. **29**, 115006 (2020)

197. Morgan database, `www.lxcat.net`, retrieved on October 5, 2020

198. Siglo database, `www.lxcat.net`, retrieved on October 5, 2020

199. Triniti database, `www.lxcat.net`, retrieved on October 5, 2020

200. B.L.M. Klarenaar, R. Engeln, M.A. Damen, M.C.M. van de Sanden, A.S. Morillo-Candas, P. Auvray, O. Guaitella, *Measuring vibrational excitation of CO$_2$ in a pulsed glow discharge*, in *Proceedings of the ISPC23 (International Symposium on Plasma Chemistry)* (Montréal, Canada, 2017)

201. B.L.M. Klarenaar, R. Engeln, D.C.M. van den Bekerom, M.C.M. van de Sanden, A.S. Morillo-Candas, O. Guaitella, Plasma Sources Sci. Technol. **26**, 115008 (2017)

202. A. Bogaerts, W. Wang, A. Berthelot, V. Guerra, Plasma Sources Science and Technology **25**, 055016 (2016)

203. W.L. Nighan, Appl. Phys. Lett. **15**, 355 (1969)

204. W.J. Wiegand, M.C. Fowler, J.A. Benda, Appl. Phys. Lett. **16**, 237 (1970)

205. L. Pietanza, G. Colonna, G. D'Ammando, A. Laricchiuta, M. Capitelli, Chemical Physics **468**, 44 (2016)

206. L.S. Polak, D.I. Slovetsky, Int. J. Radiat. Phys. Chem. **8**, 257.282 (1976)

207. N.Y. Babaeva, G. Naidis, Plasma Sources Science and Technology **30**, 03LT03 (2021)

208. J.E. Land, J. Appl. Phys. **49**, 5716 (1978)

209. P. Ogloblina, A. Tejero-del-Caz, V. Guerra, L.L. Alves, Plasma Sources Sci. Technol **29**, 015002 (2020)

210. A. Tejero-del-Caz, V. Guerra, D. Gonçalves, M.L. da Silva, L. Marques, N. Pinhão, C.D. Pintassilgo, L.L. Alves, Plasma Sources Sci. Technol. **28**, 043001 (2019)

211. G.J.M. Hagelaar, L.C. Pitchford, Plasma Sources Sci. Technol. **14**, 722 (2005)

212. Y. Itikawa, J. Phys. Chem. Ref. Data **44** (2015)

213. R.D. Hake, A.V. Phelps, Phys. Rev. **158**, 70 (1967)

214. V. Laporta, C.M. Cassidy, J. Tennyson, R. Celiberto, Plasma Sources Sci. Technol. **21**, 045005 (2012)

215. A.V. Phelps, Rev. Mod. Phys. **40**, 399 (1968)

216. L. Vialetto *et al*, In preparation (2021)

217. A. Laricchiuta, L.D. Pietanza, M. Capitelli, G. Colonna, Plasma Physics and Controlled Fusion **61**, 014009 (2018)

218. L.L. Alves, P. Coche, M.A. Ridenti, V. Guerra, Eur. Phys. J. D **70**, 124 (2016)

219. V. Guerra, A. Tejero-del-Caz, C.D. Pintassilgo, L.L. Alves, Plasma Sources Sci. Technol. **28**, 073001 (2019)

220. A.V. Phelps, Tech. Rep. 28, JILA Information Center Report (1985), university of Colorado, Boulder, Colorado, USA

221. D. Levron, A.V. Phelps, J. Chem. Phys. **69**, 2260 (1978)

222. Biagi database, www.lxcat.net, retrieved on June 2014

223. K. Wakiya, Journal of Physics B: Atomic and Molecular Physics **11**, 3913 (1978)

224. R.I. Hall, S. Trajmar, Journal of Physics B: Atomic and Molecular Physics **8**, L293 (1975)

225. G. Gousset, C.M. Ferreira, M. Pinheiro, P.A. Sa, M. Touzeau, M. Vialle, J. Loureiro, Journal of Physics D: Applied Physics **24**, 290 (1991)

226. E. Krishnakumar, S. Srivastava, International Journal of Mass Spectrometry and Ion Processes **113**, 1 (1992)

227. P.D. Burrow, The Journal of Chemical Physics **59**, 4922 (1973)

228. L. Vejby-Christensen, D. Kella, D. Mathur, H.B. Pedersen, H.T. Schmidt, L.H. Andersen, Physical Review A **53**, 2371 (1996)

229. V. Laporta, R. Celiberto, J. Tennyson, Plasma Sources Science and Technology **22**, 025001 (2013)

230. V. Laporta, R. Celiberto, J. Tennyson, Physical Review A **91**, 012701 (2015)

231. A. Annušová, D. Marinov, J.P. Booth, N. Sirse, M.L. da Silva, B. Lopez, V. Guerra, Plasma Sources Science and Technology **27**, 045006 (2018)

232. A.S. Kovalev, D.V. Lopaev, Yu. A. Mankelevich, N.A. Popov, T.V. Rakhimova, A. Yu. Poroykov, D.L. Carroll, J. Phys. D: Appl. Phys. **38**, 2360 (2005)

233. A.A. Ionin, I.V. Kochetov, A.P. Napartovich, N.N. Yuryshev, Journal of Physics D: Applied Physics **40**, R25 (2007)

234. A. Laricchiuta, R. Celiberto, M. Capitelli, Chemical Physics Letters **329**, 526 (2000)

235. M. Capitelli, R. Celiberto, *Electron-Molecule cross sections for plasma applications: the role of internal energy of the target* (Word Scientific Publishing, 1998), chap. 7, pp. 283–323

236. A. Kosarim, B. Smirnov, M. Capitelli, A. Laricchiuta, F. Paniccia, Chemical Physics Letters **422**, 513 (2006)

237. R.R. Laher, F.R. Gilmore, Journal of Physical and Chemical Reference Data **19**, 277 (1990)

238. G. Billing, in *Nonequilibrium Vibrational Kinetics. Topics in Current Physics*, edited by M. Capitelli (Springer, Berlin, Heidelberg, 1986), Vol. 39, pp. 85–112

239. T.E. Schwartzentruber, M.S. Grover, P. Valentini, Journal of Thermophysics and Heat Transfer **32**, 892 (2018)

240. T. Silva, M. Grofulović, B.L.M. Klarenaar, A.S. Morillo-Candas, O. Guaitella, R. Engeln, C.D. Pintassilgo, V. Guerra, Plasma Sources Science and Technology **27**, 015019 (2018)

241. M. Grofulović, T. Silva, B.L.M. Klarenaar, A.S. Morillo-Candas, O. Guaitella, R. Engeln, C.D. Pintassilgo, V. Guerra, Plasma Sources Science and Technology **27**, 115009 (2018)

242. A.S. Morillo-Candas, T. Silva, B.L.M. Klarenaar, M. Grofulović, V. Guerra, O. Guaitella, Plasma Sources Science and Technology **29**, 01LT01 (2020)

243. L. Polak, D. Slovetsky, International Journal for Radiation Physics and Chemistry **8**, 257 (1976)

244. V. Laporta, J. Tennyson, R. Celiberto, Plasma Sources Science and Technology **25**, 01LT04 (2016)

245. K. Kutasi, V. Guerra, P. Sá, Journal of Physics D: Applied Physics **43**, 175201 (2010)

246. C. Lee, D.B. Graves, M.A. Lieberman, D.W. Hess, Journal of The Electrochemical Society **141**, 1546 (1994)

247. J.T. Gudmundsson, I.G. Kouznetsov, K.K. Patel, M.A. Lieberman, Journal of Physics D: Applied Physics **34**, 1100 (2001)

248. H. Hokazono, H. Fujimoto, Journal of Applied Physics **62**, 1585 (1987)

249. B.F. Gordiets, A.I. Osipov, E.V. Stupochenko, L.A. Shelepin, Soviet Physics Uspekhi **15**, 759 (1973)

250. E. Kustova, E. Nagnibeda, Chem. Phys. **321**, 293 (2006)

251. M. Capitelli, E. Molinari, in *Plasma Chemistry II. Topics in Current Chemistry* (Springer, Berlin, Heidelberg, 1980), Vol. 90, pp. 59–109

252. A. Bogaerts, C. De Bie, R. Snoeckx, T. Kozák, Plasma Processes and Polymers **14**, 1600070 (2017)

253. A. Bogaerts, A. Berthelot, S. Heijkers, S. Kolev, R. Snoeckx, S. Sun, G. Trenchev, K.V. Laer, W. Wang, Plasma Sources Science and Technology **26**, 063001 (2017)

254. R. Aerts, T. Martens, A. Bogaerts, The Journal of Physical Chemistry C **116**, 23257 (2012)

255. R. Aerts, W. Somers, A. Bogaerts, ChemSusChem **8**, 702 (2015)

256. T. Kozák, A. Bogaerts, Plasma Sources Science and Technology **24**, 015024 (2015)

257. A. Berthelot, A. Bogaerts, Plasma Sources Science and Technology **25**, 045022 (2016)

258. W. Wang, A. Berthelot, S. Kolev, X. Tu, A. Bogaerts, Plasma Sources Science and Technology **25**, 065012 (2016)

259. K. Peerenboom, A. Parente, T. Kozák, A. Bogaerts, G. Degrez, Plasma Sources Science and Technology **24**, 025004 (2015)

260. J.F. de la Fuente, S.H. Moreno, A.I. Stankiewicz, G.D. Stefanidis, React. Chem. Eng. **1**, 540 (2016)

261. P. Diomede, M.C.M. van de Sanden, S. Longo, The Journal of Physical Chemistry C **121**, 19568 (2017)

262. P. Viegas, M.C.M. van de Sanden, S. Longo, P. Diomede, The Journal of Physical Chemistry C **123**, 22823 (2019)

263. P. Diomede, M.C.M. van de Sanden, S. Longo, The Journal of Physical Chemistry A **122**, 7918 (2018)

264. S.R. Sun, H.X. Wang, A. Bogaerts, Plasma Sources Science and Technology **29**, 025012 (2020)

265. L.D. Pietanza, G. Colonna, G. D'Ammando, A. Laricchiuta, M. Capitelli, Plasma Sources Science and Technology **24**, 042002 (2015)
266. L.D. Pietanza, G. Colonna, G. D'Ammando, A. Laricchiuta, M. Capitelli, Physics of Plasmas **23**, 013515 (2016)
267. L.D. Pietanza, G. Colonna, V. Laporta, R. Celiberto, G. D'Ammando, A. Laricchiuta, M. Capitelli, The Journal of Physical Chemistry A **120**, 2614 (2016)
268. L.D. Pietanza, G. Colonna, G. D'Ammando, M. Capitelli, Plasma Physics and Controlled Fusion **59**, 014035 (2016)
269. M. Capitelli, G. Colonna, G. D'Ammando, L.D. Pietanza, Plasma Sources Science and Technology **26**, 055009 (2017)
270. L.D. Pietanza, G. Colonna, M. Capitelli, Plasma Sources Science and Technology **26**, 125007 (2017)
271. L.D. Pietanza, G. Colonna, M. Capitelli, Plasma Sources Science and Technology **27**, 095004 (2018)
272. L.D. Pietanza, G. Colonna, A. Laricchiuta, M. Capitelli, Plasma Sources Science and Technology **27**, 095003 (2018)
273. L.D. Pietanza, G. Colonna, M. Capitelli, Physics of Plasmas **27**, 023513 (2020)
274. L.D. Pietanza, G. Colonna, M. Capitelli, Plasma Sources Science and Technology **29**, 035022 (2020)
275. L.D. Pietanza, G. Colonna, M. Capitelli, Physics of Plasmas **27**, 093510 (2020)
276. I. Armenise, E. Kustova, Chem. Phys. **428**, 90 (2014)
277. I. Armenise, E. Kustova, J. Phys. Chem. A **122**, 5107 (2018)
278. I. Armenise, E. Kustova, J. Phys. Chem. A **122**, 8709 (2018)
279. E. Kustova, A. Savelev, I. Armenise, J. Phys. Chem. A **123**, 10529 (2019)
280. I. Armenise, Chemical Physics **491**, 11 (2017)
281. J. Annaloro, A. Bultel, Physics of Plasmas **26**, 103505 (2019)
282. J.L. Cheng, H.X. Wang, S.R. Sun, Chinese Physics Letters **33**, 108201 (2016)
283. S. Ponduri, M.M. Becker, S. Welzel, M.C.M. van de Sanden, D. Loffhagen, R. Engeln, Journal of Applied Physics **119**, 093301 (2016)
284. M.S. Moss, K. Yanallah, R.W.K. Allen, F. Pontiga, Plasma Sources Science and Technology **26**, 035009 (2017)
285. P. Koelman, S. Heijkers, S. Tadayon Mousavi, W. Graef, D. Mihailova, T. Kozak, A. Bogaerts, J. van Dijk, Plasma Processes and Polymers **14**, 1600155 (2017)
286. A. Berthelot, A. Bogaerts, Plasma Sources Science and Technology **26**, 115002 (2017)
287. R. Snoeckx, R. Aerts, X. Tu, A. Bogaerts, The Journal of Physical Chemistry C **117**, 4957 (2013)
288. R. Snoeckx, Y.X. Zeng, X. Tu, A. Bogaerts, RSC Adv. **5**, 29799 (2015)
289. C. De Bie, J. van Dijk, A. Bogaerts, The Journal of Physical Chemistry C **119**, 22331 (2015)
290. R. Snoeckx, S. Heijkers, K. Van Wesenbeeck, S. Lenaerts, A. Bogaerts, Energy Environ. Sci. **9**, 999 (2016)
291. C. De Bie, J. van Dijk, A. Bogaerts, The Journal of Physical Chemistry C **120**, 25210 (2016)
292. R. Snoeckx, A. Ozkan, F. Reniers, A. Bogaerts, ChemSusChem **10**, 409 (2017)
293. C. Verheyen, T. Silva, V. Guerra, A. Bogaerts, Plasma Sources Sci. Technol. **29**, 095009 (2020)
294. W. Wang, R. Snoeckx, X. Zhang, M.S. Cha, A. Bogaerts, The Journal of Physical Chemistry C **122**, 8704 (2018)
295. J. Slaets, M. Aghaei, S. Ceulemans, S. Van Alphen, A. Bogaerts, Green Chem. **22**, 1366 (2020)
296. A. Bogaerts, T. Kozák, K. van Laer, R. Snoeckx, Faraday Discuss. **183**, 217 (2015)
297. A. Berthelot, A. Bogaerts, The Journal of Physical Chemistry C **121**, 8236 (2017)
298. A. Berthelot, A. Bogaerts, Journal of CO$_2$ Utilization **24**, 479 (2018)
299. V. Vermeiren, A. Bogaerts, The Journal of Physical Chemistry C **122**, 25869 (2018)
300. V. Vermeiren, A. Bogaerts, The Journal of Physical Chemistry C **123**, 17650 (2019)
301. S. Sun, H. Wang, D. Mei, X. Tu, A. Bogaerts, Journal of CO2 Utilization **17**, 220 (2017)
302. V. Kotov, P.M.J. Koelman, Plasma Sources Science and Technology **28**, 095002 (2019)
303. A.J. Wolf, F.J. Peeters, P.W.C. Groen, W.A. Bongers, M.C. van de Sanden, The Journal of Physical Chemistry C **124**, 16806 (2020)
304. P. Viegas, L. Vialetto, A.J. Wolf, F. Peeters, P.W.C. Groen, T.W. Righart, W. Bongers, R.V. de Sanden, P. Diomede, Plasma Sources Science and Technology (2020)
305. V. Vermeiren, A. Bogaerts, The Journal of Physical Chemistry C **124**, 18401 (2020)
306. S. Heijkers, A. Bogaerts, The Journal of Physical Chemistry C **121**, 22644 (2017)
307. S. Heijkers, L.M. Martini, G. Dilecce, P. Tosi, A. Bogaerts, The Journal of Physical Chemistry C **123**, 12104 (2019)
308. M. Pannier, Ph.D. thesis, Universitè Paris-Saclay (2019)
309. G.J. van Rooij, D.C.M. van den Bekerom, N. den Harder, T. Minea, G. Berden, W.A. Bongers, R. Engeln, M.F. Graswinckel, E. Zoethout, M.C.M. van de Sanden, Faraday Discuss. **183**, 233 (2015)
310. D.C.M. van den Bekerom, J.M.P. Linares, T. Verreycken, E.M. van Veldhuizen, S. Nijdam, G. Berden, W.A. Bongers, M.C.M. van de Sanden, G.J. van Rooij, Plasma Sources Science and Technology **28**, 055015 (2019)
311. A.Wolf, Ph.D. thesis, Eindhoven University of Technology (2020)
312. T. Silva, N. Britun, T. Godfroid, R. Snyders, Plasma Processes and Polymers **14**, 1600103 (2017)
313. V.A. Legasov, V.K. Zhivotov, E.G. Krasheninnikov, M.F. Kroto, B.I. Patrushev, V.D. Rusanov, G.V. Rykunov, A.M. Spektor, A.A. Fridman, G.V. Shoiin, Soviet Physics Doklady **23**, 44 (1978)
314. R.I. Azizoz, A.K. Vakar, V.K. Zhivotov, V.K. Krotov, O.A. Zinov'ev, B.V. Potapkin, A.A. Rusanov, V.D. Rusanov, A.A. Fridman, Dokl. Akad. Nauk SSSR **271**, 94 (1983)
315. K. Hassouni, A. Gicquel, M. Capitelli, J. Loureiro, Plasma Sources Science Technology **8**, 494 (1999)
316. M. Capitelli, M. Cacciatore, R. Celiberto, O. De Pascale, P. Diomede, F. Esposito, A. Gicquel, C. Gorse, K. Hassouni, A. Laricchiuta et al., Nuclear Fusion **46**, S260 (2006)
317. J. Bretagne, G. Delouya, C. Gorse, M. Capitelli, M. Bacal, Journal of Physics D: Applied Physics **18**, 811 (1985)
318. G. Colonna, L. Pietanza, M. Capitelli, Spectrochimica Acta Part B: Atomic Spectroscopy **56**, 587 (2001)

319. G. Colonna, L.D. Pietanza, M. Capitelli, Journal of Thermophysics and Heat Transfer **22**, 399 (2008)

320. M. Capitelli, R. Celiberto, G. Colonna, E. Esposito, A. Laricchiuta, S. Longo, K. Hassouni, *Fundamental Aspects of Plasma Chemical Physics: Kinetics*, Vol. 85 (Springer Series on Atomic, Optical, and Plasma Physics, 2016)

321. M. Capitelli, I. Armenise, D. Bruno, M. Cacciatore, R. Celiberto, G. Colonna, O.D. Pascale, P. Diomede, F. Esposito, C. Gorse et al., Plasma Sources Science and Technology **16**, S30 (2007)

322. M. Šimek, Z. Bonaventura, Journal of Physics D: Applied Physics **51**, 504004 (2018)

323. W.L. Nighan, Phys. Rev. A **2**, 1989 (1970)

324. M. Capitelli, M. Dilonardo, E. Molinari, Chemical Physics **20**, 417 (1977)

325. M. Capitelli, C. Gorse, G. Billing, Chemical Physics **52**, 299 (1980)

326. V.D. Rusanov, A.A. Fridman, G.V. Sholin, Akademiia Nauk SSSR Doklady **237**, 1338 (1977)

327. P.W.C. Groen, A.J. Wolf, T.W.H. Righart, M.C.M. van de Sanden, F.J.J. Peeters, W.A. Bongers, Plasma Sources Science and Technology **28**, 075016 (2019)

328. J.A. Blauer, G.R. Nickerson, Tech. Rep. AFRPL-TR-73-57, Air Force Rocket Propulsion Laboratory (1973)

329. R.N. Schwartz, K.F. Herzfeld, J. Chem. Phys. **22**, 767 (1954)

330. R.D. Sharma, C. Brau, J. Chem. Phys. **50**, 924 (1969)

331. T.G. Kreutz, J.A. O'Neill, G.W. Flynn, J. Phys. Chem. **91**, 5540 (1987)

332. J.O. Hirschfelder, C.F. Curtiss, R.B. Bird, *Molecular Theory of Gases and Liquids* (Wiley, New York, 1964)

333. G. Black, H. Wise, S. Schechter, R.L. Sharpless, J. Chem. Phys. **60**, 3526 (1974)

334. F.S. Milos, Y.K. Chen, W.M. Congdon, J.M. Thornton, Journal of Spacecraft and Rockets **36**, 380 (1999)

335. K.T. Edquist, B.R. Hollis, C.O. Johnston, D. Bose, T.R. White, M. Mahzari, Journal of Spacecraft and Rockets **51**, 1106 (2014)

336. P. Reynier, Progress in Aerospace Sciences **70**, 1 (2014)

337. B.R. Hollis, J.N. Perkins, AIAA Paper **95-2314** (1995), 26th AIAA Fluid Dynamics Conference, San Diego, June 19-22, 1995

338. B.R. Hollis, J.N. Perkins, Journal of Spacecraft and Rockets **34**, 449 (1997)

339. I. Egorov, V. Borovoy, A. Skuratov, 48th AIAA Aerospace Sciences Meeting Including the New Horizons Forum and Aerospace Exposition **2010-1073** (2010)

340. O. Kunova, A. Kosareva, E. Kustova, E. Nagnibeda, Phys. Rev. Fluids **5**, 123401 (2020)

341. A. Kosareva, O. Kunova, E. Kustova, E. Nagnibeda, Physics of Fluids **33**, 016103 (2021)

342. C. Park, J. Howe, R. Howe, R. Jaffe, G. Candler, J. Thermophys. Heat Transfer **8**, 9 (1994)

343. S. Surzhikov, 43rd AIAA Thermophysics Conference **2012-2867** (2012)

344. E. Kustova, E. Nagnibeda, Y. Shevelev, N. Syzranova, Shock Waves **21**, 273 (2011)

345. Y. Shevelev, N. Syzranova, E. Nagnibeda, E. Kustova, Doklady Physics **60**, 207 (2015)

346. A. Kosareva, G. Shoev, Acta Astronautica **160**, 461 (2019)

347. A. Sahai, B. Lopez, C. Johnston, M. Panesi, AIAA SciTech Forum - 55th AIAA Aerospace Sciences Meeting **AIAA 2017-0213** (2017)

348. A. Sahai, B. Lopez, C. Johnston, M. Panesi, J. Chem. Phys. **147**, 054107 (2017)

349. A. Sahai, C.O. Johnston, B. Lopez, M. Panesi, Phys. Rev. Fluids **4**, 093401 (2019)

350. M. Khaji, K. Peerenboom, J. van der Mullen, G. Degrez, Journal of Physics D: Applied Physics **53**, 395201 (2020)

351. G. Colonna, M. Capitelli, Journal of thermophysics and heat transfer **10**, 406 (1996)

352. I. Armenise, M. Capitelli, G. Colonna, G. Gorse, Journal of thermophysics and heat transfer **10**, 397 (1996)

353. R. Taylor, S. Bitterman, Rev. Mod. Phys. **41**, 26 (1969)

354. J. Blauer, G. Nickerson, AIAA Paper **74-536** (1974)

355. O. Achasov, D. Ragosin, Preprint no. 16, institute of heat and mass transfer, minsk, bielarus, Institute of Heat and Mass Transfer, Minsk, Bielarus (1986)

356. S. Losev, P. Kozlov, L. Kuznezova, V. Makarov, Y. Romanenko, S. Surzhikov, G. Zalogin, *Radiation of CO$_2$-N$_2$-Ar mixture in a shock wave: experiment and modeling*, in *Proc. of 3rd European Symposium on Aerothermodynamics for Space Vehicles* (ESTEC, Noordwiik, 1998), Vol. 426, pp. 437–444

357. C. Wickham-Jones, C. Simpson, D. Clary, Chem. Phys. **117**, 9 (1987)

358. R. Mc Kenzie, J. Arnold, AIAA Paper **67-322** (1967)

359. E. Kustova, E. Nagnibeda, T. Alexandrova, A. Chikhaoui, Chem. Phys. **276**, 139 (2002)

360. O. Kunova, E. Kustova, M. Mekhonoshina, E. Nagnibeda, Chem. Phys. **463**, 70 (2015)

361. E. Kustova, E. Nagnibeda, Chem. Phys. **233**, 57 (1998)

362. E. Kustova, Chem. Phys. **270**, 177 (2001)

363. E. Kustova, E. Nagnibeda, Chem. Phys. **398**, 111 (2012)

364. E. Kustova, M. Mekhonoshina, A. Kosareva, Physics of Fluids **31**, 046104 (2019)

365. I. Armenise, M. Capitelli, E. Kustova, E. Nagnibeda, J. Thermophys. Heat Transfer **13**, 210 (1999)

366. E. Kustova, E. Nagnibeda, I. Armenise, M. Capitelli, J. Thermophys. Heat Transfer **16**, 238 (2002)

367. E. Despiau-Pujo, A. Davydova, G. Cunge, L. Delfour, L. Magaud, D.B. Graves, J. Appl. Phys. **113**, 114302 (2013)

368. W.A. Seward, E.J. Jumper, J. Thermophys. Heat Trans. **5**, 284 (1991)

369. A. Daiβ, H.H. Frühauf, , E.W. Messerschmid, J. Thermophys. Heat Trans. **11**, 346 (1997)

370. V. Kovalev, A. Kolesnikov, Fluid Dynamics **40**, 669 (2005)

371. V. Kovalev, N. Afonina, V. Gromov, in *Shock Waves*, edited by Z. Jiang (Springer Berlin Heidelberg, 2005), pp. 597–602, ISBN 978-3-540-22497-6

372. P.L. Houston, R.P. Merrill, Chemical Reviews **88**, 657 (1988)

373. L. Bedra, M. Rutigliano, M. Ballat-Pichelin, M. Cacciatore, Langmuir **22**, 7208 (2006)

374. M. Rutigliano, C. Zazza, N. Sanna, A. Pieretti, G. Mancini, V. Barone, M. Cacciatore, J. Phys. Chem. A **113**, 15366 (2009)

375. D.R. Glowacki, W.J. Rodgers, R. Shannon, S.H. Robertson, J.N. Harvey, Phil. Trans. R. Soc. A **375**, 20160206 (2017)

376. J. Vieceli, I. Chorny, I. Benjamin, J. Chem. Phys. **117**, 4532 (2002)

377. I. Chorny, I. Benjamin, J. Mol. Liq. **110**, 133 (2004)

378. T. Ishiyama, J. Chem. Phys. **154**, 104708 (2021)

379. D. Mantell, S. Ryali, G. Haller, J. Fenn, The Journal of Chemical Physics **78**, 4250 (1983)

380. P. Lorraine, B. Thoms, R. Machonkin, W. Ho, The Journal of chemical physics **96**, 3285 (1992)

381. B. Jiang, H. Guo, *Communication: Enhanced dissociative chemisorption of co$_2$ via vibrational excitation* (2016)

382. J.J. Nogueira, S.A. Vázquez, O.A. Mazyar, W.L. Hase, B.G. Perkins Jr, D.J. Nesbitt, E. Martínez-Núñez, The Journal of Physical Chemistry A **113**, 3850 (2009)

383. Y. Yao, P. Shushkov, T.F. Miller, K.P. Giapis, Nature communications **10**, 1 (2019)

384. M. Rutigliano, M. Cacciatore, Journal of Thermophysics and Heat Transfer **30**, 247 (2016)

385. V. Berkut, V. Doroshenko, V. Kovtun, N. Koudryavtsev, S. Novikov, N. Smirnov, A. Sharotovov, Soviet Journal of Chemical Physics **9**, 2222 (1992)

386. I. Kim, G. Park, J.J. Na, International Journal of Heat and Mass Transfer **138**, 916 (2019)

387. A. Kolesnikov, M. Yakushin, S. Vasil'Evskii, I. Pershin, A. Gordeev, *Catalysis effects on quartz surface in high-enthalpy subsonic oxygen & carbon dioxide flows*, in *Aerothermodynamics for space vehicles* (1999), Vol. 426, p. 537

388. P. Macko, P. Veis, G. Cernogora, Plasma Sources Sci. Technol. **13**, 251 (2004)

389. V. Guerra, IEEE Transactions on Plasma Science **35**, 1397 (2007)

390. J.P. Booth, O. Guaitella, A. Chatterjee, C. Drag, V. Guerra, D. Lopaev, S. Zyryanov, T. Rakhimova, D. Voloshin, Y. Mankelevich, Plasma Sources Science and Technology **28**, 055005 (2019)

391. G. Cartry, X. Duten, A. Rousseau, Plasma Sources Science and Technology **15**, 479 (2006)

392. C. Arasa, P. Gamallo, R. Sayós, J. Phys. Chem. B **109**, 14954 (2005)

393. A.A. Buchachenko, A.A. Kroupnov, V.L. Kovalev, Acta Astronaut. **100**, 40 (2014)

394. P. Gamallo, H. Prats, R. Sayós, Journal of molecular modeling **20**, 1 (2014)

395. R. Meana-Pañeda, Y. Paukku, K. Duanmu, P. Norman, T.E. Schwartzentruber, D.G. Truhlar, J. Phys. Chem. C **119**, 9287 (2015)

396. P. Norman, T.E. Schwartzentruber, H. Leverentz, S. Luo, R.M.P. neda, Y. Paukku, D.G. Truhlar, J. Phys. Chem. C **117**, 9311 (2013)

397. K.M. Bal, E. Neyts, Chem. Sci. **7**, 5280 (2016)

398. K.M. Bal, S. Huygh, A. Bogaerts, E.C. Neyts, Plasma Sources Science and Technology **27**, 024001 (2018)

399. K.A. Fichthorn, W.H. Weinberg, J. Chem. Phys. **95**, 1090 (1991)

400. J.S. Reese, S. Raimondeau, D.G. Vlachos, J. Comput. Phys. **173**, 302 (2001)

401. V. Guerra, J. Loureiro, Plasma Sources Sci. Technol. **13**, 85 (2004)

402. V.L. Kovalev, V. Yu. Sazonenko, A.N. Yakunchikov, Mosc. Univ. Mech. Bull. **62**, 53 (2007)

403. H.M. Cuppen, L.J. Karssemeijer, T. Lamberts, Chem. Rev. **113**, 8840 (2013)

404. V. Guerra, D. Marinov, Plasma Sources Sci. Technol. **25**, 045001 (2016)

405. D. Marinov, C. Teixeira, V. Guerra, Plasma Processes and Polymers **14**, 1600175 (2017)

406. D. Marinov, Front. Chem. Sci. eng. **13**, 815 (2019)

407. Y.C. Kim, M. Boudart, Langmuir **7**, 2999 (1991)

408. B.F. Gordiets, C.M. Ferreira, J. Nahorny, D. Pagnon, M. Touzeau, M. Vialle, J. Phys. D: Appl. Phys. **29**, 1021 (1996)

409. G. Cartry, L. Magne, G. Cernogora, J. Phys. D: Appl. Phys. **33**, 1303 (2000)

410. D.V. Lopaev, E.M. Malykhin, S.M. Zyryanov, J. Phys. D: Appl. Phys. **44**, 015201 (2011)

411. V.M. Donnelly, J. Guha, L. Stafford, J. Vac. Sci. Technol. A **29**, 010801 (2011)

412. J. Hong, S. Pancheshnyi, E. Tam, J.J. Lowke, S. Prawer, A.B. Murphy, Journal of Physics D: Applied Physics **50**, 154005 (2017)

413. P. Mehta, P. Barboun, F.A. Herrera, J. Kim, P. Rumbach, D.B. Go, J.C. Hicks, W.F. Schneider, Nature Catalysis **1**, 269 (2018)

414. J. Shah, W. Wang, A. Bogaerts, M.L. Carreon, ACS Applied Energy Materials **1**, 4824 (2018)

415. P. Mehta, P. Barboun, Y. Engelmann, D.B. Go, A. Bogaerts, W.F. Schneider, J.C. Hicks, ACS Catalysis (2020)

416. Y. Engelmann, P. Mehta, E.C. Neyts, W.F. Schneider, A. Bogaerts, ACS Sustainable Chemistry & Engineering **8**, 6043 (2020)

417. R. Michiels, Y. Engelmann, A. Bogaerts, The Journal of Physical Chemistry C **124**, 25859 (2020)

418. B. Loenders, Y. Engelmann, A. Bogaerts, The Journal of Physical Chemistry C **125**, 2966 (2021)

419. T. Nozaki, K. Okazaki, Catalysis Today **211**, 29 (2013), recent Advances in Plasma and Catalysis (ISPCEM 2012)

420. V. Aquilanti, K.C. Mundim, M. Elango, S. Kleijn, T. Kasai, Chemical Physics Letters **498**, 209 (2010)

421. J. Kumamoto, J.K. Raison, J.M. Lyons, Journal of Theoretical Biology **31**, 47 (1971)

422. V.H. Silva, V. Aquilanti, H.C. de Oliveira, K.C. Mundim, Chemical Physics Letters **590**, 201 (2013)

423. V. Aquilanti, N.D. Coutinho, V.H. Carvalho-Silva, Philosophical Transactions of the Royal Society A: Mathematical, Physical and Engineering Sciences **375**, 20160201 (2017)

424. V.H. Carvalho-Silva, N.D. Coutinho, V. Aquilanti, Molecules **25**, 2098 (2020)

425. A. Jafarzadeh, K. Bal, A. Bogaerts, E. Neyts, The Journal of Physical Chemistry C **123**, 6516 (2019)

426. A. Jafarzadeh, K.M. Bal, A. Bogaerts, E.C. Neyts, The Journal of Physical Chemistry C **124**, 6747 (2020)

427. K. Van Laer, A. Bogaerts, Plasma Sources Science and Technology **25**, 015002 (2015)

428. J. Kruszelnicki, K.W. Engeling, J.E. Foster, Z. Xiong, M.J. Kushner, Journal of Physics D: Applied Physics **50**, 025203 (2016)

429. W. Wang, H.H. Kim, K. Van Laer, A. Bogaerts, Chemical Engineering Journal **334**, 2467 (2018)

430. Q.Z. Zhang, A. Bogaerts, Plasma Sources Science and Technology **27**, 105013 (2018)

431. F. Holzer, U. Roland, F.D. Kopinke, Applied Catalysis B: Environmental **38**, 163 (2002)

432. U. Roland, F. Holzer, F.D. Kopinke, Applied catalysis B: environmental **58**, 217 (2005)

433. K. Hensel, S. Katsura, A. Mizuno, IEEE Transactions on Plasma Science **33**, 574 (2005)
434. K. Hensel, V. Martišovitš, Z. Machala, M. Janda, M. Leštinskỳ, P. Tardiveau, A. Mizuno, Plasma Processes and Polymers **4**, 682 (2007)
435. K. Hensel, The European Physical Journal D **54**, 141 (2009)
436. A. Bogaerts, Q.Z. Zhang, Y.R. Zhang, K. Van Laer, W. Wang, Catalysis Today **337**, 3 (2019)
437. Y.R. Zhang, K. Van Laer, E.C. Neyts, A. Bogaerts, Applied Catalysis B: Environmental **185**, 56 (2016)
438. Y.R. Zhang, E.C. Neyts, A. Bogaerts, The Journal of Physical Chemistry C **120**, 25923 (2016)
439. Y.R. Zhang, E.C. Neyts, A. Bogaerts, Plasma Sources Science and Technology **27**, 055008 (2018)
440. Y. Zhang, H.y. Wang, Y.r. Zhang, A. Bogaerts, Plasma Sources Science and Technology **26**, 054002 (2017)
441. Q.Z. Zhang, A. Bogaerts, Plasma Sources Science and Technology **27**, 035009 (2018)
442. Q.Z. Zhang, W.Z. Wang, A. Bogaerts, Plasma Sources Science and Technology **27**, 065009 (2018)
443. M. Ramakers, G. Trenchev, S. Heijkers, W. Wang, A. Bogaerts, ChemSusChem **10**, 2642 (2017)
444. K. Van Laer, A. Bogaerts, Plasma Processes and Polymers **14**, 1600129 (2017)
445. K. Van Laer, A. Bogaerts, Plasma Sources Science and Technology **26**, 085007 (2017)
446. W.S. Kang, J.M. Park, Y. Kim, S.H. Hong, IEEE Transactions on Plasma Science **31**, 504 (2003)
447. H. Russ, M. Neiger, J.E. Lang, IEEE transactions on plasma science **27**, 38 (1999)
448. N.Y. Babaeva, A.N. Bhoj, M.J. Kushner, Plasma Sources Science and Technology **15**, 591 (2006)
449. W.S. Kang, H.H. Kim, Y. Teramoto, A. Ogata, J.Y. Lee, D.W. Kim, M. Hur, Y.H. Song, Plasma Sources Science and Technology **27**, 015018 (2018)
450. M. Jimenez-Diaz, E. Carbone, J. van Dijk, J. Van der Mullen, Journal of Physics D: Applied Physics **45**, 335204 (2012)
451. S. Rahimi, M. Jimenez-Diaz, S. Hübner, E. Kemaneci, J. Van der Mullen, J. Van Dijk, Journal of Physics D: Applied Physics **47**, 125204 (2014)
452. Y. Kabouzi, D. Graves, E. Castaños-Martínez, M. Moisan, Physical Review E **75**, 016402 (2007)
453. V. Georgieva, A. Berthelot, T. Silva, S. Kolev, W. Graef, N. Britun, G. Chen, J. van der Mullen, T. Godfroid, D. Mihailova et al., Plasma processes and polymers **14**, 1600185 (2017)
454. J.F. de la Fuente, S.H. Moreno, A.I. Stankiewicz, G.D. Stefanidis, International Journal of Hydrogen Energy **42**, 12943 (2017)
455. S. Kolev, A. Bogaerts, Plasma Sources Science and Technology **24**, 015025 (2014)
456. S. Kolev, A. Bogaerts, Plasma Sources Science and Technology **24**, 065023 (2015)
457. G. Trenchev, S. Kolev, A. Bogaerts, Plasma Sources Science and Technology **25**, 035014 (2016)
458. S. Sun, S. Kolev, H. Wang, A. Bogaerts, Plasma Sources Science and Technology **26**, 015003 (2016)
459. S. Sun, S. Kolev, H. Wang, A. Bogaerts, Plasma Sources Science and Technology **26**, 055017 (2017)
460. S. Kolev, S. Sun, G. Trenchev, W. Wang, H. Wang, A. Bogaerts, Plasma Processes and Polymers **14**, 1600110 (2017)
461. S. Kolev, A. Bogaerts, Plasma Sources Science and Technology **27**, 125011 (2018)
462. A.F. Gutsol, S.P. Gangoli, IEEE Transactions on Plasma Science **45**, 555 (2017)
463. H. Zhang, H. Zhang, G. Trenchev, X. Li, Y. Wu, A. Bogaerts, Plasma Sources Science and Technology **29**, 045019 (2020)
464. G. Trenchev, S. Kolev, W. Wang, M. Ramakers, A. Bogaerts, The Journal of Physical Chemistry C **121**, 24470 (2017)
465. G. Trenchev, A. Bogaerts, Journal of CO$_2$ Utilization **39**, 101152 (2020)
466. G. Trenchev, A. Nikiforov, W. Wang, A. Bogaerts et al., Chemical Engineering Journal **362**, 830 (2019)
467. Q. Ong, D.C.M. van den Bekerom, G. Berden, M.C.M. van de Sanden, G.J. van Rooij, *Vibrational excitement: from CO$_2$ to CO*, in *ISPC 2019, 24st International Symposium on Plasma Chemistry* (Naples, Italy, 2019), p. P1.32, http://ispc24.com/
468. C. Verheyen, T. Silva, V. Guerra, A. Bogaerts, Plasma Sources Science and Technology **29**, 095009 (2020)